

MicroBooNE

A.N. Author¹

¹*Institution 1, City, State 12345*

ABSTRACT: This paper describes the design and construction of the MicroBooNE liquid argon time projection chamber and associated systems. Details of design specifications, assembly procedures, and acceptance tests are reported.

KEYWORDS: Time projection chambers; Noble liquid detectors; Neutrino detectors.

Contents

1. Introduction and Physics Motivation	3
2. Experiment Overview	5
2.1 The MicroBooNE LArTPC	6
2.2 MicroBooNE LArTPC Implementation	8
3. Cryogenic System	9
3.1 Cryostat Design Overview	11
3.2 Liquid Argon Purification Subsystem	12
3.3 Nitrogen Refrigeration	17
3.4 Controls and Purity Monitoring	17
4. Liquid Argon Time Projection Chamber	18
4.1 Cathode	19
4.2 Field Cage	20
4.2.1 Resistor Divider Chain	24
4.3 Anode	26
4.3.1 Mechanical structure	28
4.3.2 Wire winding and quality assurance	28
4.3.3 Wire installation and tension measurements	29
4.4 Parts Preparation	30
4.4.1 Cleaning stainless steel	31
4.4.2 Cleaning G-10	32
4.5 Assembly	32
4.6 High Voltage System	32
5. Light Collection System	36
5.1 Light Production in Argon	37
5.2 The Primary Light Collection System	39
5.2.1 Photomultiplier Tubes and Bases	40
5.2.2 Wavelength-Shifting Plates	43
5.2.3 UV Light Protection for the Wavelength-Shifting Plates	44
5.2.4 Cryogenic Mu Metal Shields	45
5.2.5 Implementation of the Primary System	46
5.3 PMT Testing and Quality Assurance	47
5.4 Secondary System: Acrylic Light Guides for R&D	49
5.5 Calibration	51
5.6 Coupling of PMT Signals to the Anode Wires	52
5.7 Initial Performance of the MicroBooNE Light Collection System	53

6. Electronics and Readout Systems	54
6.1 Cryogenic Low-Noise Electronics	54
6.1.1 CMOS ASIC	54
6.1.2 Cold Motherboards	58
6.1.3 Cold Cables	59
6.1.4 Electronic Calibration	59
6.1.5 Performance Tests	59
6.2 Warm Electronic Amplification	61
6.3 Readout Electronics	62
6.3.1 Data Digitization	64
6.3.2 Data Handling	64
6.3.3 Compression Schemes	65
6.4 PMT Readout Electronics	67
6.4.1 Signal Amplification and Shaping	69
6.4.2 PMT Data Digitization	69
6.4.3 Data Handling and PMT Trigger Generation	69
6.5 Level-1 Trigger Generation	70
6.6 DAQ Design	71
6.7 High-level software trigger	74
7. Infrastructure and Monitoring Systems	75
7.1 Electronics Infrastructure at LArTF	75
7.1.1 AC Power Distribution and Grounding for Low-Noise LArTF Data-taking	76
7.1.2 DC Power Distribution to the MicroBooNE Detector	78
7.1.3 Network, Timing, and Data Distribution for Low-Noise LArTF Data-taking	79
7.1.4 Interlocks and Safety Systems	80
7.1.5 Performance Measurements	81
7.2 Slow monitoring and control system	81
7.3 Beam Monitoring	82
8. UV Laser System	83
8.1 UV Laser Calibration	86
8.2 Laser Source and Optics	86
8.3 Steering System	88
8.4 Performance Tests and Initial Operation	89
9. Conclusion	90

¹ Date: September 26, 2016; Paper Version: 2.0

1. Introduction and Physics Motivation

2 Neutrino detection is entering a new era with a number of large precision neutrino detectors, specifically
3 Liquid Argon Time Projection Chambers (LArTPCs), now in design, construction, data taking,
4 and analysis, both for long and short baseline neutrino oscillation experiments. The **Micro**
5 **Booster Neutrino Experiment**, henceforth referred to as MicroBooNE, is the first large (~ 100 tons)
6 LArTPC to operate in the United States and the second only after ICARUS to operate worldwide.
7 LArTPC detectors combine fine-grained tracking with total absorption calorimetry to provide ex-
8 cellent signal efficiency and background rejection.

9 The MicroBooNE experiment combines a physics program of short-baseline oscillations and
10 neutrino cross-section measurements with development goals to inform larger scale construction
11 of LArTPCs for the long-baseline program. MicroBooNE's principal physics goal is to address
12 the long standing unsolved puzzles generated by short-baseline neutrino oscillation results from
13 past experiments. These include results from accelerator based experiments, LSND and Mini-
14 BooNE, reactor experiments, and radiochemical experiments. The LSND accelerator based oscil-
15 lation experiment observed anti-electron neutrino appearance in an anti-muon neutrino beam. The
16 MiniBooNE experiment [1] also investigated (anti)muon- to (anti)electron-neutrino oscillations
17 and found a significant deviation from the expectation in the number of electron (anti)neutrino
18 candidates at low energy (~ 200 -500 MeV). Other hints come from a re-analysis of the expected
19 reactor antineutrino flux that suggests a deficit of reactor neutrinos [2, 3], and the analysis of cal-
20 ibration data taken by GALLEX and SAGE [4, 5] radiochemical experiments. Interpreting these
21 results through neutrino oscillations suggests a mass squared difference on the order of ~ 1 eV² and
22 an oscillation probability consistent with small mixing, incompatible with the oscillation parame-
23 ters from solar and atmospheric results. These signals can be interpreted as oscillations to sterile
24 neutrinos, which are neutrinos that do not interact via the weak interaction but which can oscillate
25 with the three standard model neutrinos. While each of the short baseline results taken alone does
26 not reach the statistical significance to claim a discovery, combining them together suggests sterile
27 neutrino oscillations or some other phenomena underway at short baselines. Definitive evidence
28 for sterile neutrinos would constitute a revolutionary discovery, with strong implications for par-
29 ticle physics as well as for cosmology. Proposals to address these signals by employing reactor,
30 accelerator, and radioactive source experiments are in the planning stages or underway worldwide.

31 MicroBooNE will address short baseline neutrino oscillations, specifically the MiniBooNE
32 low energy excess result, at Fermi National Accelerator Laboratory (Fermilab). MicroBooNE will
33 be exposed to the 0.5-2 GeV on-axis Booster Neutrino Beam (BNB), the same beam used for the
34 MiniBooNE experiment, at a ~ 500 m baseline, also the same as MiniBooNE, but by employing the
35 LArTPC technology to efficiently separate signal electrons from background photons. In addition
36 to MicroBooNE's signature oscillation analyses, a suite of precision cross-section measurements
37 will be performed, critical both for future LArTPC oscillation experiments and for what can be
38 learned about neutrino interactions in general. In the neutrino interactions from the BNB, multiple
39 interaction processes (quasi-elastic, resonances, deep inelastic scattering) are possible, and compli-
40 cated nuclear effects in neutrino interactions on argon result in a variety of final states. These can
41 range from the emission of several nucleons to more complex topologies with multiple pions, all
42 in addition to the leading lepton in charged-current events. The LArTPC technology employed by

1 MicroBooNE is particularly well suited for complicated topologies because of its excellent particle
2 identification capability and calorimetric energy reconstruction down to very low detection thresh-
3 olds. MicroBooNE will also be supernova live and capable of detecting a galactic supernova, and
4 prepare the analysis of the search for proton decays. For a proton decay search, the experiment will
5 not have a competitive sensitivity due to too small target mass. However, this will be an important
6 proof of principle measurement towards future searches in larger detectors.

7 The MicroBooNE experiment is located 470 m from the BNB production target and 600 m
8 from the NuMI production target. MicroBooNE began operations in late 2015 for an anticipated
9 \sim 3 year data taking run to be followed by data taking as part of the full Short Baseline Neutrino
10 (SBN) program beginning in 2018 with the commencement of operations of the SBND [6] and
11 ICARUS experiments, located at 110 m and 600 m respectively from the BNB production target.
12 MicroBooNE will definitively address whether or not the MiniBooNE low energy excess in neu-
13 trino mode is due to electrons or photons. SBND will look for this low energy excess at the near
14 location (110m) from the production target, and the three detectors combined will cover the entire
15 LSND allowed region in neutrino parameter space to 5σ through ν_e appearance.

16 The LArTPC technique will be used by MicroBooNE at a relatively large scale, so far only sur-
17 passed by the ICARUS T600 detector. The potential of liquified noble gases to be employed as the
18 detection media in particle detectors with high spatial resolution was recognized in the 1960’s [7].
19 Large calorimeters for the measurement of particle energy were then realized by using cryogenic
20 noble liquids as active components [8]. Furthermore, the LArTPC was proposed at CERN by
21 C. Rubbia in 1977 [9] as a detector capable of providing uniform and precise imaging of large
22 volumes.

23 The implementation of the LArTPC idea was extensively developed within the ICARUS ex-
24 periment through an intense R&D program. Various prototype detectors were realized and operated
25 to develop the systems needed for larger physics experiments. Techniques for purification, signal
26 readout electronics, and cryogenics were developed. The largest ICARUS test device had a mass of
27 about 3 tons of LAr [10, 11] and allowed for the collection of large samples of cosmic-ray events.
28 In parallel, a smaller volume detector (50 liters of LAr) was exposed to the CERN WANF neutrino
29 beam allowing the detection of neutrino interaction events for the first time in a LArTPC [12].

30 The largest LArTPC detector built so far is the 600-ton ICARUS T600 detector, which was
31 operated first on the surface exposed to cosmic rays [13] before deployment underground at LNGS
32 for operation in the CNGS neutrino beam. ICARUS measurements have shown that the technique
33 is viable at large scales with a drift length as long as 1.5 m [14 – 18].

34 The success of the construction of the T600 motivated several follow up ideas aimed at reach-
35 ing even higher target masses [19]. A monolithic magnetized large mass device was proposed
36 in [20], based on the scaling up of the ICARUS approach. The ICARUS experience led then to the
37 broader development of the LArTPC concept. A LArTPC design envisioning a single cylindrical
38 volume of 70 m diameter and 20 m height, called GLACIER, was discussed in [21, 22], based on a
39 double-phase readout. This approach eventually evolved to the LAGUNA [23] proposal and to the
40 LAGUNA LBNO [24, 25] conceptual design, aimed at a large detector placed along a long-baseline
41 beam from CERN to an European underground site. In the United States, an analogous multi-kton
42 detector was proposed using conventional single-phase wire readout for the LBNE project [26],
43 aimed at a long-baseline neutrino beam sent from Fermilab to the Sanford Laboratory in South

1 Dakota. The LBNE and LBNO efforts have now largely merged to form the DUNE experiment
2 [27].

3 In parallel, LArTPCs were also considered for short-baseline neutrino experiments, motivating
4 the use of relatively smaller size devices. At Fermilab, the first LArTPC to be successfully oper-
5 ated in the NuMI beam was the ArgoNeuT detector [28] that, despite the relatively small mass of
6 ~ 170 kg, has been able to perform a series of detailed studies on the interaction of medium-energy
7 neutrinos[29 – 32]. Other critical development projects are currently underway at Fermilab such
8 as [33 – 37], all geared towards development of the technology and of analyzing particle interac-
9 tions in the detectors. The goal of the development in the near term is towards the SBN program
10 experiments, and in the farther term, following the recent recommendations of the P5 panel [38],
11 the LBNF project and the DUNE experiment which envisions an internationally coordinated effort
12 for the realization of an intense neutrino beam facility at Fermilab and a far large mass neutrino
13 detector in a long-baseline configuration (> 1000 km).

14 More information on the LArTPC technology can be found in existing reviews (see, e.g., [39]
15 and references therein).

16 **Organization of Document** This document describes the design, construction, and technical de-
17 tails of the MicroBooNE experiment. Section 2 gives a brief review of the LArTPC technique
18 and its implementation in MicroBooNE. Section 3 describes the cryogenic and purification sys-
19 tems which are required for maintaining a stable volume of highly purified liquid argon. The
20 LArTPC detector described in section 4 is the centerpiece of the experiment, providing fine-grained
21 images of neutrino interactions. A light collection system, described in section 5, provides precise
22 timing information by viewing the detector volume and recording signals from the scintillation
23 light that is produced therein. Signals from the light collection system and from the LArTPC are
24 amplified, sampled, and recorded by a custom-designed electronic and readout system, as described
25 in section 6. Section 7 describes the auxiliary instrumentation that monitor and control the detector
26 and all of its associated systems, as well as provide an electrically quiet environment for the exper-
27 iment to operate. Finally, one of the main calibration sources for the experiment is an ultraviolet
28 laser system, described in section 8, that provides the capability to map out the performance of the
29 LArTPC detector. A cosmic ray tagger system, under construction at the time of the writing of this
30 paper, will be sited to beam right and left, and above and below the detector cryostat.

31 **2. Experiment Overview**

32 The MicroBooNE detector at Fermilab in Batavia, Illinois is sited on axis on the BNB, 470 m
33 downstream from the neutrino production target. The BNB delivers a beam of predominantly muon
34 neutrinos with energies peaking at 700 MeV produced primarily from pion decays. MicroBooNE
35 is also exposed to an off-axis component of the NuMI beam [40] produced from pion and kaon
36 decays with average neutrino energies of about 2 GeV and 0.5 GeV respectively. MicroBooNE
37 is located about 600 m downstream from the NuMI neutrino production target. The characteris-
38 tics of the BNB beamline are well measured and understood from many years of data taking and
39 analysis on the MiniBooNE experiment [41], which operated directly downstream of the Micro-
40 BooNE location. Figure 1 shows the arrangement of MicroBooNE with respect to the BNB and

1 NuMI beamlines at Fermilab. The physics program of MicroBooNE will utilize both BNB and
2 NuMI samples. MicroBooNE will also collect data that is out-of-time with either beam, which will
3 be useful for developing analyses (e.g. proton decay searches) relevant for next-generation detec-
4 tors. The primary detector technology employed by MicroBooNE is the LArTPC, whose operating
5 principle is described in this section.

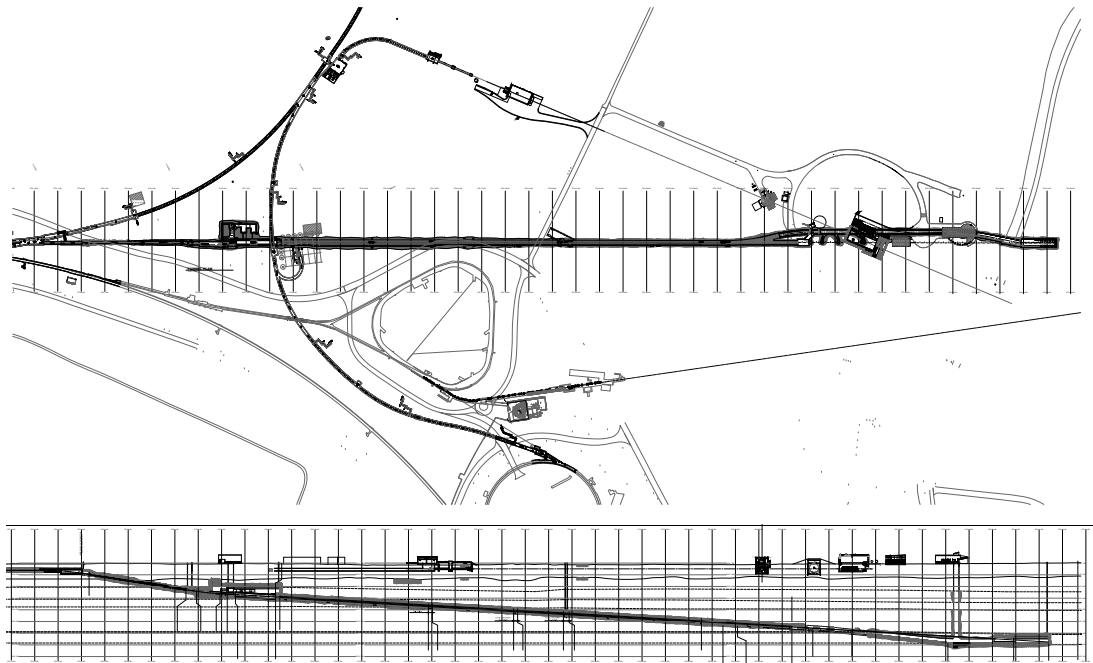


Figure 1: Plan (top) and cross-sectional (bottom) views of MicroBooNE. MicroBooNE is on-axis to the BNB, and off-axis to the NuMI beam.

6 2.1 The MicroBooNE LArTPC

7 Charged particles traversing a volume of highly-purified liquid argon leave trails of ionization elec-
8 trons in their wake and also create prompt vacuum ultraviolet (VUV) scintillation photons. In a
9 LArTPC , the liquid argon is highly purified and the ionization trails are transported practically
10 undistorted over distances of the order of meters [42] under the influence of a uniform electric field
11 in the detector volume, until they reach anode planes located along one side of the active volume.
12 The uniform electric field is created by introducing voltage onto a cathode plane and gradually
13 stepping that voltage down in magnitude across a field cage, which is formed from a series of
14 equipotential rings surrounding the drift volume. The anode plane is arranged parallel to the cath-
15 ode plane, and in MicroBooNE, parallel to the beam direction. There are typically three planes of
16 sense wires comprised of wires with a characteristic pitch, held at a predetermined bias voltage,
17 that continuously sense the signals induced by the ionization electrons drifting towards them. The
18 electrostatic potentials of the sequence of anode planes allow ionization electrons to pass undis-
19 turbed by the first planes before ultimately ending their trajectory on a wire in the last plane. The
20 drifting ionization thus induces signals on the first planes (referred to as Induction planes) and di-

1 rectly contributes to the signals in the final plane (referred to as the Collection plane). Figure 2
 2 depicts a simplified arrangement for a LArTPC.

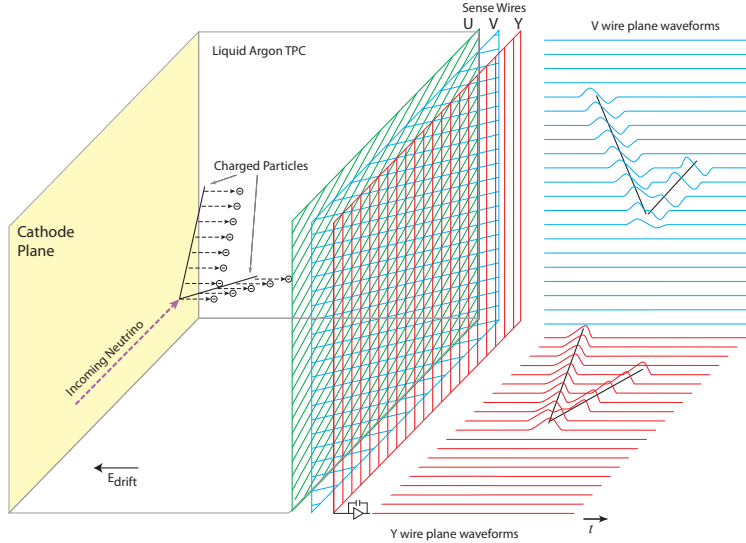


Figure 2: Operational principle of a LArTPC.

3 The charged particle trajectory is reconstructed using the known positions of the anode plane
 4 wires and the recorded drift time of the ionization. The drift time is the difference between the
 5 arrival times of ionization signals on the wires and the time the interaction took place in the detector
 6 (t_0) which is provided by an accelerator clock synced to the beam (e.g. - BNB or NuMI) or from
 7 a trigger provided by the light collection system. The characteristics of the waveforms observed
 8 by each wire provide a measure of the energy deposition of the traversing particles near that wire,
 9 which, when taken as a whole for each contained particle's trajectory, allow for determination of
 10 momentum and particle identity.

11 The scintillation photons are detected by a light collection system that is immersed in the liquid
 12 argon and faces into the detector volume. This system provides signals that can establish the event
 13 t_0 and supplies trigger information to an electronic readout system. The light collection system
 14 signals are vital in distinguishing detector activity that is in-time with the beam (e.g. originating
 15 from beam interactions) from that which is out-of-time (e.g. likely not originating from beam-
 16 related interactions), benefiting event reconstruction. Spatial information transverse to the drift
 17 direction can also be inferred from the light collection signals, further aiding in the reconstruction
 18 of the activity occurring inside the detector.

19 The choice of liquid argon as both the neutrino target and detector medium in LArTPCs is well
 20 motivated, though not without introducing unique considerations for experimental design. Liquid
 21 argon as a target for neutrinos is attractive due to its density, allowing a more compact detector with
 22 a substantial boost in event rate over a comparable detector using less dense media, such as water.
 23 A tradeoff to this aspect is the short radiation length (14 cm) and that the complicated structure

1 of the argon atom, relative to simpler targets such as hydrogen or helium, does introduce nuclear
2 effects that must be considered during data analysis. The cryogenic temperatures at which the
3 noble elements are in the liquid phase also introduces the need for additional design considerations
4 to ensure stable and safe operations.

5 Table 1 lists some of the properties of liquid argon that are salient for LArTPC design. The
6 noble liquids are all characterized by their excellent dielectric properties, able to maintain high volt-
7 ages without suffering electrical breakdown. The long drift lengths over which ionization electrons
8 must travel in large LArTPC detectors requires the presence of a uniform electric field over that
9 distance. This is achieved via the introduction of extremely high voltage ($\mathcal{O}(100$ kV) magnitude)
10 onto the LArTPC cathode; this voltage is suitably maintained due to the dielectric properties of
11 liquid argon and by ensuring the detector components have no sharp edges. The noble liquids are
12 all very bright scintillators, with wavelengths deep in the UV, and also produce copious amounts
13 of ionization. Both the scintillation and the ionization signals are necessary for a robust accounting
14 of the activity occurring inside the LArTPC. Finally, the desire to build LArTPCs on increasingly
15 larger scales, such as those necessary in neutrino experiments, is bolstered by the abundance (1%
16 of atmosphere) and low cost of argon.

Table 1: Selected properties of liquid argon.

Property	Value	Reference
Atomic number	18	
Atomic weight [g/mol]	39.95	
Boiling point [K] @ 1 atm	87.3	[43]
Density [g/cm ³] @ 1 atm	1.4	[43]
Dielectric constant	1.505	[44]
Radiation length [cm]	14.0	[45]
Molière radius [cm]	10.0	[45]
W-value for ionization [eV/pair]	23.6	[46, 47]
Minimum specific energy loss [MeV/cm]	2.12	[45]
Electron transverse diffusion coef. [cm ² /s]	13	[48, 49, 11]
Electron longitudinal diffusion coef. [cm ² /s]	5	[11, 50]

17 The successful implementation of the LArTPC technique depends critically on several factors.
18 The liquid argon must be purified of any electronegative contaminants, such as water or oxygen, to
19 accommodate the very long drift path of ionization through a MicroBooNE-sized LArTPC without
20 significant charge loss. The signals that the ionization electrons create on the anode wires are very
21 small, requiring low-noise electronics to discern signal pulses. The MicroBooNE collaboration
22 has designed and constructed an experiment that addresses all of these considerations, providing
23 critical technological development for the next generation of LArTPC experiments to build upon.

24 2.2 MicroBooNE LArTPC Implementation

25 MicroBooNE’s LArTPC active volume, which is defined as the volume immediately within the
26 confines of the LArTPC field cage, is a rectangular liquid argon volume with dimensions 2.3 m
27 vertical x 2.5 m horizontal x 10.4 m along the beam direction. This is the maximum volume that

1 can be used for physics analyses. The cathode (anode) defines the beam-left (beam-right) side of
2 the active volume. The end of the LArTPC that the beam first encounters is referred to as the
3 “upstream” end, while the opposite end is referred to as “downstream”. Anode plane-to-plane
4 spacing is 3 mm, and each plane has 3 mm wire pitch. The induction plane wires are oriented at
5 $\pm 60^\circ$ relative to vertical, and the collection plane has vertically oriented wires. Field cage loops
6 are employed to maintain uniformity of the electric field across the entire width of the detector,
7 and these loops also act to define the top, bottom, upstream, and downstream sides of the active
8 volume.

9 MicroBooNE uses a right-handed Cartesian coordinate system, with the origin defined to be
10 located on the upstream face of the LArTPC, centered halfway up the vertical height of the active
11 volume and horizontally centered on the anode plane closest to the cathode (the innermost anode
12 plane). In this system, x ranges from 0.0 m at the innermost anode plane to +2.5 m at the cathode,
13 y ranges from -1.15 m on the bottom of the active volume to +1.15 m at the top of the active
14 volume, and z ranges from 0.0 m at the upstream end of the active volume to +10.4 m at the
15 downstream end.

16 The light collection system, which is an array of photomultiplier tubes and scintillator pad-
17 dles, is located directly behind the anode planes on beam-right, facing the detector volume through
18 the anode planes. The LArTPC and light collection system are immersed in liquid argon con-
19 tained within a single-walled cryostat with a 170 ton capacity. Electronics mounted directly on
20 the LArTPC amplify the signals on the wires, which are then passed out of the cryostat for further
21 processing and storage on disk. Table 2 lists the primary detector design parameters of Micro-
22 Boone, and figure 3 shows a schematic of the cross section of the detector. Details of these design
23 parameters and construction of all detector subsystems will be provided in the subsequent sections.

Table 2: Primary detector design parameters for MicroBooNE.

Parameter	Value
LArTPC Dimensions	2.325 m vertically 2.560 m horizontally 10.368 m longitudinally
LArTPC argon mass	90 tons
Total Number of Wires	8256
Drift field	500 V/cm
Light collection	30 8" diameter PMTs 4 scintillator paddles
Cryostat liquid argon capacity	170 tons
Operating temperature	87 K
Operating pressure	2 psig

24 3. Cryogenic System

25 The use of large quantities of highly-purified liquid argon as a detector medium in MicroBooNE
26 requires a sophisticated cryogenic infrastructure that can maintain stable operations for years at a

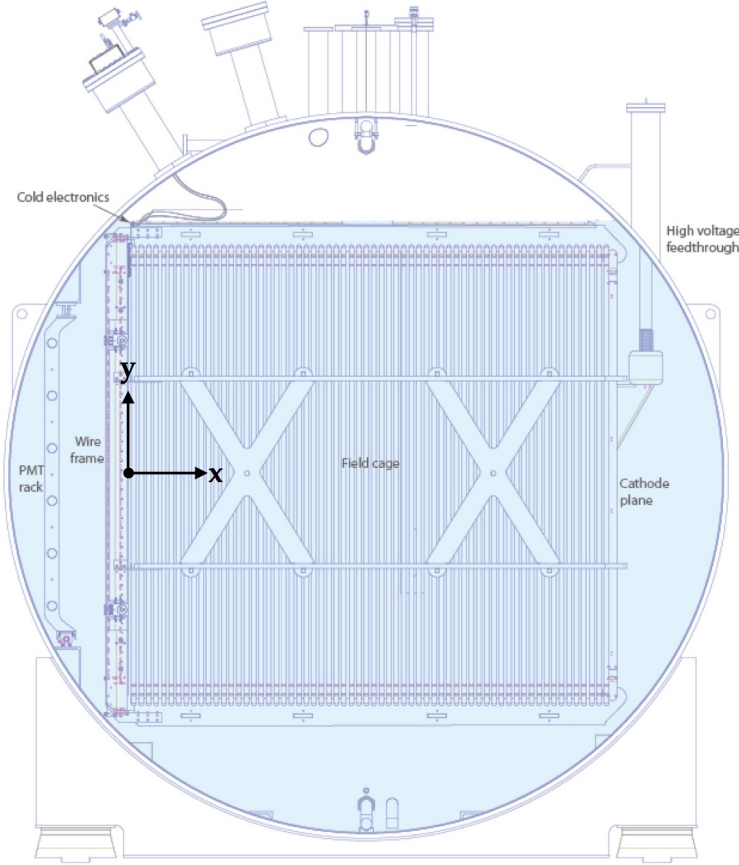


Figure 3: Schematic of the cross section of the MicroBooNE LArTPC. In this view, the beam would be directed out of the page (in the z direction).

time. Not only must the purity of the liquid argon be maintained, but the pressure and temperature gradients within the LArTPC active volume must be tightly controlled as the drift velocity of electrons is dependent on these quantities. A customized cryogenic system that serves these purposes has been built, and the requirements for this system are shown in table 3.

Table 3: Primary design requirements for MicroBooNE cryogenic and purification systems.

Parameter	Value	Motivation
Argon purity	<100 ppt O ₂	MIP identification at longest drift
Argon purity	<2 ppm N ₂	Scintillation light output
LAr Temperature gradient	<1° K	Drift-velocity uniformity
LAr recirculation rate	1 volume change/day	Maintain purity
Cryostat heat load	<15 W/m ²	Minimize convection currents and bubbles
Cryogenic capacity	10 kW	Capacity to deal with expected heat load
Cryostat maximum pressure	30 psig	Determines relief sizing

The MicroBooNE cryogenic system is represented in figure 4. The central component of the

1 system is a cryostat that houses the complete LArTPC and light-collection detector systems. The
2 cryostat is supported by three major subsystems: the argon purification system, the nitrogen re-
3 frigeration system, and the controls and monitoring system. These systems each represent the next
4 generation of LArTPC cryogenic system after the Liquid Argon Purity Demonstrator (LAPD) [35]
5 and make considerable use of the expertise gained during the design and implementation of that
6 apparatus.

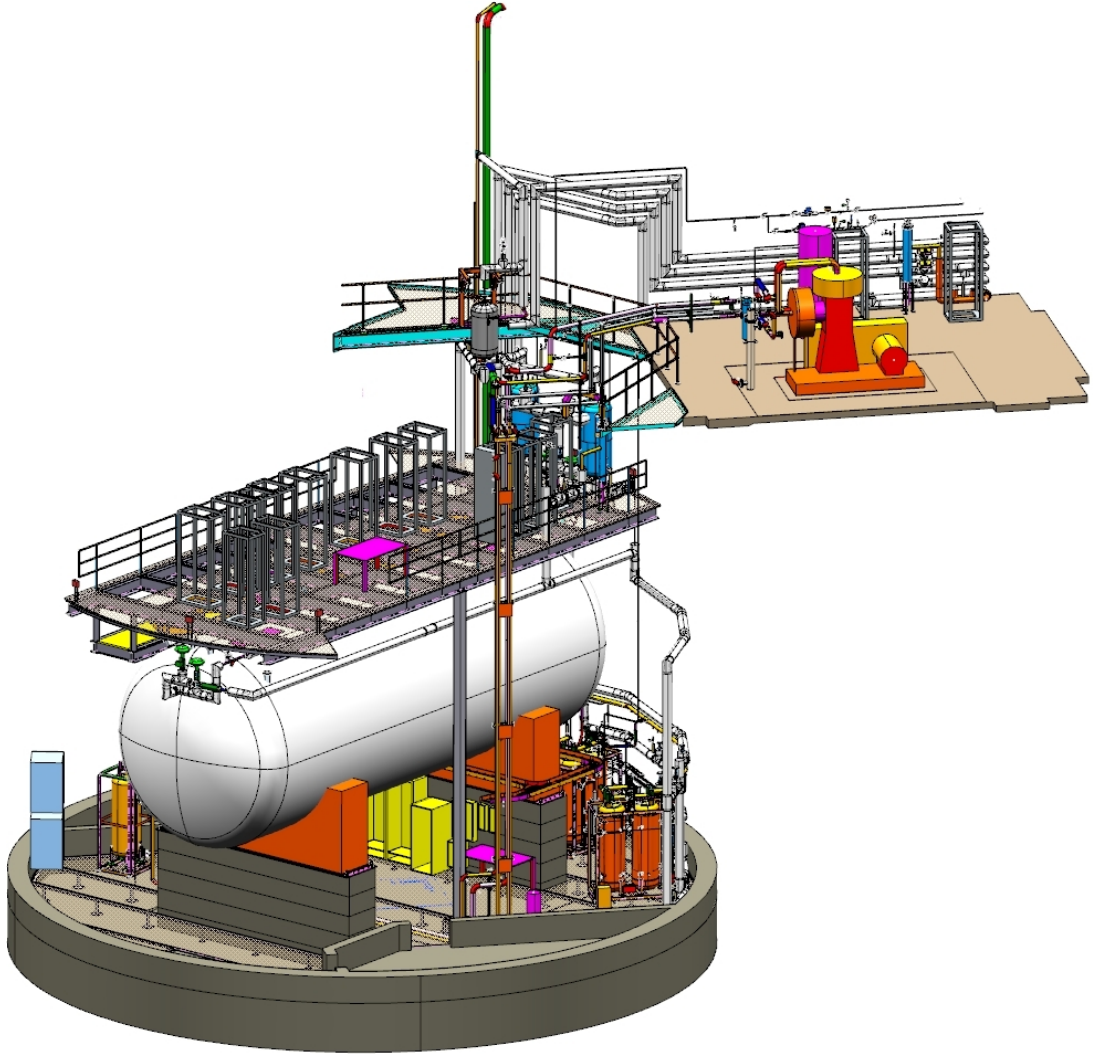


Figure 4: Three-dimensional renderings of the MicroBooNE cryogenic system installed at LArTF.

7 **3.1 Cryostat Design Overview**

8 Three major components make up the MicroBooNE cryostat: a stainless steel (type 304) vessel
9 to contain the liquid argon and all the active detector elements, front and rear supports to carry
10 the weight of the fully loaded cryostat, and foam insulation covering the cryostat outer surfaces.
11 The foam insulation serves to reduce heat input from the ambient environment to a sufficiently low
12 level to prevent large temperature gradients and boiling of the liquid argon. The cryostat and the

1 cryogenic systems are designed to achieve the high-purity liquid argon needed to allow ionization
2 electrons to drift to the anode wires with low probability of capture, and the high degree of thermal
3 homogeneity needed to avoid the introduction of non-constant drift velocities for the ionization
4 electrons. Finally, the outer diameter of the vessel is designed to be the maximum standard size for
5 over-the-road transport.

6 Ionization electrons must not be significantly attenuated, via attachment to electronegative
7 contaminants in the liquid argon, as they drift up to 2.5 m across the active volume. This dictates
8 that the argon be kept free of electronegative contaminants to the level of 100 parts-per-trillion
9 (ppt). The cryostat is designed to minimize outgassing (desorption) and to avoid leakage and
10 diffusion of air into the system. This requirement imposes strict quality assurance demands on all
11 welds for penetrations into the cryostat and on cleaning and handling procedures for the finished
12 vessel. Achieving the required level of purity is accomplished with a purification system, described
13 in section 3.2, that removes electronegative contaminants from the argon during the initial fill and
14 those introduced over time by leaks and outgassing of system components.

15 The electron drift velocity ($v_d = 1600$ m/s at an electric field of 500 V/cm, with a liquid argon
16 temperature dependence $\Delta v_d/v_d = -0.019\Delta T$) must remain constant in magnitude and direction
17 throughout the active liquid argon volume to avoid distortion of the mapping of drift time into the
18 position along the drift (\hat{x}) direction. This requirement limits the allowable temperature variations
19 of the liquid argon to less than 0.1 K and the laminar and turbulent flow rate of liquid argon to
20 less than 1 m/s. These requirements limit fractional errors in velocity, and therefore in the drift-
21 coordinate determination, to be less than 0.1%. The constraints on constancy of drift velocity affect
22 the design by imposing limits on the acceptable heat flux through the insulation.

23 The cryostat is constructed to the latest American Society of Mechanical Engineers (ASME)
24 boiler code requirements [51] and features a single-walled construction, cylindrical shape, and
25 domed caps closing each end, as shown in figure 5. One end was removed for installation of
26 the active detectors, welded back in place upon completion of that task, and then recertified to
27 the ASME code requirements. Upon installation of the sealed cryostat in its final location at the
28 Liquid Argon Test Facility (LArTF), 16 inches of spray-on, closed cell, Polyurethane insulation
29 was applied to the exterior of the cryostat, as shown in figure 6. At LArTF, to avoid ground loops
30 that could interfere with the LArTPC signals, the cryostat vessel is grounded in only one place,
31 allowing it to act as a Faraday cage. This grounding scheme is explained further in section 7.1.

32 The vessel surface has 34 nozzle penetrations for cryogenic and electrical services, detailed in
33 table 4. All nozzles are sealed with feedthroughs, flanges, or pipes that are suitable for operation at
34 the nominal pressure and temperature of the cryostat.

35 **3.2 Liquid Argon Purification Subsystem**

36 The heart of the cryogenic system is the liquid argon purification subsystem. The primary require-
37 ment of this subsystem is to keep the level of electronegative contamination to below 100 ppt of
38 oxygen-equivalent contaminants. This requirement was determined by the physics needs of the
39 experiment, namely the need to keep the attenuation of ionization electrons to less than 20% over
40 the longest drift distance in the LArTPC. In addition to the requirement on the electronegative con-
41 tamination, the system must maintain the level of nitrogen contamination in the argon at less than

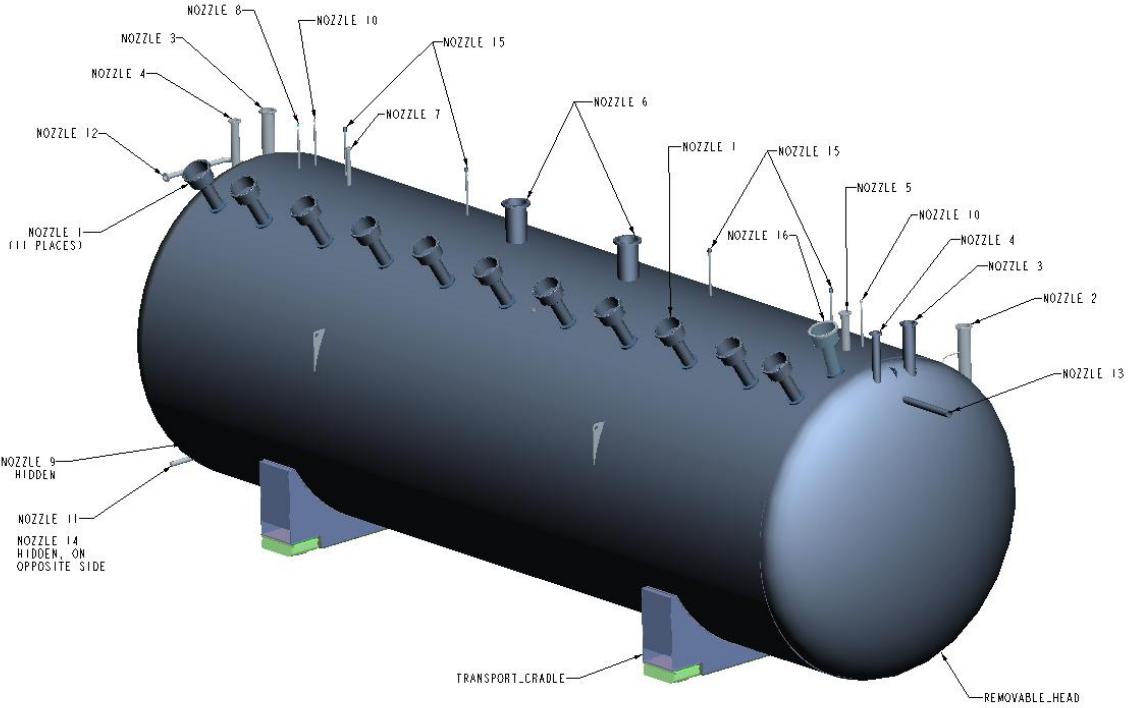


Figure 5: MicroBooNE cryostat with nozzle penetrations labeled.

1 2 parts per million (ppm) [52] to keep the attenuation of the scintillation photons in the argon to a
 2 minimum.

3 The MicroBooNE argon purification subsystem consists of liquid argon pumps and filters that
 4 serve to circulate the argon and remove impurities that degrade the quality of the data collected by
 5 the active detectors. There are two pumps in the system arranged in parallel in order to allow for
 6 continuous recirculation while one pump is being serviced. Similarly, there are two sets of filters
 7 arranged in parallel in the system. Figure 7 schematically depicts the flow of liquid and gaseous
 8 argon in the MicroBooNE cryogenic system.

9 The recirculation pumps are Barber-Nichols [53] BNCP-32B-000 magnetically-driven partial-
 10 emission centrifugal pumps. Each pump isolates the liquid argon from the electric motor. The
 11 impeller, inducer, and driving section of the magnetic coupling each have their own bearings that
 12 are lubricated by the liquid argon at the impeller. The motor is controlled by a variable frequency
 13 drive (VFD) that allows adjustment of the pump speed to produce the desired head pressure and
 14 flow within the available power range of the motor.

15 Each filter skid contains two filters, each having identically-sized filtration beds of 77 liters.
 16 The first filter that the argon stream enters contains a 4A molecular sieve supplied by Sigma-
 17 Aldrich [54] that primarily removes water contamination but can also remove small amounts of
 18 nitrogen and oxygen. The second filter contains BASF CU-0226 S, a highly-dispersed copper ox-
 19 ide impregnated on a high-surface-area alumina, which removes oxygen [55] and, to a lesser extent,
 20 water. Thus, the oxygen filter is placed downstream of the molecular sieve to maximize oxygen fil-
 tration. The oxygen-filtering media must be reduced to copper with the procedure described below

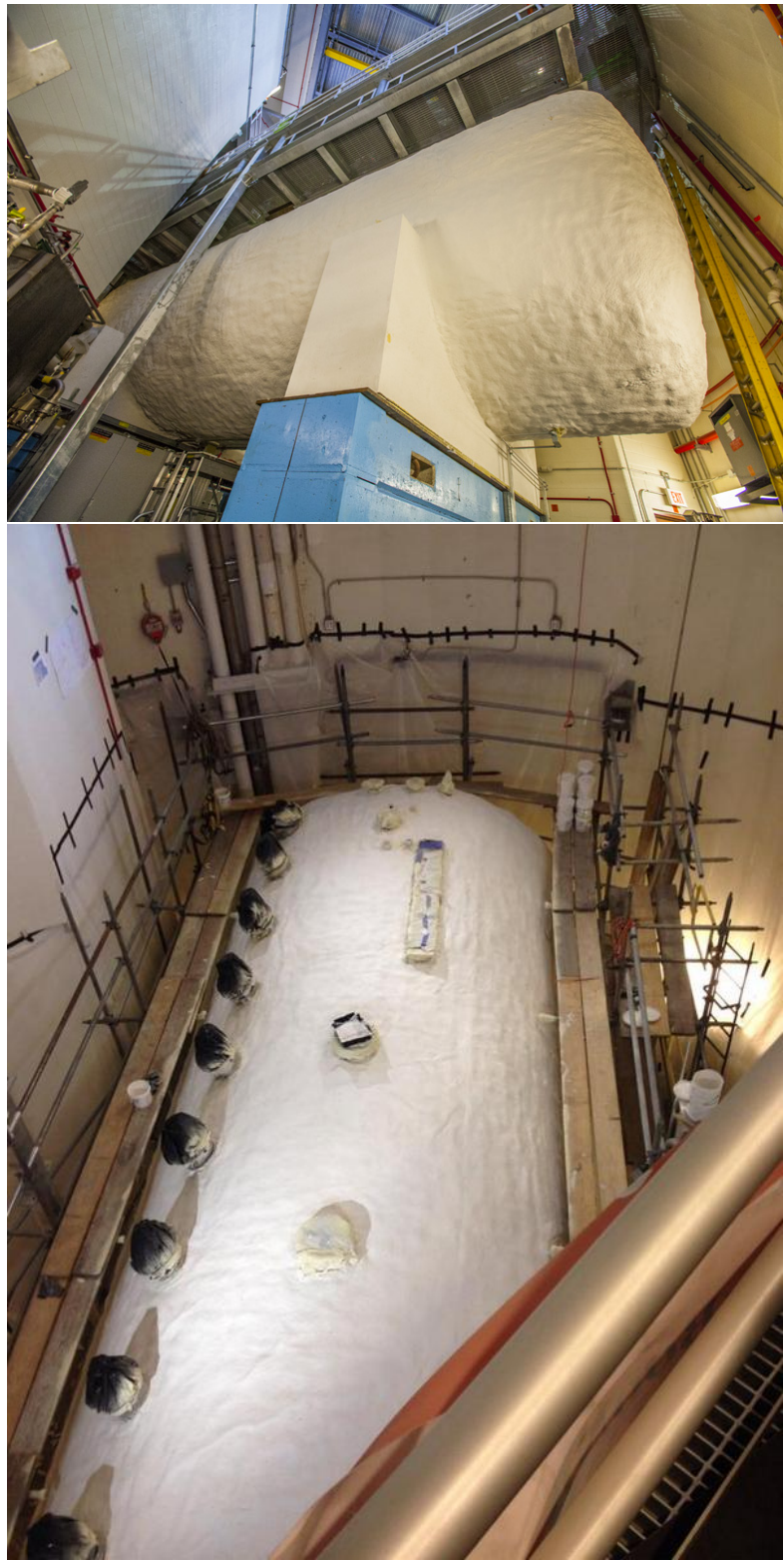


Figure 6: Photographs of the cryostat after application of exterior foam insulation.

Table 4: List of nozzle penetrations in MicroBooNE cryostat. CF=ConFlat flanges, RFWN=raised face weld neck flanges.

Nozzle ID	Function	Flange
N1A-N1K	LArTPC Signal Feedthrough	14" CF
N2	LArTPC HV Feedthrough	8" CF
N3A-N3B	Purity Monitor	8" CF
N4	Temperature Signals	6" CF
N5	Safety Vent	4" RFWN
N6A-N6B	Vacuum Pump-Out	10" RFWN
N7	Condensor	3"
N8	Top Instrument Port	3/4"
N9	Bottom Instrument Port	3/4"
N10A-N10B	Liquid Level Probe	3/4"
N11	Gas Circulation In	2"
N12	Gas Circulation Out	2"
N13	From LAr Filters	3"
N14	To LAr Pumps	2"
N15A-N15B	Laser Calibration	2-3/4" CF
N16	PMT Signal Feedthrough	14" CF
N17	Spare	6" CF
N18	Temperature Signals	6" CF
N19	Spare	6" CF

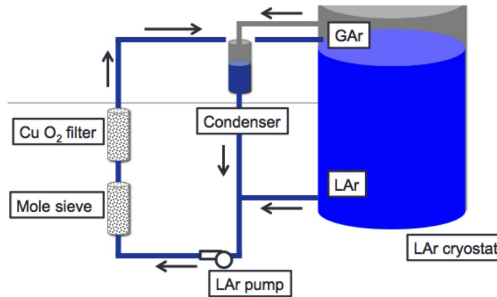


Figure 7: Flow diagram of argon in MicroBooNE, showing direction of liquid and gaseous argon in the cryogenic system. Gaseous argon from the cryostat is condensed and directed through the purification subsystem. Liquid argon drawn from the cryostat volume is directed into the purification subsystem. **NOTE: Update with better figure!**

- ¹ before it can remove oxygen from the liquid argon. The filters are insulated with vacuum jackets and aluminum radiation shields. The metallic radiation shields were chosen because the filter regeneration temperatures, described below, would damage traditional aluminized mylar insulation.
- ² Pipe supplying the filter regeneration gas is insulated both inside the filter vacuum-insulation space and outside the filter with Pyrogel XT which is an aerogel-based insulation [56] that can withstand

1 temperatures up to 650°C.

2 The filters are regenerated *in situ* using heated gas, by a procedure developed for LAPD. The
3 filters are regenerated using a flow of argon gas that is heated to 200°C, supplied by a commercial
4 500 liter liquid argon dewar. Once the argon gas reaches 200°C, a small flow of hydrogen is mixed
5 into the primary argon flow and exothermically combines with oxygen captured by the filter to
6 create water. Too much hydrogen mixed in with the primary argon flow would induce temperatures
7 that are sufficiently high to damage the copper-based filter media. The damage is induced by
8 sintering of the copper, which reduces the available filter surface area. Thus, precautions are taken
9 to maintain a hydrogen fraction below 2.5% of the heated gas mixture. During the heated gas
10 regeneration, five filter-bed temperature sensors monitor the filter-material temperature and the
11 water content of the regeneration exhaust gas is measured. To remove any remaining trace amounts
12 of water, the filters are then evacuated using turbomolecular vacuum pumps while they cool.

13 A particulate filter with an effective filtration of 10 microns, positioned between the cryostat
14 and the filter skids, prevents any debris in the piping from being introduced into the cryostat.
15 The particulate filter consists of a commercial stainless steel sintered-metal cylinder mounted in a
16 custom cryogenic housing and vacuum jacket. Filtration is accomplished by flowing liquid argon
17 to the interior, then outward through the walls, of the sintered-metal cylinder. Flanges on the argon
18 piping, along with flanges and edge-welded bellows on the vacuum jacket, allow removal of the
19 particulate filter.

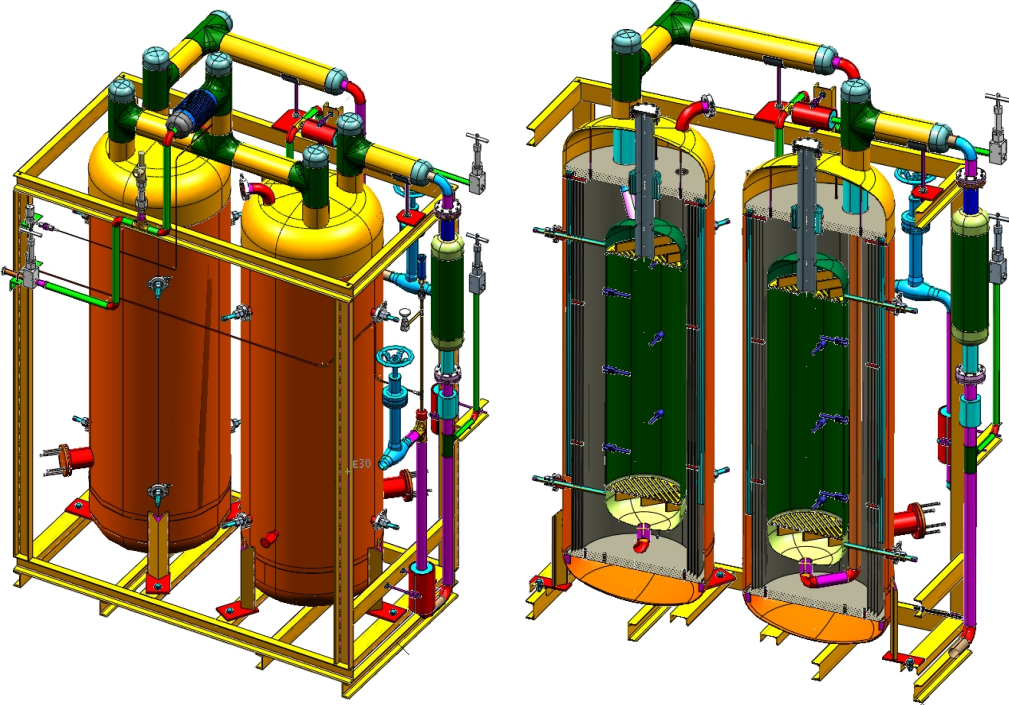


Figure 8: Three-dimensional rendering of a MicroBooNE filter skid. The left drawing shows the full skid, while the right drawing shows a cut-away of the vessels.

20 The argon-purification piping is 1.0 in diameter stainless steel that was pre-insulated by the

1 manufacturer with 10.2 cm of polyurethane foam. During the fabrication process, all piping was
2 washed with distilled water and detergent to remove oil and grease, then cleaned with ethanol.
3 All valves associated with the argon-purification piping utilize a metal seal with respect to am-
4 bient air, either through a bellows or a diaphragm, to prevent the diffusion of oxygen and water
5 contamination. The exhaust side of each relief valve is continuously purged with argon gas to
6 prevent diffusion of oxygen and water from ambient air across the o-ring seal. Where possible,
7 ConFlat flanges with copper seals are used on both cryogenic and room-temperature argon piping.
8 Pipe flanges in the system are sealed using spiral-wound graphite gaskets. Smaller connections are
9 made with VCR fittings with stainless steel gaskets.

10 **3.3 Nitrogen Refrigeration**

11 The cryostat and purification systems that contain the liquid argon are subject to heat load from
12 the environment, as well as from the active detectors that have electrical power enabled. To keep
13 these systems operating at a stable temperature and pressure, a liquid nitrogen refrigeration system
14 is present to provide the necessary cooling power. The liquid nitrogen system contains two con-
15 densers that are arranged in parallel. One of these is utilized for normal operations and one serves
16 as a backup on standby. Each condenser contains two liquid nitrogen coils, an inner and an outer,
17 with the gas argon on the shell side, as shown in figure 9. Typically only one coil is actively running
18 and the second can be manually activated during situations where the system heat load is higher
19 than usual. Each condenser is sized to handle a heat load of approximately 9.5 kW. With the vessel
20 full of liquid argon and no pump or liquid argon circulation running, the condenser uses 600-650
21 gallons of liquid nitrogen per day, which equates to a 3.9 kW system heat load. Once liquid argon
22 begins circulating using the pumps, this usage rate will increase by 50-100%.

23 **3.4 Controls and Purity Monitoring**

24 MicroBooNE makes use of resistive thermal devices (RTDs) to measure temperatures throughout
25 the experimental infrastructure. Twelve RTDs are located along the walls of the cryostat, and
26 another ten RTDs are mounted inside screws attached to the structure of the LArTPC. Each of
27 the filter vessels in the purification system contain nine RTDs. The RTDs within the filter vessels
28 prevent overheating which could potentially occur during filter regeneration with heated argon-
29 hydrogen gas.

30 Liquid argon contaminations ranging between 300 and 50 ppt oxygen equivalent can be mea-
31 sured using double-gridded ion chambers, henceforth referred to as purity monitors, immersed in
32 liquid argon. The design of the purity monitors is based on the design presented by Carugno et
33 al. [57]. A thorough description of the purity monitors, the data-acquisition hardware and software
34 used in LAPD can be found in [35]. MicroBooNE uses the same type of purity monitors, and the
35 same data-acquisition hardware and software.

36 A measure of the electronegative impurities is made with the purity monitor by examining the
37 fraction of electrons generated at the purity monitor cathode that subsequently arrive at the purity
38 monitor anode (Q_A/Q_C) after a drift time t . The ratio of (Q_A/Q_C) is related to electron lifetime, τ ,
39 such that

$$Q_A/Q_C = e^{-t/\tau}. \quad (3.1)$$

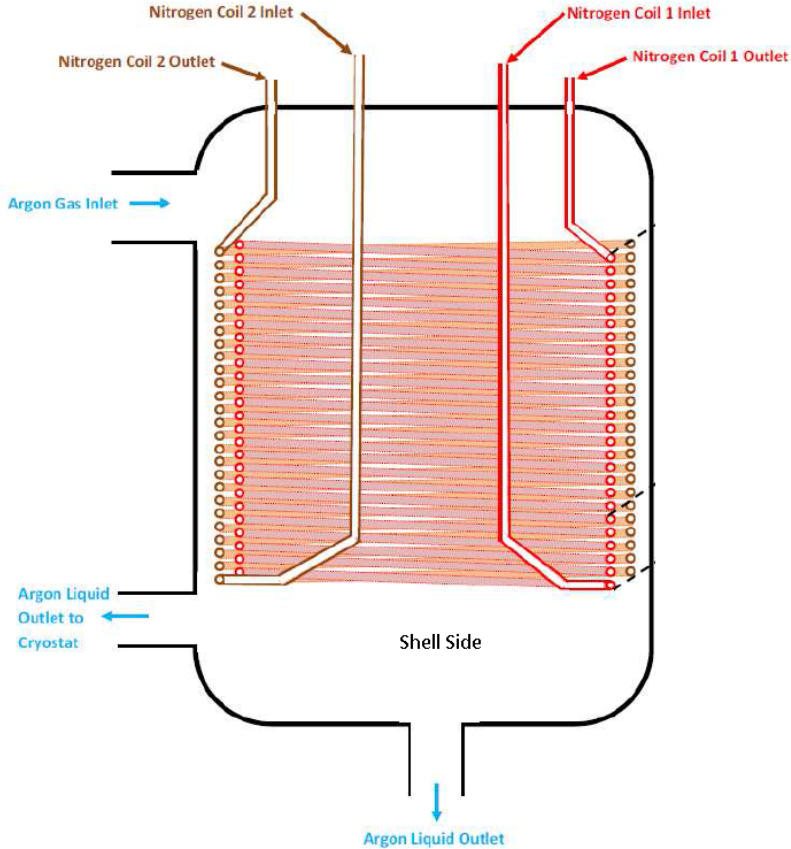


Figure 9: Diagram of a condenser.

Measurement of liquid argon purity in the MicroBooNE cryogenic system are provided by three purity monitors of varying lengths. One purity monitor with a drift distance of 50 cm sits in a vessel just downstream of the filters and is used to monitor filter effectiveness. Two purity monitors, one with a drift distance of 19 cm and the other with a drift distance of 50 cm, sit within the primary MicroBooNE vessel at each end of the LArTPC.

4. Liquid Argon Time Projection Chamber

The MicroBooNE LArTPC drifts and collects charge to produce fine-grained images of the ionization that is liberated by charged particles traversing a volume of highly-purified liquid argon. This section describes the design and implementation of the LArTPC in the experiment.

The LArTPC is composed of three major structures: the cathode, the field cage, and the anode. A negative voltage is introduced via a feedthrough passing through nozzle N2 on the cryostat and applied at the cathode, which defines an equipotential surface. This cathode voltage is incrementally stepped down in magnitude by means of a voltage divider chain spanning the field cage, creating a region of uniform electric field within the LArTPC. Opposite the cathode, and oriented parallel to it, are the anode wire planes: two induction planes (referred to as the “U” and “V”

1 planes) with wires oriented at ± 60 from vertical, followed by one collection plane (referred to as
 2 the “Y” plane) with vertically-oriented wires. The wires of the anode planes are the sensitive ele-
 3 ments that detect the ionization created by charged particles traveling through the LArTPC. Figure
 4 10 depicts the assembled MicroBooNE LArTPC after insertion into the cryostat, showing details
 5 of the cathode, field cage, and anode plane. Table 5 lists the main parameters of the MicroBooNE
 6 LArTPC, which will be described in detail in this section.

Table 5: MicroBooNE LArTPC design parameters and nominal operating conditions.

Parameter	Value
LArTPC (active) dimensions ($h \times w \times l$)	2.325 m \times 2.560 m \times 10.368 m
LArTPC (active) mass	90 tons
# Anode planes	3
Anode planes spacing	3 mm
Wire pitch	3 mm
Wire type	SS, diam. 150 μm
Wire coating	2 μm Cu, 0.1 μm Ag
# wires (total)	8256
# Induction0 plane (U) wires	2400
# Induction1 plane (V) wires	2400
# Collection plane (Y) wires	3456
Wire orientation (w.r.t. vertical)	+60°,-60°,0° (U,V,Y)
Cathode voltage (nominal)	-128 kV
Bias voltages (U,V,Y)	-200 V, 0 V, +440 V
Drift-field	500 V/cm
Max. Drift Time, Cathode to U (at 500 V/cm)	1.6 ms
# Field-cage steps	64
Ring-to-ring voltage step	2.0 kV

7 4.1 Cathode

8 The cathode is assembled from 9 individual stainless steel sheets (Type 304, 0.09 inches thick) that
 9 are fastened to a supporting frame by hex button head stainless steel screws. The outer edge of
 10 the cathode frame consists of round stainless steel tubes of 2.0 inch outer diameter and 0.125 inch
 11 wall thickness. Within this outer edge, square tubes with 2.0 inch \times 2.0 inch cross-sectional area,
 12 and 0.125 inch wall thickness, are fastened together with button head screws, forming a support
 13 structure upon which the cathode sheets are attached. The individual components of the support
 14 structure are further welded together to eliminate sharp features from this high-potential surface.
 15 The exterior frame and support structure of the cathode, and also an interior view, are shown in
 16 figure 11. The cathode plane sheets are shimmed according to survey data to make the cathode as
 17 flat and as parallel to the anode frame as possible. Flatness of the cathode is evaluated relative to
 18 a best fit plane of survey data (more than 10000 survey points recorded with a laser tracker). The
 19 largest deviations of the cathode from the best fit plane are +6.6 mm and -6.5 mm. Approximately

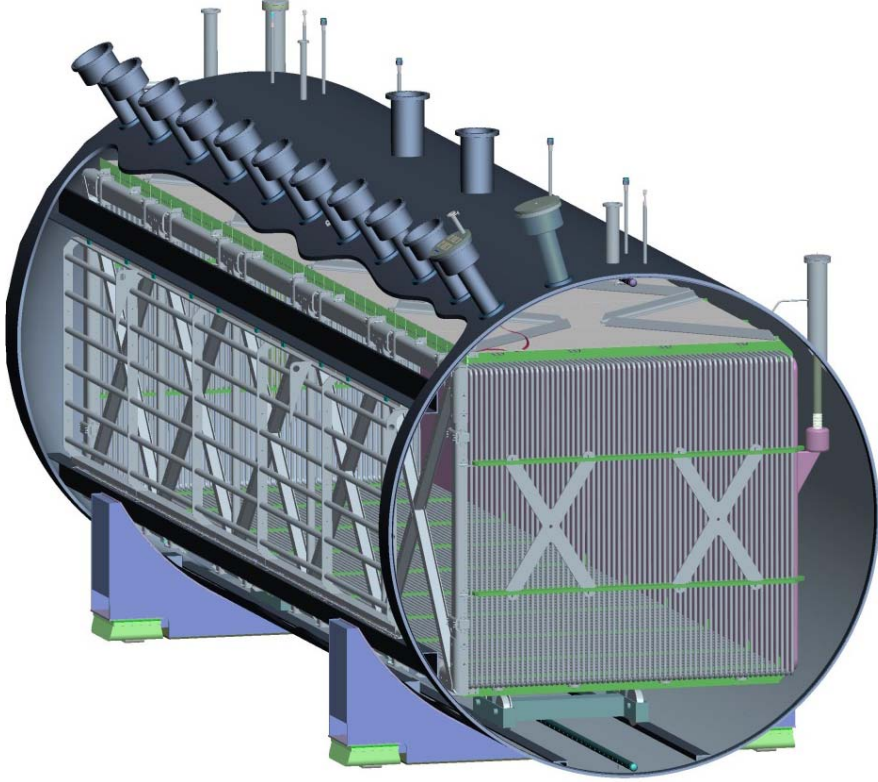


Figure 10: Schematic diagram of the MicroBooNE LArTPC , depicted as it is arranged inside the cryostat.

1 55% of the measured survey points fall within +/-3 mm of the best fit plane, and more than 90% of
 2 the points fall within ± 5 mm. Figure 12 shows the results of the survey, with deviations from flat
 3 represented as color-coded data extending away from the nominal plane of an ideal cathode.

4 4.2 Field Cage

5 The field cage encloses the volume between the cathode plane and the anode wire planes, and in
 6 doing so creates a region with a uniform electric field. The volume defined by the interior of the
 7 field cage, bounded by the anode and cathode planes, is referred to as the “active” volume. The field
 8 cage structure consists of 64 individual thin-walled stainless steel tubes (1.0 inch OD, 0.065 inch
 9 wall thickness), each shaped into a rectangular loop framing the perimeter of the active volume.
 10 These 64 loops are mounted parallel to the cathode and anode planes, as shown in figure 11, and
 11 are held in place by a G-10 rib support structure. Each field cage loop is electrically connected
 12 to its neighbors via a resistor divider chain (described in following section), causing each loop to
 13 operate at a different electrical potential which in turn maintains a uniform electric field between
 14 the cathode and anode planes. For a nominal -128 kV cathode voltage, the difference in potential
 15 between adjacent field cage loops is 2 kV, ramping down the total potential in equidistant steps
 16 from cathode to anode. The distance from center-to-center of adjacent field cage loops is 4.0 cm.

17 Each field cage loop is assembled from 6.77 feet long vertical pipes on the upstream and
 18 downstream ends of the LArTPC , and on the top and bottom from two 17 feet long horizontal pipes



Figure 11: Top: Exterior view showing the cathode frame and structural supports to which cathode sheets are fastened. Bottom: Interior view of cathode plane as viewed from the upstream end of the LArTPC , showing cathode sheets.

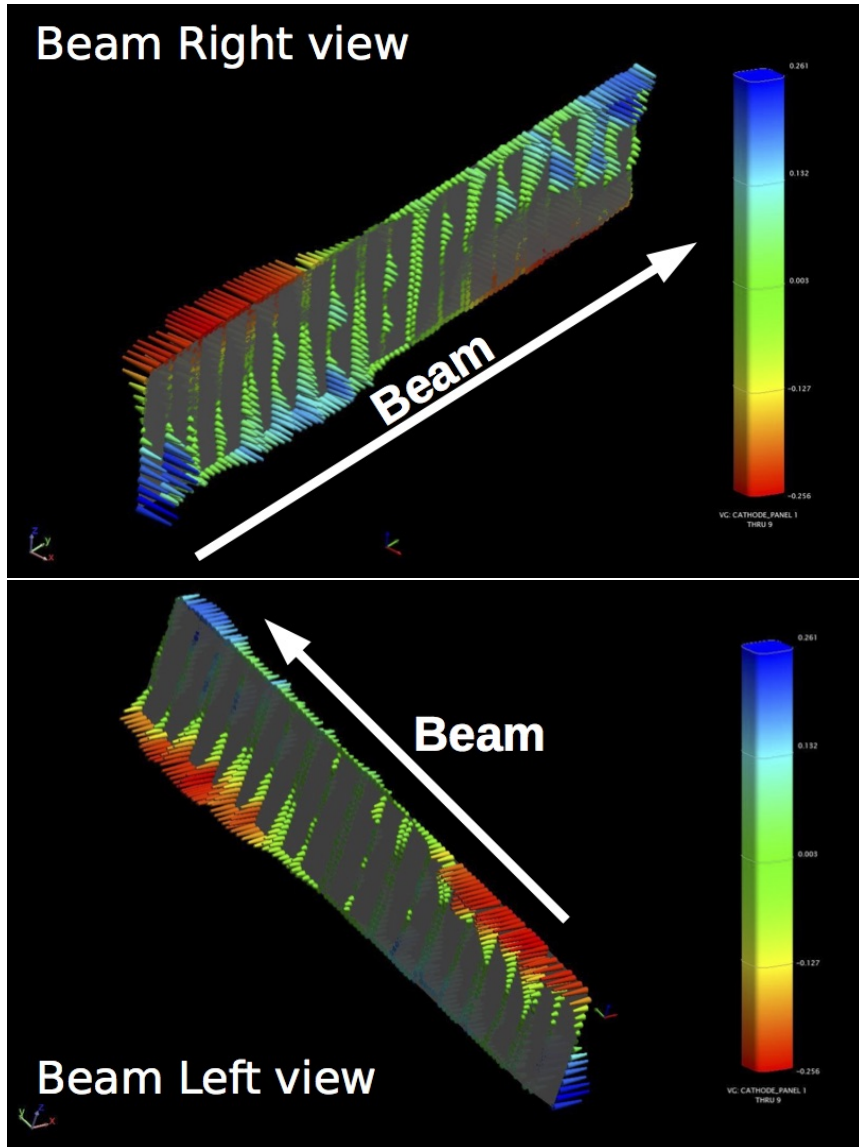


Figure 12: Survey results for interior (top) and exterior (bottom) of the cathode after shimming. Color scale extends from -0.256 cm (red) to +0.261 cm (blue).

1 connected by a stainless steel coupling in the center. Each tube has venting holes approximately
 2 every 6 inches so that they fill with liquid argon and allow air and gaseous argon to escape during
 3 cryostat cool down and filling.

4 The four corners of each field cage loop are curved with a radius of 2.0625 inch. Each corner
 5 is formed by three parts: two couplings and an elbow, shown in figure 13. The couplings make the
 6 connections between the pipes and the elbow. The thin-walled tubes and elbows slip-fit over the
 7 ends of the couplings with a 0.88-inch overlap. Each coupling has two 6-32 NC tapped holes and
 8 the connections to the adjoining pieces are made by hex head button screws and lock washers.

9 In order to avoid electrical breakdown between the inner cryostat surface and field cage parts
 10 at high potential on or near the cathode, the electric field strength is minimized at the corners and

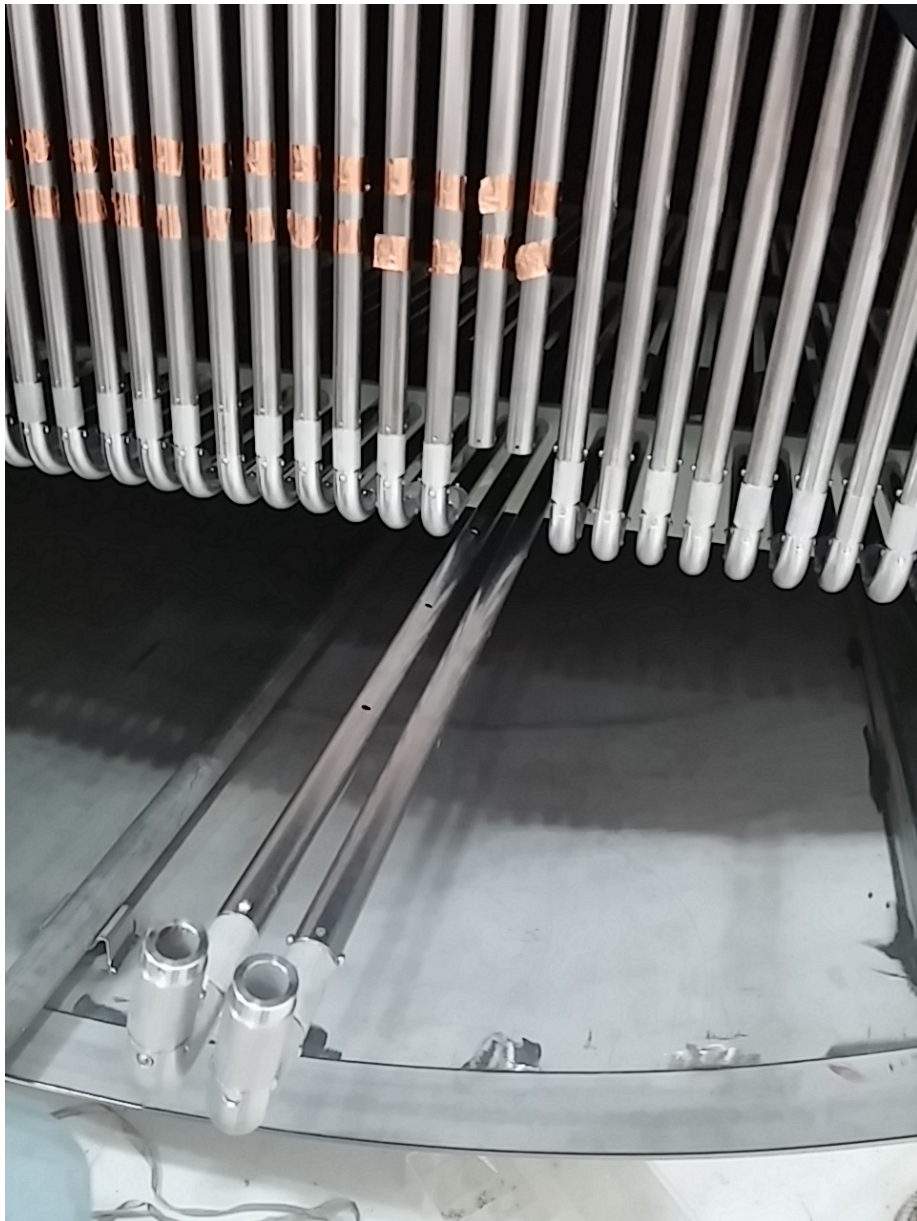


Figure 13: Field cage loops, with two partially disassembled to show elbow and couplings.

edges of the field cage. Loop 0 is the cathode frame, which is at the same potential as the cathode plane sheets attached to it. The frame is made from larger diameter piping of 2 inch OD, and it has a slightly smaller circumference than the other field cage loops, as shown in figure 14. The elbow of loop 1 has a specially designed shape in order to minimize the electric field potential, and the elbow of loop 2 has a softer radius of curvature than the standard elbows. For all three of these loops (loop 0, 1, and 2), connections at corners and joints are made by welding instead of screws to avoid sharp edges that would result in higher electric fields and greater chance of electrical breakdown.

Another precaution to minimize the electrical field between the loops and the cryostat surface is the positioning of the coupling screws: for the first 20 loops, the screws are positioned on the



Figure 14: Field cage loops closest to (and including) the cathode are modified to reduce sharp edges that would result in higher electric fields.

1 sides facing the screws of the neighboring loops instead of facing inward to the LArTPC active vol-
2 ume and outward toward the grounded cryostat surface. Hex head button screws and lock washers
3 are also used here in order to minimize sharp metal edges.

4 **4.2.1 Resistor Divider Chain**

5 A resistor divider chain installed across the field cage loops steps the voltage down in magnitude
6 from the cathode plane to the anode wire plane in equidistant steps. For a nominal value of -128 kV
7 on the cathode, this results in a potential difference of 2 kV between each pair of loops. The value

1 of the equivalent resistance between loops within the divider chain was chosen to be low enough
2 such that the current flow through the divider circuit is much greater than the signal current flowing
3 through the LArTPC . The signal current in this case is the total energy deposited by cosmic rays,
4 and is estimated to be <50 nA. An equivalent resistance of 250 M Ω between each pair of field cage
5 loops, corresponding to a current flow of 8 μ A, was chosen.

6 The voltage divider chain is mounted on the inside of the field cage at the upstream end of the
7 detector. The couplings at the top corner of each field cage loop have additional holes facing the
8 inside of the field cage, where the resistors are mounted. On the first 16 field cage loops, pairs of
9 Metallux HVR 969.23 499 M Ω resistors (rated to 23 W, 48 kV in air) are mounted electrically in
10 parallel to establish the beginning of the voltage divider chain. On the remaining loops, thick-film
11 Ohmite Slim-Mox 104E metal-oxide epoxy-coated resistors with a lower power and voltage rating
12 (1.5 W, 10 kV in air) are used. Extensive testing was done on these two types of resistors [58]. For
13 redundancy, the desired 250 M Ω total resistance between each pair of field cage loops is composed
14 of four individual 1 G Ω Slim-Mox 104E resistors placed electrically in parallel and attached to a
15 printed circuit board. Printed circuit boards span across eight field cage gaps and therefore have
16 eight 250 M Ω resistances in series, shown in figure 15. The electrical connection between the
17 boards and each field cage loop is made by metal contact pads on the back side of the boards, held
18 in electrical contact with the field cage tube by a button-head hex screw and lock washer.

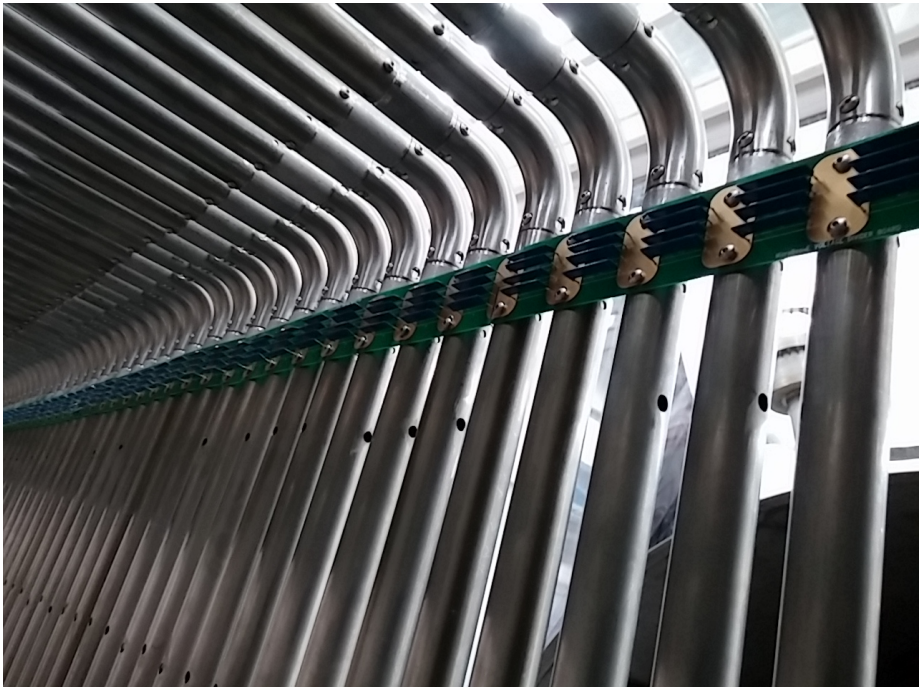


Figure 15: The Ohmite Slim-Mox 104E resistors arranged in parallel sets of four on printed circuit boards that span eight field cage tubes.

19 While the designed operating voltage difference across each resistor in the detector is 2 kV
20 with a power flow of 4 mW, there is a slight possibility that these values could temporarily exceed
21 the rating of the resistors in the case of discharge between the cathode plane or field cage loops and

1 the cryostat wall, through the bulk liquid argon. Recent studies [59] have shown that the value of
2 the minimum breakdown electrical field decreases with the increasing argon purity; for purities as
3 high as that required in the MicroBooNE detector, breakdown has been observed at electric fields
4 as low as 40 kV/cm.

5 The field cage behaves like a capacitance network at high frequencies. Based on measurements
6 and simulations, the total energy stored inside the field cage when fully charged is estimated to be
7 approximately 24 J. In the case of a discharge between the cryostat and the cathode or one of the
8 field cage loops close to the cathode, simulations show that voltages of up to 80 kV peak, with
9 a discharge time constant of a few seconds, can develop across the resistors. The observed peak
10 voltages in such discharge scenarios decrease the further the breakdown occurs from the cathode,
11 such that discharges occurring between the cryostat and field cage loops 32 through 63 do not
12 exceed the 10 kV rating of the resistors.

13 In order to protect the resistors near the cathode from damage which could potentially render
14 the field cage inoperable, two strategies have been implemented. First, due to the knowledge
15 obtained in the breakdown electrical field studies mentioned before, on the first 16 field cage loops
16 near the cathode the Ohmite Slim-Mox 104E resistors are replaced by 499 M Ω Metallux HVR
17 969.23 resistors that have a higher voltage rating of 48 kV. An extensive study of resistor breakdown
18 in liquid argon of several resistor brands and models [58] has revealed that the breakdown voltage
19 observed in liquid argon exceeds the rating in air substantially for all resistors. No breakdown
20 has been observed up to 32 kV for the Ohmite Slim-Mox 104E resistor. For the Metallux HVR
21 969.23 resistors, no breakdown has been observed up to the limit of the test apparatus of 130 kV.
22 Since the Metallux HVR 969.23 resistors are significantly larger physically than the loop-to-loop
23 distance, they are mounted diagonally between each pair of field cage loops. They are held by
24 copper brackets, which are attached to studs welded onto the field cage tubes, shown in figure 16.

25 The second type of protection installed for all resistors on field cage loops 1 through 32 is a
26 surge protection circuit. The chosen surge protection devices are designed to short the circuit in
27 the case of a voltage spike, which protects any other electrical components installed in parallel.
28 Below their clamping voltage, they exhibit a very high resistance and do not influence the circuit.
29 The behavior of Gas Discharge Tubes (GDTs) and varistors in liquid argon has been studied exten-
30 sively for application in the MicroBooNE field cage [60]. The surge protection device chosen is a
31 Panasonic ERZ-V14D182 varistor with a clamping voltage of 1700V. In order to obtain a very high
32 resistance in normal operation and a clamping voltage above the 2 kV in normal operation mode,
33 three of these devices are mounted in series across a block of four Slim-Mox 104E or two Metallux
34 969.23 resistors. These additional varistor boards make electrical contact with the field cage via
35 brass mounting brackets that are fastened to the field cage with button head screws, as shown in
36 figure 17.

37 **4.3 Anode**

38 The anode frame holds the induction and collection plane sense wires at tension and provides
39 overall structural support for the beam-right side of the LArTPC. Individual sense wires for all
40 anode planes are held in place by wire carrier boards, which are printed circuit board assemblies
41 that locate the wires as well as provide the electrical connection to the electronic readout system of
42 the experiment.

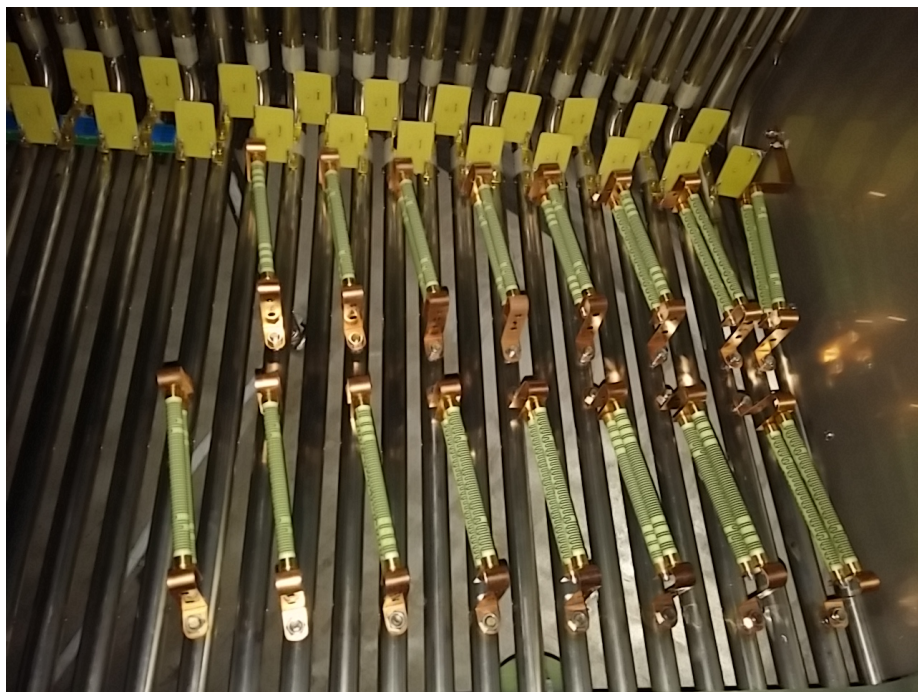


Figure 16: The Metallux HVR 969.23 resistors mounted on the 16 field cage loops closest to the cathode.



Figure 17: Surge-protecting varistors are installed in parallel with the voltage divider resistors for the first 32 field cage loops. Here, they are shown mounted on small boards in sets of 3, and attached to the field cage by means of 6-32 hex button head screws.

1 4.3.1 Mechanical structure

- 2 The anode frame is comprised of a stainless steel C-channel hosting adjustable tensioning bars to
3 which the wire carrier boards are attached. The C-channel and tensioning bar assembly is depicted
4 for one corner of the anode frame in figure 18. Wire carrier boards attach to precision alignment
5 pins distributed along the length of the tensioning bars.

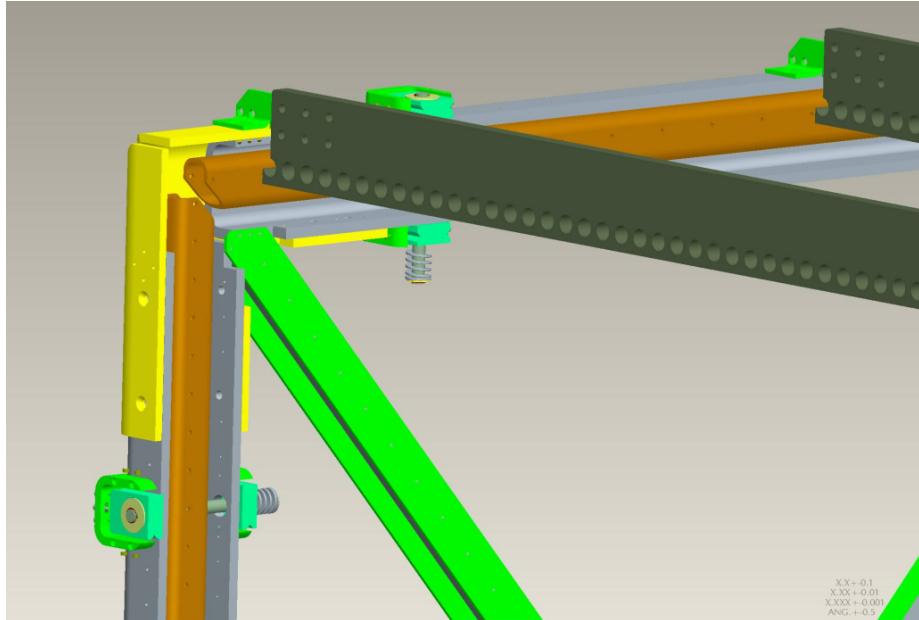


Figure 18: Rendering of the anode frame assembly. The C-channel is depicted in gray, and the adjustable tensioning bar assembly is shown in orange.

6 4.3.2 Wire winding and quality assurance

- 7 The three anode planes are constructed from wire carrier boards that have had individually-prepared
8 wires attached to them in groups of 16 (for the U- and V- angled planes) or 32 (for the vertical Y-
9 plane). Consistent quality in wire preparation was achieved by a semi-automated winding machine,
10 which terminated the ends of each wire via wrapping around 3 mm diameter brass ferrules as shown
11 in figure 19. Each wire was tested for strength by being placed on a tensioning stand where a load
12 of 2.5 kg (more than 3 times the nominal load of 0.7 kg) was applied for 10 minutes, ensuring that
13 the wire preparation did not leave any weaknesses that could result in a breakage later on. Upon
14 successful completion of the quality assurance testing for each wire, it was placed onto a wire
15 carrier board, shown in figure 20

16 When installed, the wires make contact with gold pins positioned on the wire carrier board,
17 and these pins are connected to a trace that routes to the cold electronics described in section 6.1.
18 After fully filling a wire carrier board with wires, a cover plate was installed and press-fit rivets
19 were installed to hold the assembly together. The assembled wire carrier board was then placed
20 onto a tension stand, to reapply a 2.5 kg tension/wire to the whole board for 10 minutes. This is
21 to ensure that the wires were not weakened during the board assembly process. The tension stand

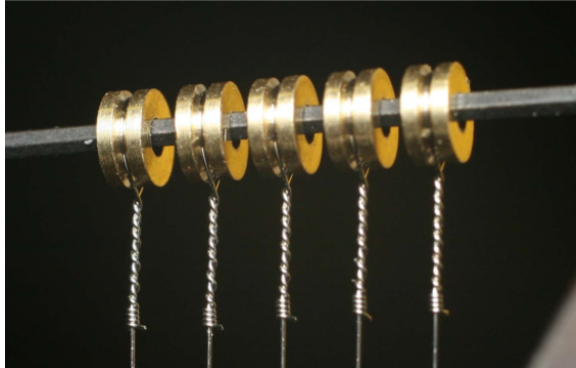


Figure 19: Picture of the wire termination on the brass ferrules. Each ferrule is 3 mm in diameter, and 1.5 mm thick.

¹ is depicted in figure 21. A comprehensive description of the MicroBooNE wire preparation and
² associated quality assurance studies can be found in [61].

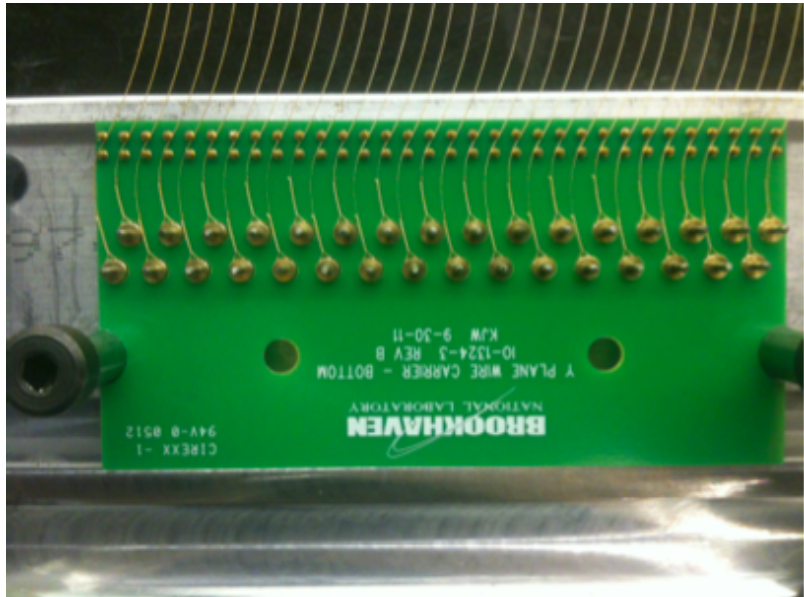


Figure 20: Picture of a collection plane wire carrier board that has been filled with wires, but has not yet had cover plate installed.

³ 4.3.3 Wire installation and tension measurements

⁴ During detector construction the completed wire carrier assemblies were manually installed onto
⁵ the adjustable tensioning bars residing in the C-channel of the supporting anode frame. A team
⁶ of two people installed each assembly (consisting of wires and supporting carrier boards on either
⁷ end) onto the anode frame. The collection plane was the first installed, followed by the middle
⁸ induction plane, and then finally the inner induction plane. Once all three anode planes were
⁹ completely installed, the tensioning bars were adjusted and a survey was taken of the tension of
¹⁰ all anode wires. Tension was measured via measuring the resonant frequency of a laser beam



Figure 21: Picture of a collection plane wire carrier board on the tension stand.

reflected off of a plucked wire and incident on a photodiode connected to a spectrum analyzer program [62]. The tension measuring equipment was developed and produced by the University of Wisconsin Physical Sciences Laboratory. The tensioning bars were adjusted iteratively until the surveyed tension of all wires was within a range, approximately ± 1.0 N of the nominal value of 6.9 N, where no single wire was too taught or loose to create detector performance issues. Figure 22 shows the final surveyed tension of the wires within the LArTPC.

4.4 Parts Preparation

The majority of the parts that make up the LArTPC are either stainless steel or G-10. These two material types, as well as any others used in the LArTPC, were tested in the Fermilab Materials Test Stand (MTS) [36], whose purpose was to investigate the suitability of materials for use in LArTPCs. The MTS confirmed that none of the materials used in the LArTPC assembly would

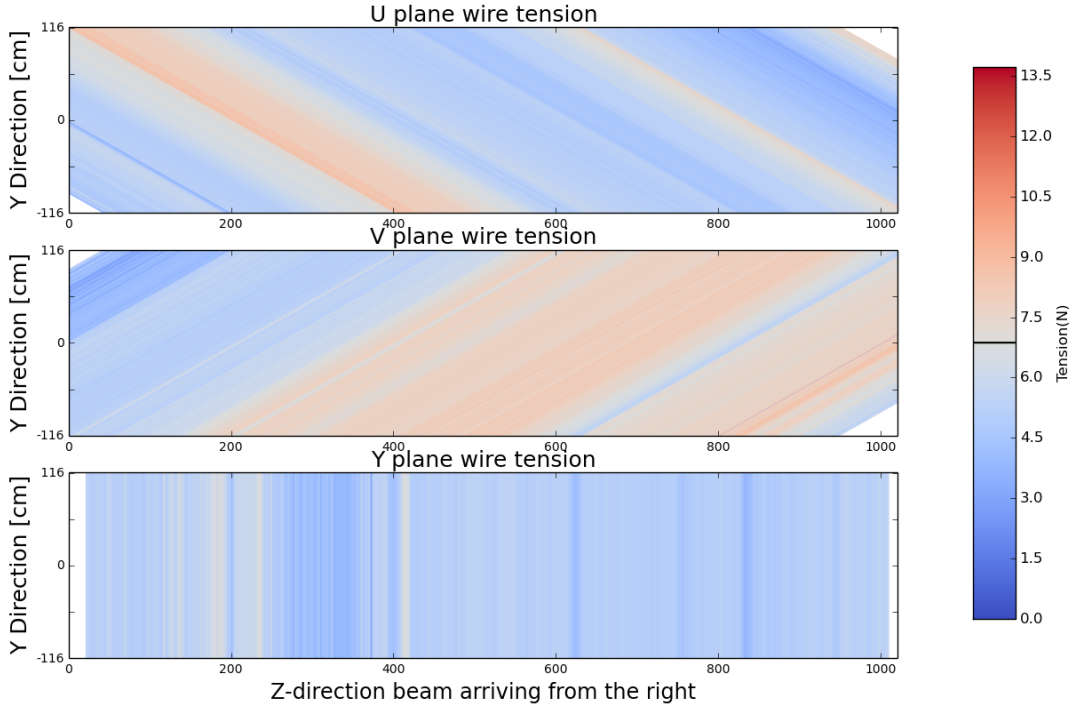


Figure 22: Final survey results for wire tension of the MicroBooNE LArTPC.

1 contaminate the liquid argon. Before assembly, all LArTPC parts were cleaned according to the
2 procedures described in the following sections.

3 **4.4.1 Cleaning stainless steel**

4 The delivered stainless steel parts were often greasy due to machining, and those with holes or
5 interior cavities generally had a significant amount of trapped metal shavings due to the machining
6 processes. Many of the pieces also had markings from permanent ink pens, dirt smears, rust spots,
7 and/or dried oil from machining. These pieces were scrubbed with ScotchBrite 7447 general-
8 purpose hand pads before cleaning.

9 Parts that were small enough to fit in an ultrasonic bath were prepared according to the follow-
10 ing prescription. A pre-rinse with tap water was performed to remove particulate matter, followed
11 by deburring of sharp edges. The first ultrasonic wash was 15 minutes in heated distilled water
12 with a 3% solution of Citranox acid detergent [63]. After a first rinse in distilled water, a second
13 ultrasonic wash was performed, again for 15 minutes, but using heated distilled water with a weak
14 solution of Simple Green detergent [64]. A second rinse in distilled water was performed, followed
15 by a final rinse in a fresh bath of distilled water. The parts were then wiped dry with lint-free cloths,
16 air dried completely, and wrapped in plastic film for storage.

17 Stainless steel parts which were too large to fit in the ultrasonic bath were prepared by a simpler
18 prescription out of necessity. A pre-rinse with tap water was followed by deburring to remove sharp
19 edges. Both the first and second washes were done with tap water and a weak solution of Simple
20 Green detergent, scrubbing with brushes and lint-free sponges. Two tap water rinses were done,
21 and the parts were then wiped dry with lint-free cloths. As a final additional step, each part was

1 wiped with 200-proof ethyl alcohol, and then air dried completely. These parts were also wrapped
2 in plastic film for storage.

3 **4.4.2 Cleaning G-10**

4 G-10 is known to absorb large quantities of water, which would outgas in the argon and could
5 inhibit reaching the required argon purity in the detector. For this reason all G-10 parts were cleaned
6 and then baked to remove moisture. The largest G-10 parts on the detector are beams that span the
7 distance between the cathode and anode. These were washed in 500-gallon ultrasonic baths that are
8 overseen by Fermilab Accelerator Division, typically used for cleaning large sections of accelerator
9 beam pipes. An initial pre-wash was done with tap water to remove as much particulate matter as
10 possible, since the machining process left a large amount of dust on the machined edges. Pieces
11 were then placed in the ultrasonic bath with heated deionized water and a 2% solution of Elma
12 Clean 65 (EC 65) neutral cleanser [65]. Two ultrasonic bath rinses were performed, and the pieces
13 were then sealed in plastic bags with clean dry nitrogen gas. In order to remove the absorbed water,
14 the large G-10 parts were then transported to Fermilab Technical Division where they underwent
15 an outgassing procedure to remove any remaining absorbed moisture. They were baked in a large
16 oven under vacuum until a plateau in the outgassing was reached, as reported by a monitor inside
17 the oven. Upon completion of the outgassing procedure, the parts were resealed in plastic bags for
18 storage.

19 **4.5 Assembly**

20 The full mechanical structure of the LArTPC is shown in figure 23, with the top image depicting
21 the cathode frame on the left, made semi-transparent to show the support structures on which the
22 cathode sheets are attached. The anode frame is on the right of this image, with I-beams configured
23 in a crossed pattern to maintain the shape and rigidity of the outer C-channel structure. Ribs of G-
24 10 connect the anode and cathode, electrically isolating them from each other while also providing
25 mounting holes to hold in place each of 64 field cage loops that define the active volume of the
26 LArTPC . The field cage loops are visible in the photograph in the bottom frame of figure 23.

27 Assembly was done inside of a clean tent, shown in figure 24, on a flat surface made up of
28 adjustable-height metal platforms that were installed on the assembly room floor. These platforms
29 were leveled to better than 0.5 mm before beginning assembly. The anode frame was the first part
30 of the detector to be assembled on this surface, shown in figure 25. It was temporarily placed
31 aside, and the cathode frame was assembled on the same set of platforms along with the G-10 ribs,
32 which stood vertically with the help of temporary unistrut support pieces. The combined cathode
33 and G-10 frame was then lifted and rotated to the proper orientation, with G-10 ribs extending
34 horizontally from the cathode to the anode, as shown in figure 26. Finally, the anode frame was
35 brought back over and attached to the G-10 ribs, and the stainless steel tubes that make up the field
36 cage loops were fed through the holes in the G-10 ribs to complete the mechanical structure of the
37 LArTPC .

38 **4.6 High Voltage System**

39 To create the drift electric field, an adjustable negative voltage (referred to as the “high-voltage”
40 or “HV”) is supplied to the LArTPC cathode, generated outside of the cryostat by a Glassman

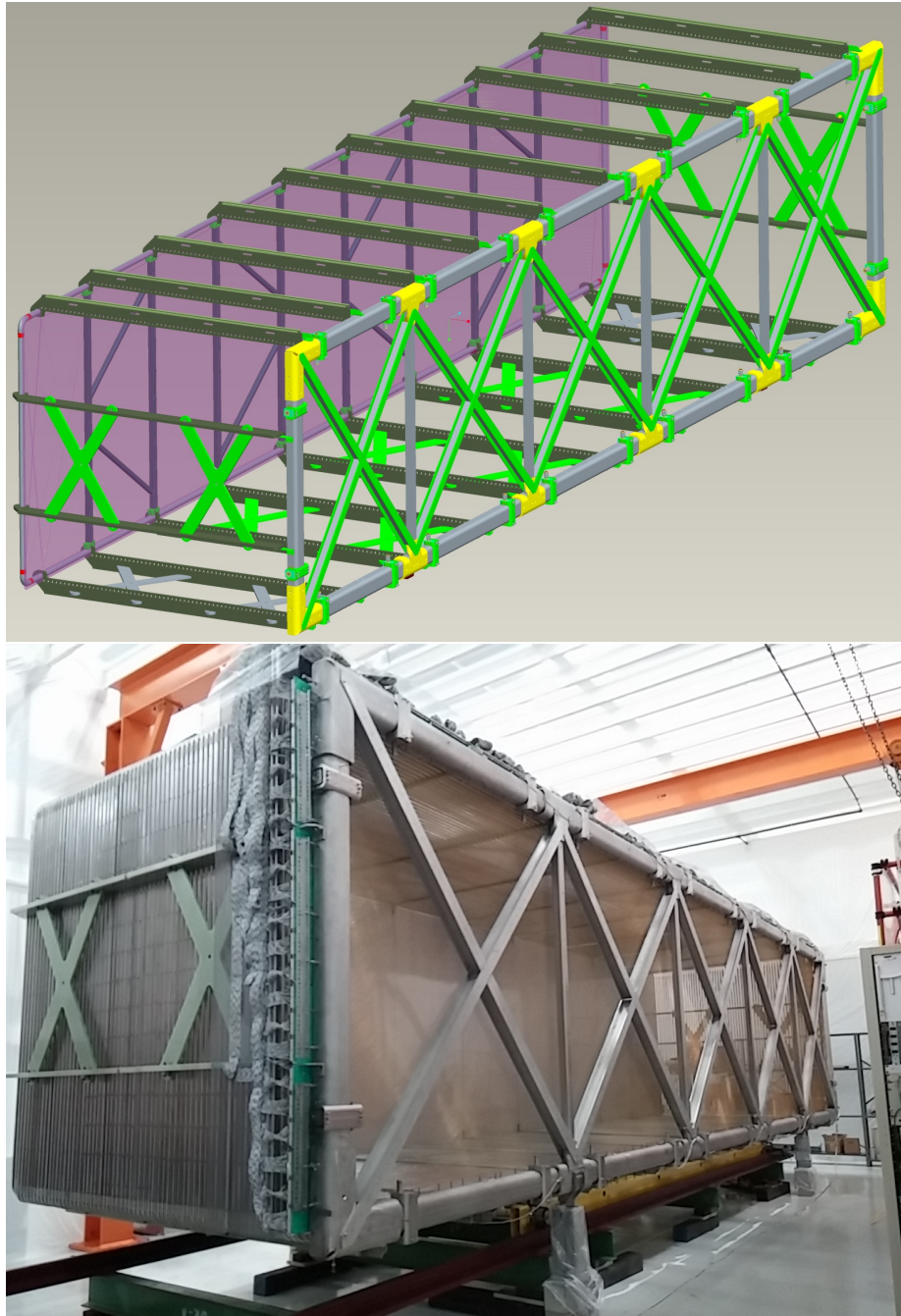


Figure 23: Top: Rendering of the full LArTPC frame assembly. Bottom: Assembled LArTPC after wire and electronics installation.

1 LX150N12 power supply. Before entering the cryostat, the output of the power supply is passed
 2 through a current-limiting resistor series that serves as both a low-pass filter for the power supply
 3 ripple, and a stored energy partition in case of a sudden reduction in voltage. The resistor series
 4 is a set of eight $10\text{ M}\Omega$ resistors submerged in a transformer oil in an aluminum container. This
 5 assembly was successfully tested to -200 kV. The capacitance of the cable is $\sim 50\text{ pF/m}$ making the



Figure 24: Clean tent where MicroBooNE LArTPC assembly was conducted.



Figure 25: Anode frame in the process of being moved from the metal assembly platforms.

¹ time constant of the component upstream of the LArTPC ~ 35 ms.

² The potential is introduced into the cryostat by a custom-designed HV feedthrough. The feedthrough is based on an ICARUS design [13]; an inner 1.0 in diameter stainless steel conductor



Figure 26: Cathode frame and G-10 ribs on metal assembly platforms.

1 carrying the HV is surrounded by an insulating tube, 2.0 in outer diameter and 1.0 in inner diameter,
2 of ultra-high molecular weight polyethylene (UHMW PE), which is further encased in an outer
3 ground tube. A photograph and drawing of the production feedthrough are shown in figure 27.

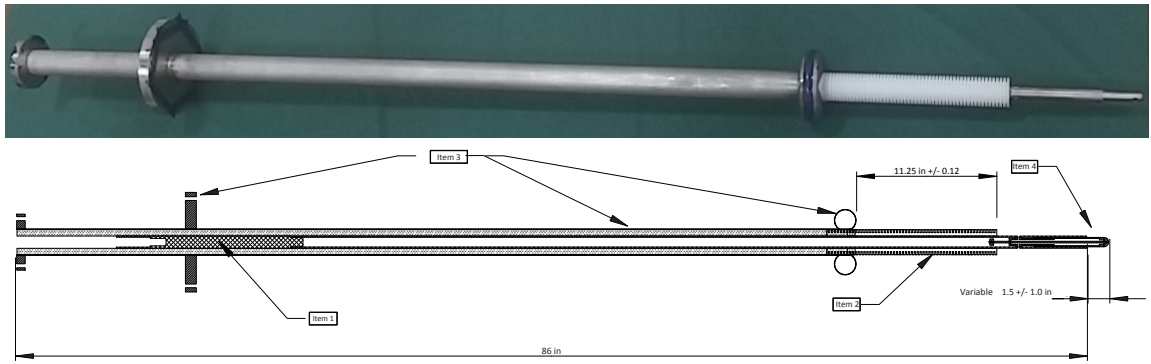


Figure 27: Photograph and drawing of the production HV feedthrough. The spherical probe tip is attached to the end of the inner conductor, on the right side of these figures.

4 MicroBooNE's voltage target combined with its geometry of a cylindrical cryostat with a
5 single drift region necessitate that the HV feedthrough extend deeper into the cryostat than the
6 ICARUS feedthrough to avoid high field regions. Figure 28 shows the HV feedthrough extending
7 into its receptacle cup attached to the LArTPC cathode. The lower termination of the outer ground
8 tube is a torus chosen to reduce the electric field between both the feedthrough and the cathode

1 plane and along the feedthrough itself. The length of exposed UHMW PE is machined with grooves
2 in an effort to improve performance. The electrical connection to the cathode is accomplished with
3 a hemispherical spring-loaded tip attached to the inner conductor of the feedthrough. When the
4 feedthrough is installed on the cryostat, the spring-loaded tip makes contact with the receptacle
5 cup attached to the cathode.



Figure 28: The production HV feedthrough inserted into the cathode receptacle cup inside the cryostat.

6 5. Light Collection System

7 Liquid argon is a very bright scintillator, and collecting the light produced when charged particles
8 travel through the LArTPC is critical aspect of fully understanding the interactions taking place in
9 the detector. The light collection system is designed to meet MicroBooNE's physics goals for light
10 collection, which are twofold. First, for accelerator-induced events, the light collection system is
11 designed to trigger on 40 MeV kinetic energy protons produced in neutrino interactions. Second,
12 for non-beam events, the system is designed for efficient observation of 5 to 10 MeV electrons from
13 supernova neutrinos.

1 The light produced by neutrino interactions in MicroBooNE is an important input for both
2 event selection and reconstruction. One of the critical capabilities the light collection system pro-
3 vides is the ability to form a beam-event trigger when a pulse of light is observed in coincidence
4 with the beam spill. Because a vast majority of beam spills will not produce a neutrino interaction
5 in the detector, such a trigger will substantially reduce the data output rate. For non-beam physics
6 studies, the light system provides triggering and an event interaction time (t_0). For accelerator-
7 induced events, the start time of a beam spill is, in principle, sufficient. However, because of the
8 long window over which the ionization electrons of an event drift (about 1.6 ms maximum drift
9 time at 500 V/cm field), there are many accelerator-induced events in which a cosmic ray muon
10 crosses the detector during the drift time. Utilizing the position of hits in the photodetectors, one
11 can better reject cosmic ray muon tracks. The light can also be used to trigger and select spe-
12 cific types of cosmic-ray calibration events (Michel electrons, straight-through muons, etc.) and
13 non-beam events (supernova neutrinos, cosmic background events to proton decay studies, etc.).

14 The light collection system consists of primary and secondary sub-systems. The primary light
15 collection system is made up of “optical units”, each one consisting of a PMT located behind a
16 wavelength-shifting plate. In total, 32 optical units were installed, yielding 0.85% photocathode
17 coverage. The secondary system consists of four light guide paddles. These paddles are introduced
18 for R&D studies for future LArTPCs, and are placed near the primary optical units to allow a
19 comparison of their performances. A flasher system, used for calibration, consists of optical fibers
20 bringing visible light from an LED to each PMT face.

21 The light collection detectors are located in the y - z plane behind the anode planes of the
22 LArTPC, as shown in figure 29. The combined transparency of the three anode planes is 86%
23 for light at normal incidence. This transparency value assumes 100% of VUV photons impinging
24 on the wires (150 μm diameter and 3 mm pitch) are absorbed. The detectors were placed so as
25 not to be obscured by the LArTPC structural cross-bars, shown in figure 29. Locating the light
26 detectors behind the anode plane places them in a very weak electric field due to the +440 V bias of
27 the collection plane. To test for an effect from weak electric fields, the response of a PMT placed
28 between a +700 V mesh and ground, separated by 50 cm, was studied. The PMT zenith was 25 cm
29 from the HV. No effects on the signal were observed. This was expected, as the photocathode is
30 held at ground, effectively acting as a Faraday cage.

31 Throughout the design and construction of the light collection system, substantial R&D was
32 performed. The reader should refer to [52, 66 – 77] for detailed results of these studies. A useful
33 overall review is available in [78].

34 Figure 30 shows the light observed in two sequential events, consistent with a muon entering
35 the detector followed by a Michel electron from the decay. One can see that the light is relatively
36 well localized. This allows the light to be correlated with specific tracks in the detector. This
37 “flash-track matching” is used to identify and reconstruct the tracks that are in time with the beam
38 spill—an important goal of the light collection system.

39 **5.1 Light Production in Argon**

40 Light produced in liquid argon arises from two processes: scintillation and Cherenkov radiation.
41 Scintillation light is produced by the formation and eventual radiative decay of excited argon dimers
42 (or eximers) and is emitted in an isotropic distribution. Liquid argon is an excellent scintillator: it

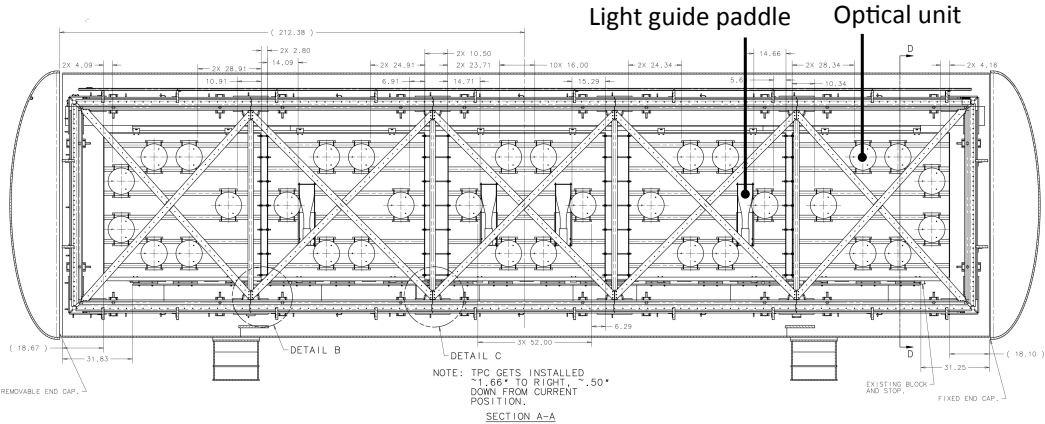


Figure 29: The MicroBooNE light collection system consists of a primary system of 32 optical units and a secondary optical system of four lightguide paddles [72]. These are mounted behind the anode wire planes such that the view is not obscured by structural cross bars of the LArTPC.

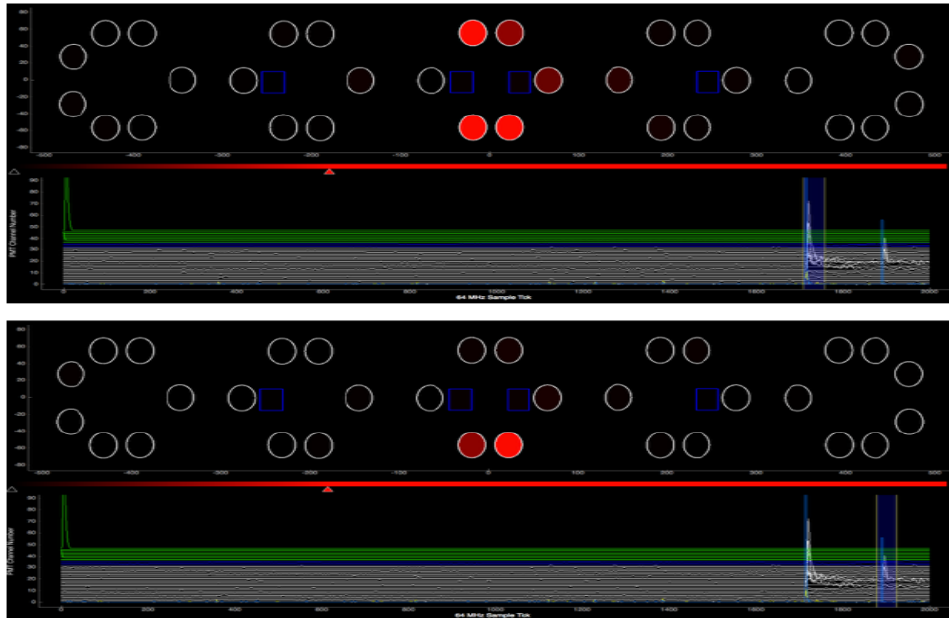


Figure 30: Two sequential event displays for the light collection system. The sequence is consistent with a muon that stops (top) and decays (bottom). The circles correspond to the optical units. Red circles indicate those units with hits. The waveforms versus time are shown below.

Table 6: Important properties of scintillation light in liquid argon that affect detection in MicroBooNE.

Property	Value	Reference
Wavelength	128 nm	[79]
Singlet, Triplet state time constants	6 ns, 1.6 μ s	[80]
Photons/MeV for $E = 500$ V/cm	24000	[13]
Triplet lifetime quench due to N ₂ at 1 ppm	20%	[81]
Attenuation length due to N ₂ at 1 ppm	66 m	[52]
Rayleigh Scattering Length	\sim 90 cm	[82]
Transparency of the wireplanes at normal incidence	86%	-

1 produces a large amount of light per unit energy deposited (about 40,000 per MeV at no drift field)
2 and is transparent to its own scintillation. The scintillation light has a prompt and slow component
3 with decay times of about 6 ns and 1.6 μ s, respectively. The two lifetimes correspond to the two
4 lowest-lying eximer states with the prompt component coming from the decay of a singlet state
5 and the slow from the decay of a triplet state. The prompt to slow ratio is about 1:3 for minimum
6 ionizing particles and varies with ionization density and particle type. Both components consist of
7 photons with a wavelength of 128 nm.

8 There is a significant uncertainty on the expected triplet lifetime [80] and this may be further
9 modified by quenching (non-radiative dissociation of excimers by impurities) [81]. Other factors
10 that can affect the arrival of the light include Rayleigh scattering, absorption by impurities, and
11 obstructions. For detailed discussion of the physics of scintillation light production and propagation
12 in MicroBooNE, see [78]. Table 6 summarizes information about the scintillation light.

13 Because scintillation photons have a wavelength of 128 nm they are very difficult to detect
14 using conventional photodetectors. Figure 31 summarizes the challenges involved in detection of
15 the 128 nm scintillation light. In order to detect the scintillation light, with spectrum shown in
16 red, the VUV photons must be shifted into the visible region. MicroBooNE employs tetraphenyl-
17 butadiene (TPB). This organic fluor absorbs in the UV (green line) and emits in the visible with a
18 peak at 425 ± 20 nm (green hatched region), the peak wavelength having a slight dependence on the
19 micro-environment of the fluors. This is a favorable wavelength for detection by the photomulti-
20 plier tubes (PMTs) employed by MicroBooNE. The efficiency for transmission through borosilicate
21 PMT glass (black) and the quantum efficiency of the cryogenic tubes used in MicroBooNE (blue)
22 are overlaid on the TPB spectrum.

23 5.2 The Primary Light Collection System

24 Each of the 32 optical units of the primary light collection system consist of a cryogenic Hamam-
25 matsu 5912-02MOD PMT seated behind an acrylic plate coated with a TPB-rich layer and sur-
26 rounded by a mu-metal shield. Figure 32 shows a diagram of one unit (left) and a photograph
27 of installed units (right). Past experiments have directly coated PMTs with wavelength shifter
28 [13]. However, the MicroBooNE design separates the PMT from the wavelength-shifting plate for
29 simplicity of quality control and installation. This proved important, as R&D indicated that TPB is



Figure 31: Scintillation light emission spectrum (red) and TPB re-emission spectrum (green), in arbitrary units. Superimposed are important efficiencies (see y axis): Dark green line – absorption of VUV light by TPB; Black line – transmission of borosilicate glass; Blue line – efficiency of a R5912-02mod cryogenic PMT [78]

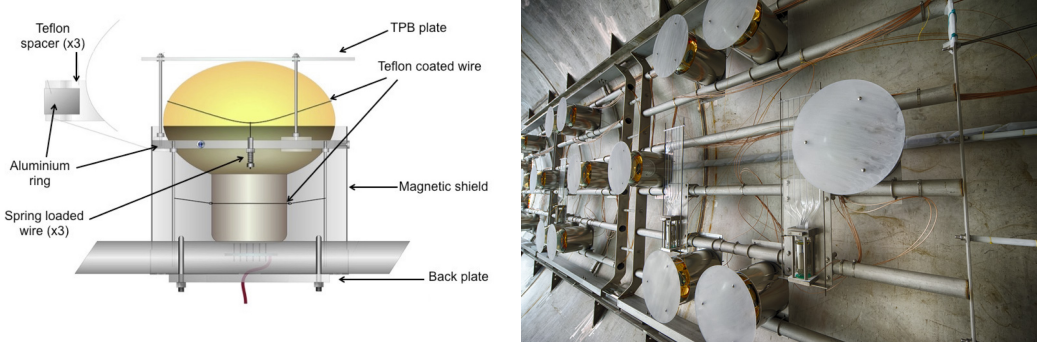


Figure 32: Left: diagram of the optical unit; Right: units mounted in MicroBooNE, immediately prior to LArTPC installation.

¹ particularly vulnerable to environmental degradation (see section 5.2.3). In this section, description
² is provided for each component of the optical unit, as well as for the overall assembly.

³ 5.2.1 Photomultiplier Tubes and Bases

⁴ Reference [70] provides detailed information on the selection and testing of the 8" Hamamatsu
⁵ R5912-02mod cryogenic PMTs employed in MicroBooNE. In this section a brief summary of the
⁶ findings from this testing is presented.

⁷ The R5912-02mod employs a bi-alkali photocathode. Because the PMT is designed for cryo-
⁸ genic use, the R5912-02mod also features a thin platinum layer between the photocathode and the

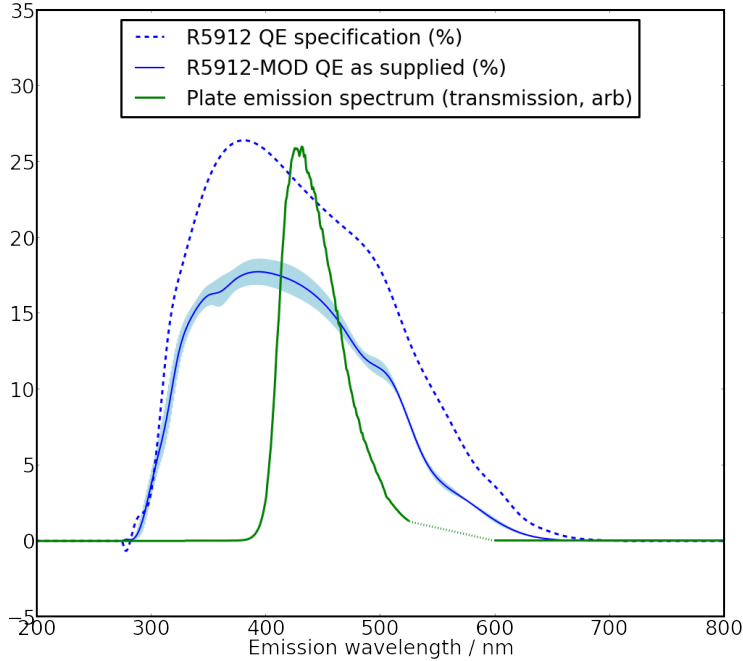


Figure 33: The specification for the non-platinum undercoated PMT from [83]. The blue band shows the mean and standard deviation of the four quantum efficiency curves provided by Hamamatsu for installed MicroBooNE PMTs. Also shown is the measured emission spectra of MicroBooNE wavelength-shifting coatings, discussed in section 5.2.2. [78]

1 borosilicate glass envelope to preserve the conductance at low temperatures. While this allows
 2 the PMT to function below 150 K, absorption in the platinum reduces the efficiency of the PMT
 3 by 20%. Figure 33 provides quantum efficiency curves for the 8 inch photomultiplier tubes. The
 4 manufacturer's specifications do not include the effects of the platinum photocathode coating, but
 5 a wavelength dependent quantum efficiency was provided by Hamamatsu for 4 of the 32 installed
 6 PMTs. The mean and standard deviation of these curves is shown in figure 33.

7 The R5912-02mod is a 14-stage PMT. The high gain at room temperature (10^9 at ~ 1700 V),
 8 compensates for known reduced gain at 87 K in the liquid argon. The high gain also has the
 9 additional advantage of allowing operation at lower than nominal voltage which reduces heat-loss
 10 in the cables and the potential for high voltage breakdown at the feedthroughs.

11 The PMT base is designed such that the photocathode is grounded and the last dynode in the
 12 chain is held at large, positive voltage. Thus the PMT bulb, which is closest to the LArTPC anode
 13 plane, is at ground and does not disturb the electric field on the wires. The result is that the high
 14 voltage (HV) can be provided and the signal can be extracted from the PMT using a single cable,
 15 reducing the cable volume in the vapor region and removing a possible source of out-gassing water
 16 impurity.

17 The flat PC-board base was made of Rogers RO4000-series woven glass-reinforced laminate,
 18 which is the same material with the LArTPC cryogenic front end boards. The base is attached
 19 ~ 1 cm from the bottom of the PMT and is the closest possible distance of safe approach to the
 20 PMT vacuum seal tip. A schematic and photos of the PMT base are provided in reference [70].

1 The passive components include only metal film resistors and C0G/NP0 capacitors, which have
2 the minimum temperature coefficients, and the performance at cryogenic temperatures were tested.
3 Because the supplied HV and return signal share a single cable, the signal must be split from the
4 HV through an AC-coupling capacitor, as is discussed in section 5.2.5.

5 All installed PMTs were tested in a PMT test stand, both at room temperature and in liquid
6 nitrogen which is at 77 K. The details are described in reference [70]. In brief, the test stand
7 consisted of a light-tight 346 L, liquid nitrogen filled dewar into which up to four PMTs could be
8 installed. The PMTs were immersed and maintained in the dark environment for up to three days
9 before most measurements of the dark rate and gain were performed. A fiber brought in light from
10 a pulsed blue LED, which was tested for linearity with bias voltage.

11 Among the important results from cryogenic testing were the following [70]:

- 12 • The PMTs could be ramped to voltage quickly in the cold environment, and after 30 minutes,
13 the gains were found to be stable.
- 14 • If the room temperature PMTs were immersed in liquid nitrogen, dramatic changes in the
15 gain were observed after initial turn-on. The PMT gain remained high in the first \sim 5 hours
16 after immersion, and then suddenly dropped by more than a factor of two, afterwards reaching
17 a stable value with a small drift.
- 18 • The PMT response showed good linearity up to 100 photoelectrons (PE), which was the
19 maximum attainable by the PMT test stand LED.
- 20 • The HV for each PMT was selected to produce a gain of 3×10^7 in liquid nitrogen, and was
21 typically chosen to be \sim 1300 V.
- 22 • The dark current plateaus extended up to 1800 V in liquid nitrogen, and the dark current is
23 higher in liquid nitrogen than at room temperature.
- 24 • The PMT performance depended on rate of the pulsed LED.

25 No PMTs were rejected on the basis of the testing. However, there were three unexpected results
26 to note here.

27 The first unexpected behavior was that, at room temperature, most of the PMTs showed gains
28 that were 10 to 30% higher than manufacturer's specifications. As expected at cryogenic tempera-
29 tures, the gain is reduced by \sim 10% to 50%. To measure the PMT gain, the LED was set to produce
30 one to two PEs. The gain was found from the separation of the single PE peak from the pedestal,
31 where the single PE response was fit using the procedure described in [84].

32 Second, it was found that the PMTs are noisier in the cryogenic environment. It would typ-
33 ically be expected that thermal emission is suppressed at cryogenic temperatures and one would
34 expect a lower dark current for PMTs operating in this regime. However, the dark current mea-
35 sured in the liquid nitrogen is higher than at room temperature. Although the cause is unknown,
36 this phenomenon has previously been observed[85]. A proposed explanation is provided in [86].

37 Third, an LED pulse-rate-dependent gain shift was found during testing, as shown on figure 9
38 of reference [70]. This behavior is described qualitatively in [87]. With 10 kHz LED pulsing, the
39 gains of cold and dark-adapted PMTs were shown to steadily increase, requiring nearly 24 hours

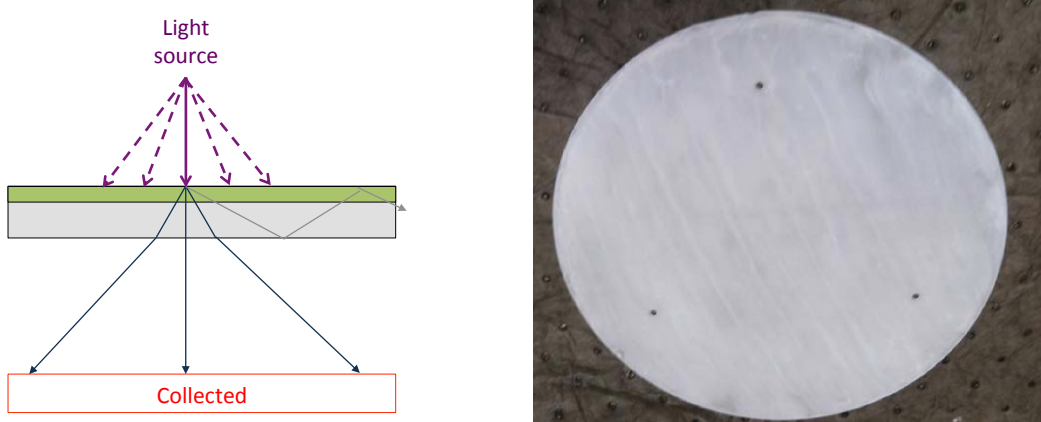


Figure 34: Left : Illustration of transmission mode, used by the optical units. Right: photograph of a coated plate.

from turn-on to stabilize. The effect was not observable at 10 Hz. This is relevant to MicroBooNE because the cosmic muon rate in the MicroBooNE detector is ~ 5 kHz. Therefore a similar effect is expected in the MicroBooNE detector. Preliminary results from measurements of the PMTs installed in the LAr-filled MicroBooNE cryostat shows the expected effect.

5.2.2 Wavelength-Shifting Plates

In order to be sensitive to 128 nm VUV liquid argon scintillation photons, the optical assemblies use a wavelength-shifting coating to convert this VUV light to visible wavelengths that are detectable by photomultiplier tubes. In MicroBooNE, the active ingredient of this coating is TPB, an organic fluor which absorbs efficiently in the vacuum ultraviolet with an emission spectrum peaked around 425 nm [88] as shown in figure 31.

The optical unit PMTs observe light transmitted through TPB-coated, 12-inch diameter acrylic plates (see figure 34). The coating consists of a 1:1 TPB-to-polystyrene ratio, with 1 g of each dissolved in 50 ml of toluene. A small amount of ethyl alcohol is added as a surfactant. The coating is applied to the acrylic plate in three layers by brush-coating. The solution dries in air at room temperature. This leads to a final layer which is oversaturated with TPB, and white crystals form on the surface as the coating dries. The presence of surface crystallization gives the MicroBooNE plates a white, opaque finish. Details of the process are described in reference [89].

The emission spectrum in figure 33 was measured using a Hitachi F-4500 fluorescence spectrophotometer with an incident beam of wavelength 270 nm, selected by a diffraction grating from a xenon lamp. A standard rhodamine dye calibration sample was used to correct for drift in the lamp and spectrometer. The measurement was made in transmission mode, and an artifact peak at a harmonic of the twice incident wavelength was observed between 525 and 600 nm. This region is omitted from the reported spectrum of figure 33.

As shown in figure 33, although the absolute quantum efficiency for the platinum-undercoated cryogenic PMT is lower than the non-cryogenic version, the wavelength dependence is similar, and overlap between the TPB emission spectrum and the sensitive wavelength range of the PMT remains high. Using the measured TPB emission spectrum for plate coatings and the PMT quantum

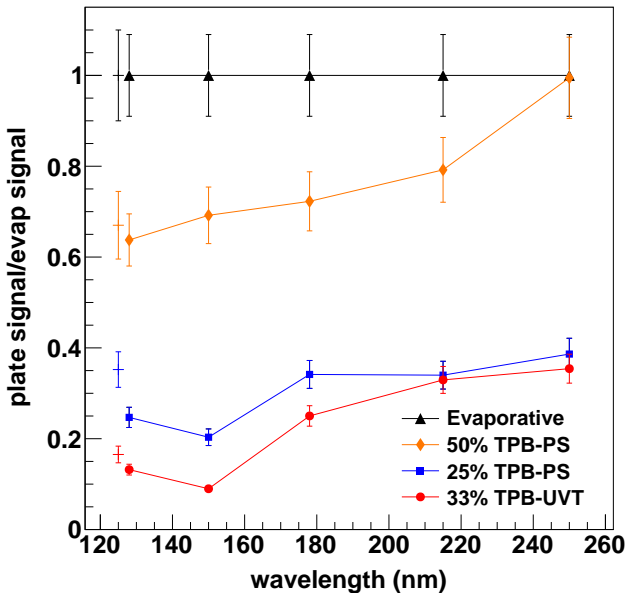


Figure 35: Measured efficiencies of various wavelength-shifting coatings, from [89]. In this plot, 50%TPB-PS is the MicroBooNE plate coating used in the optical units. The 33%TPB-UVT is the light guide coating for the secondary light collection system described below. Connected points were measured in a vacuum monochromator at room temperature, and non-connected points were measured in liquid argon with 128 nm scintillation light. All points are normalized to the performance of an evaporatively coated plate.

¹ efficiency curve provided, the spectrum-averaged PMT quantum efficiency is $15.3 \pm 0.8\%$ per
² visible photon incident on the photocathode.

³ The wavelength-shifting performance of the coating was measured at 128 nm relative to evap-
⁴ orative coatings of the type studied in [90]. Coating efficiencies were measured as a function
⁵ of wavelength between 128 and 250 nm using a vacuum monochromator at room temperature.
⁶ They were also measured in liquid argon using 128 nm scintillation light, relative to the same
⁷ evaporatively coated plate. These data are shown in figure 35, and more information about these
⁸ measurements can be found in [89].

⁹ The absolute efficiency of the MicroBooNE coatings can be obtained by multiplying the rela-
¹⁰ tive efficiencies of figure 35 by the measured absolute efficiencies from [90], and accounting for the
¹¹ temperature dependence in the wavelength-shifting efficiency of pure TPB reported in [91]. The
¹² expected efficiency of MicroBooNE coatings is found to be 0.98 ± 0.17 emitted visible photons per
¹³ incident 128 nm photon for the plate coating.

¹⁴ 5.2.3 UV Light Protection for the Wavelength-Shifting Plates

¹⁵ TPB coatings have been shown to degrade under exposure to ultraviolet light [68] through a rad-
¹⁶ ical mediated photo-oxidation to the UV-blocker and photo-initiator benzophenone [92]. Several
¹⁷ measures were taken to ensure that degradation was minimized during the construction of the ex-

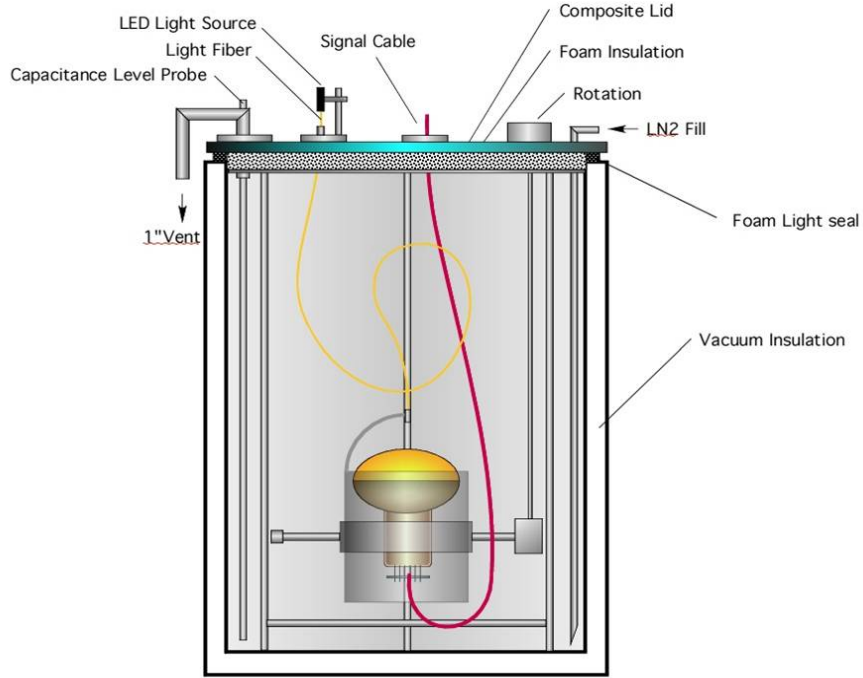


Figure 36: Schematic of the system used to study the mu-metal shields. The design allows rotation along all three axes.

periment. The TPB powder and coated elements were stored in the dark at all times, with coated plates and light guides being kept wrapped in foil and stored in a dark container before installation. The detector construction area was covered with a UV blocking plastic [93], and test plates were placed at various positions in the clean tent to check for degradation from stray light. After several weeks of exposure, one test plate with a clear line of sight to the tent entrance demonstrated a few percent degradation, and all others showed no observable loss of efficiency. The open end of the MicroBooNE cryostat was shielded from light by a black curtain after installation, and the feedthroughs of the cryostat were blocked when not in use to prevent stray light from entering. The coated plates were the final component of the optical system to be installed into the detector to give the minimum possible light exposure during the detector construction process.

5.2.4 Cryogenic Mu Metal Shields

The trajectories of electrons within the 8" PMT can be deflected by the Earth's magnetic field. This effect can be reduced or removed by surrounding the PMT with mu metal, a metal of low magnetic permeability. Commonly used mu-metal fails to provide shielding at cryogenic temperatures. Two types of cryogenic mu metal, Cryoperm 10 and A4K, both products of Amuneal, were identified that did provide shielding at cryogenic temperature.

The mu metal shields were tested in the apparatus shown in figure 36. The system allowed for the PMT to be positioned at an angle relative to the vertical axis, with the rotator set to 30 positions from 0 to 348° . The set-up was on a dolly that allowed for rotation about the vertical axis. PMT tests were performed in air and in liquid nitrogen. PMTs were dark adapted for 5 hours before

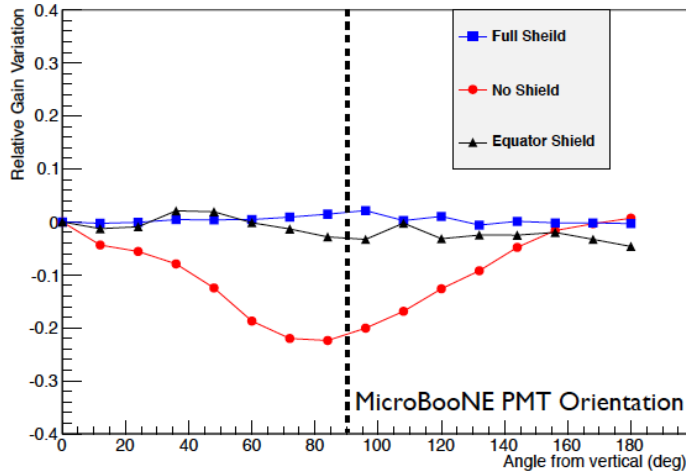


Figure 37: Red: Angular dependence of a PMT response with no shield; Black: for a shield that reaches the tube equator; Blue: for a shield that fully covers the tube to the zenith.

1 testing. A blue LED provided 1 to 2 single PEs of light through an optical fiber. The fiber was
 2 fixed to the PMT mount such that the endpoint was stationary with respect to the tube as the system
 3 was rotated.

4 The mean charge from the PMT as a function of angle was recorded. The error was primarily
 5 systematic. The $\sim 10^6$ LED pulses per data point give $< 1\%$ statistical error on the mean.
 6 However, 24-hour studies of a single point showed $\sim 5\%$ variations in collected charge due to
 7 gain drift. Results showed that A4K and Cryoperm function essentially identically, to within the
 8 measurement error, and so MicroBooNE chose A4K, based on significant cost savings. A plot of
 9 the relative PMT gain variation versus angle from vertical, figure 37, shows that adding the shield
 10 significantly improves PMT performance. This plot shows the effect of the A4K shield with the
 11 height aligned with the equator of the PMT (black) and aligned with the zenith of the bulb (blue),
 12 compared to no shield (red) as a function of PMT azimuthal angle. Given the 5% systematic error,
 13 the two shield positions are indistinguishable.

14 As a result of these tests, the A4K shields were designed to extend just past the equator of the
 15 PMT. The shield has small holes in the backplate that allows the PMT cables to exit the shield.
 16 MicroBooNE is the first LArTPC to use cryogenic mu metal shields in its light collection system.

17 5.2.5 Implementation of the Primary System

18 The light collection system is composed of optical units assembled as shown in the top picture
 19 of figure 38. The PMT is seated within the mu metal shield on three teflon pads attached to an
 20 equatorial support ring. The neck of the tube slides inside a loose wire guide-loop that prevents
 21 the PMT from tipping. The PMT is held within this assembly using teflon-encased wires that
 22 extend across the bulb and connect to wire hooks attached to the equatorial ring with stainless
 23 steel springs. Legs extending from the support at the equator are screwed into a backplate for final
 24 mounting. Concern about differences in contraction of the materials led to this design which holds
 25 the PMT in place, but with only moderate rigidity. The units were tested to ensure the PMTs would
 26 not be displaced during installation and filling. Three posts extend upward from the equatorial

1 ring to hold the plate 3.0 cm above the apex of the bulb. The optical units slide into a cylindrical
2 mu-metal shield, which screws into the equatorial ring. The unit is then mounted on stainless steel
3 back-plates affixed to a support rack, as shown in the bottom picture of figure 38.

4 The support rack consists of five stainless steel components, or modules, for ease of instal-
5 lation. Each module has vertical height 1.83 m and horizontal length 2.07 m, resulting in a total
6 horizontal length of 10.36 m. Unlubricated Thomson bearings fitted to the lower edge allow each
7 module to slide into the cryostat on rails mounted in the vessel. The system was designed to allow
8 the light detection system to slide into the vessel after the LArTPC was installed. However, in the
9 end, scheduling permitted installation of the system before the LArTPC installation. This had the
10 advantage of making installation and surveying easier, but the drawback that the system would be
11 exposed to UV light for a long period. Therefore, the units were installed with dummy clear acrylic
12 plates, and the TPB coated plates were installed only just before the LArTPC was moved in and
13 the detector could be easily protected from light. During optical unit installation, each rack module
14 was supported by a temporary mounting rail. The optical units were then mounted in positions
15 chosen to avoid obstruction by the LArTPC cross-bars, as shown in figure 29. As the units were
16 mounted and slid into the cryostat, the cables were loosely tied to the bars of the rack for support
17 and constraint.

18 The “splitter” circuit, located outside of the cryostat, is shown in figure 39. The splitter sepa-
19 rates the HV of the PMT from its output signal which is subsequently split into a high-gain (HG)
20 and a low-gain (LG) channel. The HG and LG channels respectively carry 18% and 1.8% of the
21 output signal. This allows a wide dynamic range for ADC readout of the PMT pulses. The ca-
22 pacitance was chosen to minimize reflections, since the bases are not back-terminated. The HV is
23 supplied to the splitter using BiRa Corporation, Model 4877PS modules.

24 The PMT cable system delivers HV and returns signals between the external splitter and the
25 optical unit in the cryostat. A single cable runs from an external connector, through the feedthrough
26 filled with Stycast 2850 epoxy [94], into the cryostat and to the PMT base. The RG316/U coaxial
27 cable has 50 Ohm impedance. Cables were terminated with Pasternack PE4498 SHV to accom-
28 modate that the cable carries HV to the tube as well as signals from the tube. The cable carries
29 an AC voltage rating of 1100 V; however tests showed the DC rating to be at least three times
30 higher and so suitable for this use. The cables were routed through feedthroughs consisting of a
31 pipe filled with solidified epoxy mounted on a conflat disk. On the warm side of the feedthrough,
32 the cables were terminated at a patch panel with SHV connectors. The SHV connector impedance
33 has a negligible effect on the 20-30 ns PMT signals. SHV cables connect the patch panels to the
34 splitters. The impedance of every channel was tested at the feedthrough patch panel for a stable
35 and correct value for the base resistance, which was 4.04 ± 0.02 MΩ for the 8-inch PMTs.

36 **5.3 PMT Testing and Quality Assurance**

37 The PMTs were tested and characterized before installation in the detector in the "Bo" cryostat at
38 Fermilab. The Bo cryostat is a 250-liter vacuum-insulated vessel with an inner diameter 22 inches
39 and a depth of 40 inches used for R&D studies, and, relevant to this paper, a vertical slice test of
40 the MicroBooNE optical units. The system is described in detail in reference [78]. The cryostat
41 can be filled with purified LAr with parts per billion level contamination of oxygen and water and
42 parts per million level of nitrogen. The light collection system was tested with light from visible

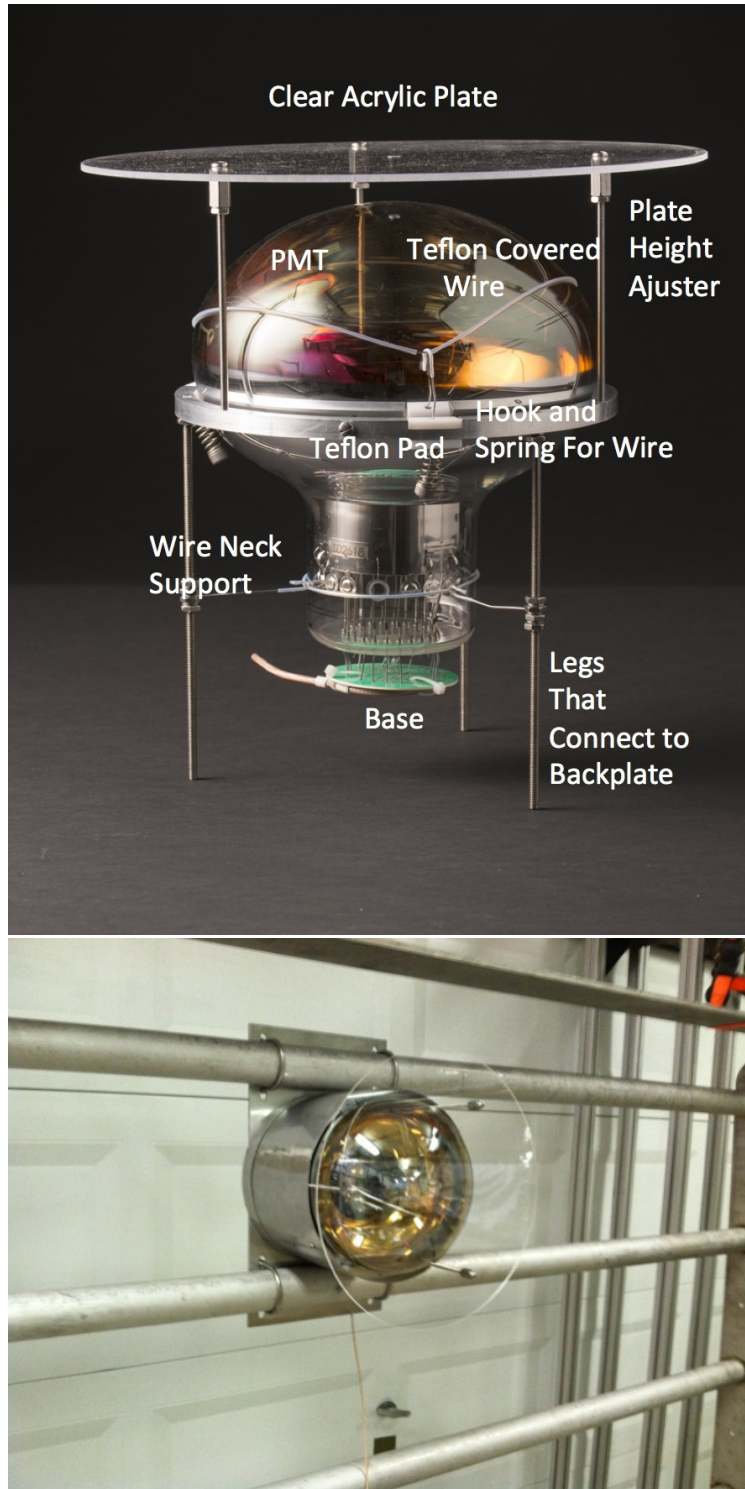


Figure 38: Top The optical unit mount internal to the shield, with components labeled; Bottom: Unit mounted on rails. The clear plates were replaced with TPB-coated plates immediately before LArTPC installation, as discussed in the text [70, 72].

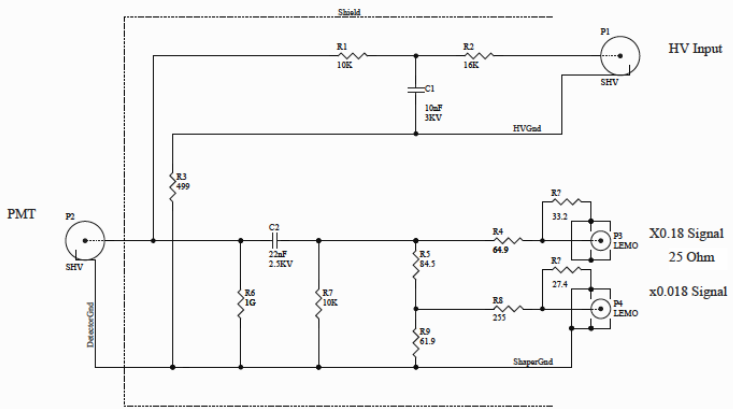


Figure 39: The "splitter" circuit. The circuit connects the HV source to the PMT. It also provides a pathway for signal pulses from the PMT to reach the readout electronics via an AC-coupling capacitor (C2). The signal is split into two copies, one provided with an attenuation factor of 0.18 and another at 0.018. Both signal sources are recorded by the readout electronics in order to provide two dynamic ranges.

(420 nm) and UV (250 nm) LEDs piped in via fiber, as well as scintillation light from ^{210}Po alpha sources and cosmic rays.

A vertical slice test (VST) of the MicroBooNE optical system was performed in the Bo Cryo stat. The slice consisted of two 8 inch PMTs with base electronics, mu-metal shield, TPB plates, cable feed throughs, splitters, the HV power supply and the interlock system. Tests were performed without and with the mu-metal shield. The test made use of the DAQ components described in section 6, including the shaper, FEM, trigger card, control card, and server. The MicroBooNE trace impurity monitors were also used.

The VST informed the final design of many components, as well as producing results relevant to understanding the running conditions and performance expectations. For example, during studies of the response of the slice to 128 nm scintillation light from the alpha source, valuable information was gathered on the single photo-electron dark rate and cosmic ray rate that could be scaled to the MicroBooNE detector expectations. As a second example, these runs allowed characterization of the pulse shape nonlinearities of the optical units, as seen in figure 40. These were shown to be significant at ~ 300 photo-electron in pulse amplitude. Full amplitude saturation occurred at ~ 670 PE. Thus, it is concluded that for pulses of more than 300 PE, pulse shape cannot be described by linear superposition of single photoelectron pulses.

5.4 Secondary System: Acrylic Light Guides for R&D

A secondary light collection system consisting of four lightguide paddles was also installed. This concept has several advantages for future large detectors such as DUNE. First, the collection area per channel is larger than the optical units, providing more coverage for the same number of electronics channels, cables, and feedthroughs. Second, the detectors have a flat profile so they can be slid between chambers in a multi-LArTPC detector, minimizing space requirements of the light

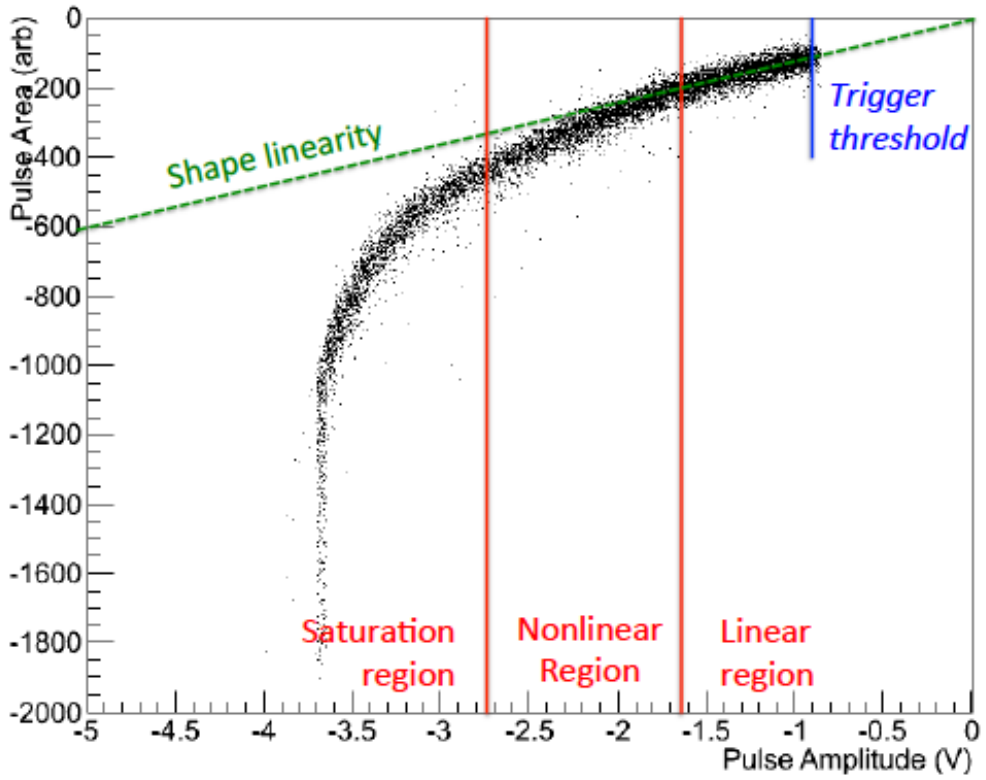


Figure 40: As shown by the VST, linearity of cosmic-ray induced PMT pulses is maintained up to amplitudes of around 1.7 V (300 PE), and amplitude saturation occurs at 3.7 V (670 PE) [78]

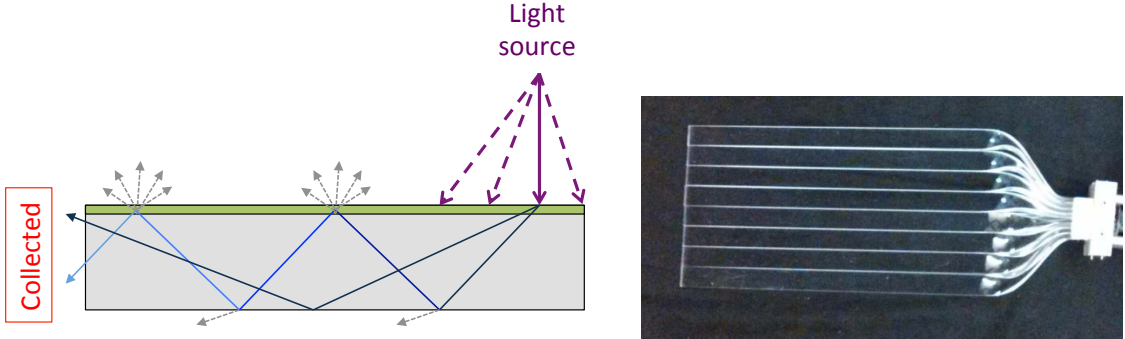


Figure 41: Left : Illustration of guiding mode, used by the paddles. Right: photograph of a coated paddle.

¹ collection system. In the case of MicroBooNE, the design gradually guides light in bent acrylic bars to a PMT. This design was an early alternative to a perfectly flat design that guides the lights to SiPMs. Running this system will provide long-term information on performance of lightguide

1 based systems. It also enhances the MicroBooNE dynamic range, since the lightguide detectors
2 saturate at a much higher light level than the optical units.

3 In the case of the lightguides, the 128 nm light is absorbed and shifted by a clear wavelength-
4 shifting coating, and the re-emitted light is guided to a 2-inch Hamamatsu R7725-MOD PMT, as
5 illustrated in figure 41, left. The installed paddles consist of six bars. A photograph of one coated
6 paddle with eight bars is shown in figure 41, right. The active length of each bar is 20 inches. This
7 system was added for R&D purposes and made use of 8 spare channels available of HV, cables,
8 feedthroughs, and electronics. The impedance of the 2 inch PMTs, tested at the feedthrough, was
9 $4.89 \pm 0.01 \text{ M}\Omega$. As shown in figure 29, each paddle is installed next to an optical unit for direct
10 comparison of performance.

11 The coating requirements for plate assemblies and light guides are different, and so the com-
12 position and coating methods for each were separately optimized. In the case of the light guide
13 coatings, the figure of merit is the light emitted in guided mode. Guided mode light is the light
14 that is detected at one of the ends of a test sample, which is orthogonal to the illuminated face of
15 the sample. In addition to the wavelength-shifting efficiency of the active layer, the detected light
16 yield is affected by the reabsorptive and scattering losses in the coating as visible light propagates
17 along the bar. The light guide assemblies have a TPB coating of 33% TPB to 67% UVT acrylic
18 by mass, also with ethanol surfactant. The coating is applied as a single layer and the TPB re-
19 mains suspended in the acrylic matrix as the coating dries, leading to a smooth, visibly transparent
20 surface. The performance and attenuation behavior of similar light guides to those installed in Mi-
21 croBooNE were studied experimentally in [69]. The reported non-exponential attenuation suggests
22 that surface losses dominate over bulk losses as the attenuation mechanism, and that the fractional
23 loss per reflection within the light guide is of order 2-3% [92].

24 In the light guide coatings, the TPB is suspended in an acrylic matrix which leads to a slight
25 broadening of the emission spectrum compared to the spectrum from the plates. This is an ex-
26 pected effect—TPB fluorescence has been shown to have dependence upon its microenvironment
27 [95, 96, 91, 97, 98], and reference [91] demonstrated spectral broadening in the presence of a
28 polystyrene substrate. Using the monochromator described for the plate spectrum studies, the light
29 guide coating spectrum was measured in guided mode. A 10 cm section of light guide, with the
30 incident beam perpendicular to the TPB coated surface, was used. Based on reference [91] it is ex-
31 pected that the emission spectrum for the light guide coating, with TPB embedded in the substrate,
32 will not change significantly as it cools to 87 K. The expected efficiency for the light guide coating
33 is found to be 0.25 ± 0.05 emitted visible photons per incident 128 nm photon.

34 **5.5 Calibration**

35 The flasher system for the optical units and the light guides is described in reference [75]. This
36 system was developed to check the timing of the installed optical units, exercise the optical units
37 during construction and commissioning, and to calibrate them once the detector is operational. The
38 reference provides engineering drawings and details. The system is briefly summarized here.

39 A control board pulses an array of 400 nm LEDs, each of which is coupled through an optical
40 feedthrough to 10 m optical fibers within the cryostat. The custom feedthrough/patch panel design
41 encases the fibers in Arathane CW 5620 blue with HY 5610 hardener. The internal fibers are Molex
42 FVP polyimide fibers with diameter of 600 mm, cladding of 30 μm , and an additional buffer layer

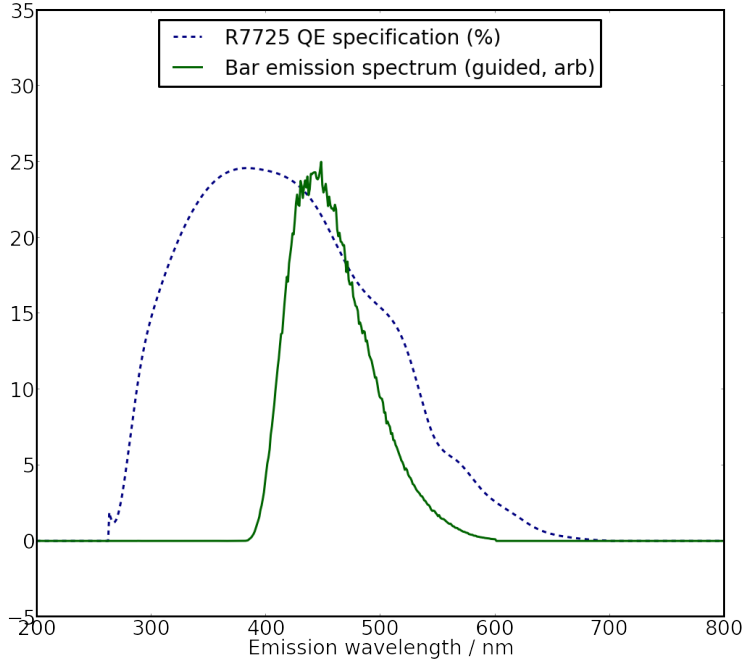


Figure 42: Measured emission spectra of the light guide coating in guided mode, and the R7725 quantum efficiency. Only the quantum efficiency of the non-undercoated PMT model is shown, from [99].

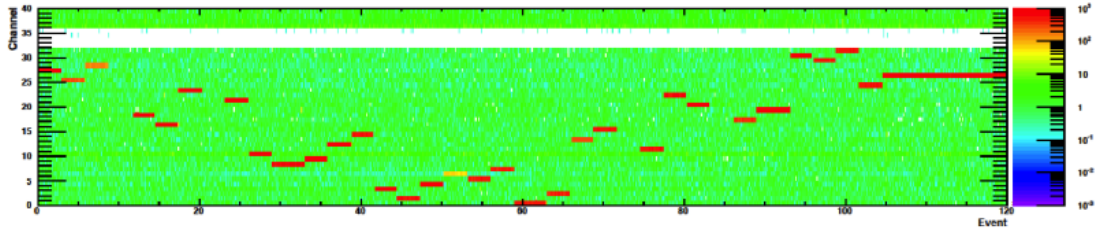


Figure 43: Charge detected in each PMT due to flasher tests, shown as a function of time. Each PMT is flashed for a short period. The white band indicates unused channels.

of 25 μm . Each PMT has an individual calibration fiber. Each fiber is routed along the rack and attached to the PMTs by a fiber holder constructed of an aluminum standoff with a nylon-tipped set screw at a distance of about 2 inches from the PMT glass.

Figure 43 shows the results of flasher tests on all 32 optical units and four PMTs on the paddles. Time is along the x axis and PMT channel number is along the y axis. The white region separating the optical unit PMTs from the paddle PMTs represents unused channels. The colored bars indicate charge detected in the PMTs during flashing. One can see that all tubes respond properly.

5.6 Coupling of PMT Signals to the Anode Wires

The ICARUS detector has observed an unexpected cross-talk between their PMTs and collection wire plane [100]. The Argontube test stand at the University of Bern also observed this effect [101].

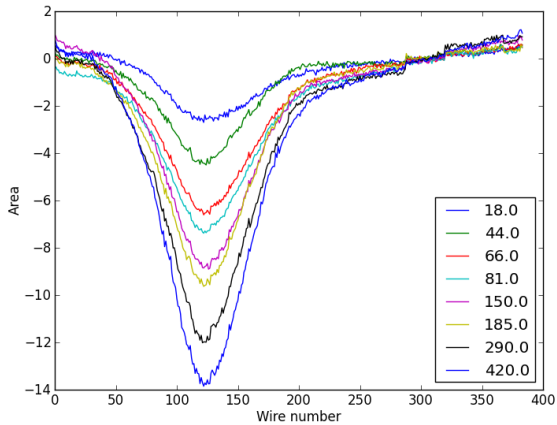


Figure 44: Area of signal pulses recorded on collection plane (in arb. units) as a function of wire number (arb. offset). The legend indicates the calibrated photo-electron count. The signal pulses are averaged over 50,000 repetitions. The plots are pinned together at wire 300, as the distribution baseline fluctuated over the course of the experiment due to intermittent noise.

Therefore, while the LArTPC was under final testing, before being rolled into the cryostat, an experiment was devised in order to determine the implication of this cross-talk for MicroBooNE. One of the production 8" Hamamatsu R5912-02mod PMTs was placed 5" from the LArTPC collection wire plane. This PMT was encased in a dark box with an optical fiber delivering light from a LED flasher. The collection wire plane was read out using a DAQ test-stand that reflects the final DAQ design.

A clear signal was observed on the collection plane when the LED fired. The magnitude of the signal was characterized as a function of photo-electron count (figure 44) and separation between the PMT and wire-plane. The signal induced on the collection plane was estimated to be no more than ~ 10 ADC counts for a cosmic ray under normal operating conditions. This was reduced to ~ 2 ADC counts when the PMT was encased in the μ -metal shields. This was deemed an acceptably small amount that further shielding was not required.

The effect appears to saturate with photo-electron count, and is reduced when shorting the resistors between the anode and last dynode. A later test with Argontube showed that the signal was drastically amplified when using capacitors not able to withstand cryogenic temperatures in the PMT base [101]. This suggests that the effect is electrostatic in nature, and probably due to capacitive coupling between the PMT and wire-plane. This is also suggested by the similarity between the signals observed and those produced by anode-coupled readout of a light collection system [77].

5.7 Initial Performance of the MicroBooNE Light Collection System

The system was first powered on after the cryostat had been filled with liquid argon. All the PMTs in both the primary and secondary system were found to be operational. Figure 45 shows the waveforms for all the PMT channels around the time that a large pulse, potentially from a cosmic ray muon, is observed. After initial checks of the system's health, the single photoelectron response

1 of each PMT was set such that a one photo-electron pulse has an amplitude of 20 ADC counts as
2 seen by the PMT readout system. The flasher LED system, described previously, is used to set this
3 response. Figure 46 shows a candidate single photoelectron pulse following arrival of a TTL logic
4 pulse driving the LED flasher system. The LED light level is set so that the majority (about 80%)
5 of waveforms see no response in the region where pulses from the LED are expected to occur. This
6 ensures that for windows with pulses, the pulses are of single photoelectrons. Figure 47 shows an
7 example of the area vs. maximum amplitude of such pulses seen by a PMT during the flasher runs.

8 **6. Electronics and Readout Systems**

9 The analog signals that develop on a LArTPC during its operation must be amplified, digitized,
10 and written to disk for use in analysis. Custom low-noise electronics that are capable of operating
11 in the liquid argon environment have been developed for this purpose in MicroBooNE. The data
12 from these LArTPC electronic channels, as well as from the PMTs, is sent to a readout system that
13 digitizes and organizes the information before passing it along to a Data Acquisition (DAQ) system
14 that stores it on disk. The stages of signal processing are illustrated in figure 48. The following sub-
15 sections describe the LArTPC cold electronics, the LArTPC and PMT readout electronics systems,
16 and the DAQ system in more detail. Details of triggering capabilities available in MicroBooNE are
17 also provided in this section.

18 **6.1 Cryogenic Low-Noise Electronics**

19 To obtain optimum detector performance, MicroBooNE uses cryogenic low-noise front-end elec-
20 tronics for readout of the LArTPC. To reduce electronic noise, the interconnection length between
21 the LArTPC wires and preamplifier should be as short as possible thus minimizing the total capaci-
22 tance seen at the preamplifier input. To accomplish this, the analog front-end ASICs, which include
23 a preamplifier, shaper, and signal driver are located inside the cryostat in addition to the wire bias
24 voltage distribution system, decoupling capacitors, and calibration networks. The front-end ASIC
25 and associated circuits are implemented on a cold mother board which is directly attached to wire
26 carrier boards on the LArTPC itself. Cold cables are used to transmit output signals from cold
27 motherboards to warm interface electronics installed on the top of signal feed-through flanges.

28 **6.1.1 CMOS ASIC**

29 The analog front end ASIC is designed in 180 nm CMOS technology, which integrates both the
30 preamplifier and shaper on a single chip. Each chip has 16 channels to read out signals from 16
31 wires. Each channel also has a charge injection capacitor for precision calibration. In MicroBooNE,
32 the shaper has 4 programmable gain settings (4.7, 7.8, 14 and 25 mV/fC) and 4 programmable
33 peaking time settings (0.5, 1.0, 2.0 and 3.0 μ s) that provide increased flexibility to the readout
34 system. The ASIC also has programmable baseline settings (200 or 900 mV) to accommodate
35 different detection wire configurations: either collection or induction plane. It has a selectable
36 AC/DC coupling mode with a 100 μ s time constant for the AC coupling mode which can be used
37 to reduce low frequency noise. The ASIC also has built-in band-gap reference and temperature
38 sensors to facilitate biasing and monitoring.

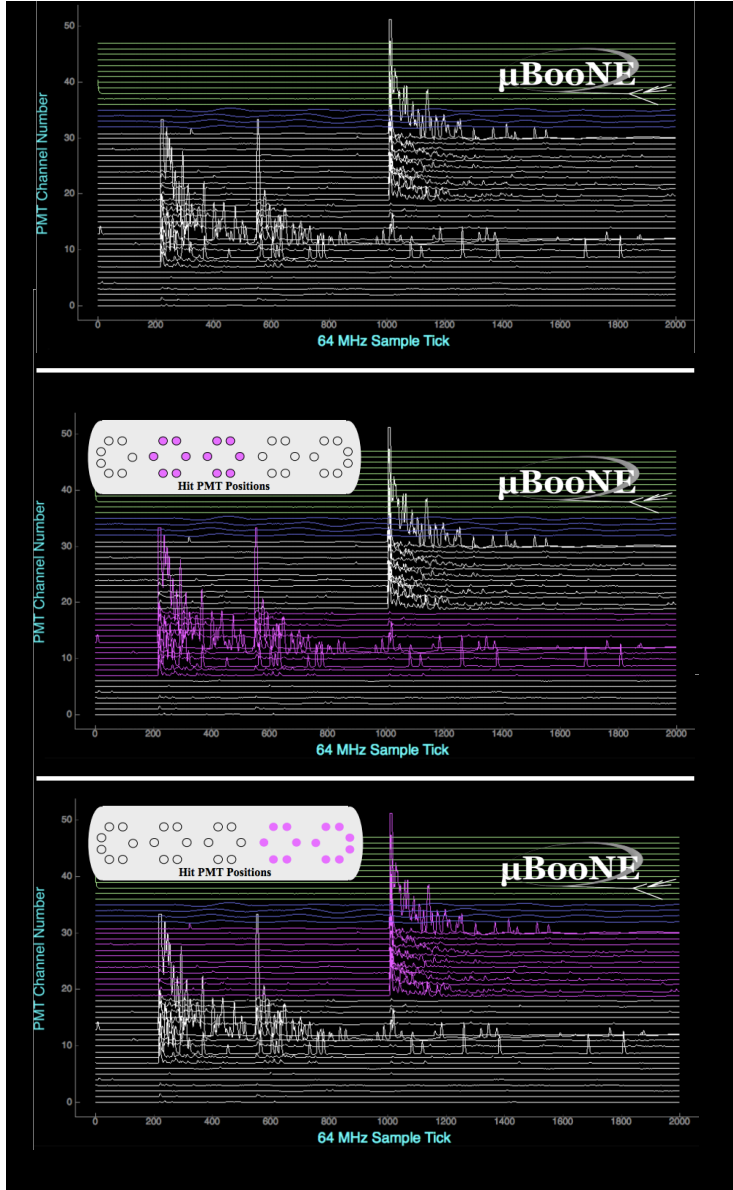


Figure 45: Top: Example waveforms from all 32 PMTs of the primary light collection system over a 31.25 microsecond readout window. The waveforms from the PMTs are in white. The blue waveforms are from the secondary lightguide PMTs, which are off in this picture. Waveforms from channels reserved for logic inputs are shown in green. In this image, the PMTs see two successive flashes of light at different parts of the detector. Middle and Bottom: Magenta highlights the early and late pulse, with the insets showing the PMTs which fired. Each pulse is likely from two cosmic ray muons traveling through the detector.

1 The CMOS ASICs consume only \sim 6mW/channel in its default configuration. The front end
 2 ASICs of the entire detector generate \sim 50 W of heat load that is easily handled by the cryogenics
 3 system. Design guidelines that constrain the electric field and the current density to address the
 4 lifetime of CMOS devices operated at cryogenic temperatures have been applied to every single

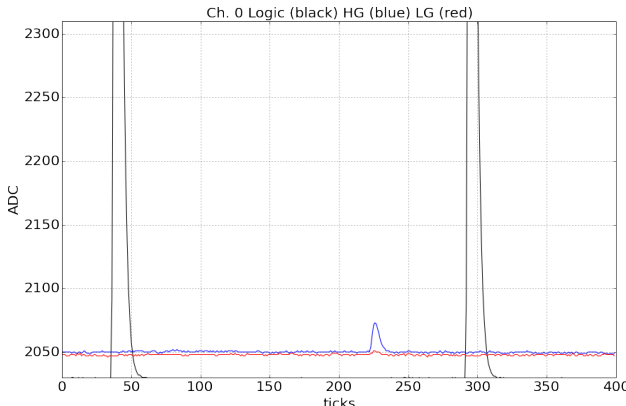


Figure 46: Example waveform captured by the PMT readout electronics during single photoelectron calibrations. The black waveform is of logic pulses that mark time at which an LED in the flasher system is driven. After some delay coming from PMT cable lengths and the flasher system, a candidate single photoelectron pulses is seen.

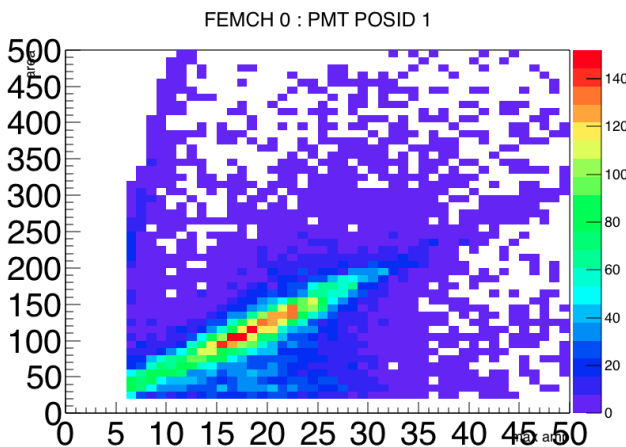


Figure 47: Distribution of the maximum amplitude and charge of pulses collected during an LED flasher calibration run. The central distribution of events is due to single photoelectron pulses.

1 transistor (total \sim 15,000 transistors) in the ASIC design. A picture of the layout of the CMOS
 2 ASIC is shown in figure 49. Test results agree well with simulations and indicate that the ana-
 3 log and the digital circuits (including the digital interface) operate as expected in the cryogenic
 4 environment.

5 The MicroBooNE LArTPC has 8,256 readout channels and a total of 516 CMOS ASICs are
 6 required to fully instrument the detector. The production testing of the CMOS ASICs required
 7 two steps: both a warm and cold test. The warm test was performed with a dedicated test board
 8 housed in a Faraday box containing a socket to house the ASIC for ease in chip exchange. All
 9 programmable parameters (gain, peaking time, baseline, AC/DC coupling etc.) were exercised
 10 with the warm test setup for careful screening at room temperature. The yield of the warm testing
 11 of the ASICs was \sim 89%. ASICs must have passed the warm test before going through cold testing.
 12 The cold test was performed with a dedicated test board containing 6 sockets to facilitate testing

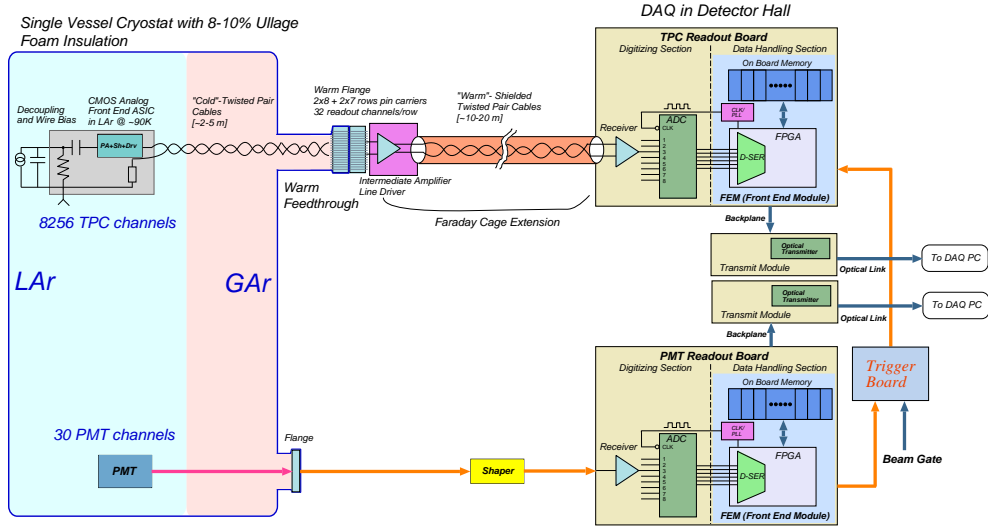


Figure 48: MicroBooNE LArTPC and PMT signal processing and readout stages.

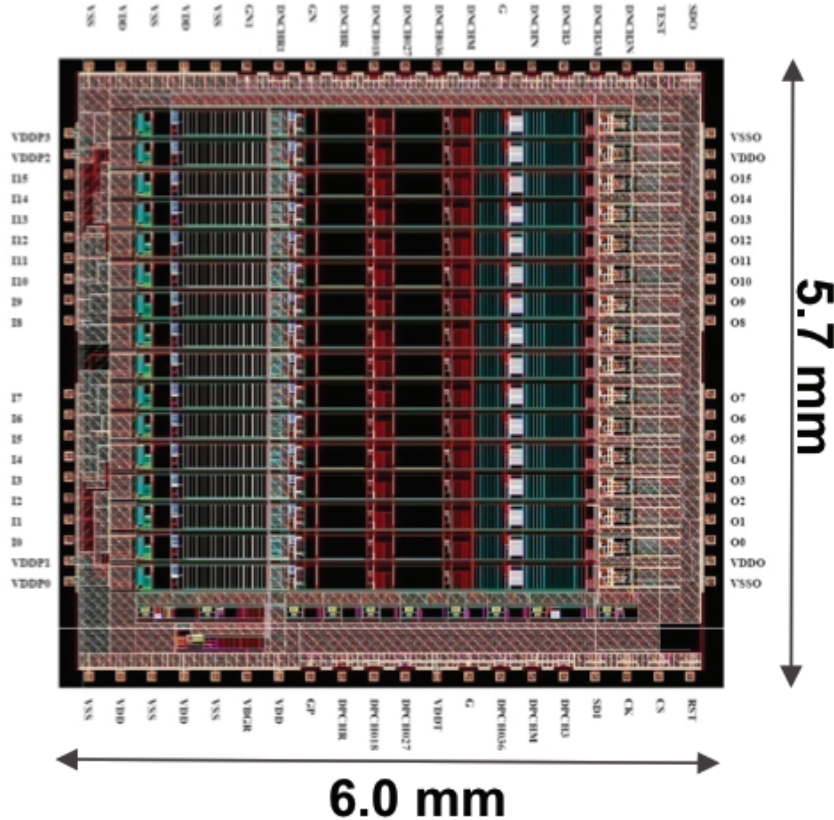


Figure 49: Layout of the CMOS analog front end ASIC

¹ of multiple chips in liquid nitrogen at the same time. A total of 201 ASICs went through cold
² testing with a yield of $\sim 97\%$. Based on this high yield, it was decided not to continue the cold

1 screening test on the rest of the production chips, as they were tested cold after being installed on
2 the motherboard. After enough (\sim 600) ASICs passed the production screening test, they were sent
3 to an assembly house to equip the cold motherboard.

4 **6.1.2 Cold Motherboards**

5 A cold motherboard was designed to house the MicroBooNE CMOS ASICs. In this capacity,
6 the motherboard provides signal interconnections both between the detector wires and preampli-
7 fier inputs as well as between the driver outputs and cold cables to the signal feed-through. The
8 cold motherboard design provides sufficient protection of the ASICs against electrostatic discharge
9 during installation. It also provides a calibration network and bias voltage distribution for the
10 wire planes. Specifically, a calibration signal enters the cryostat via a feed-through and reaches
11 the preamplifiers through the motherboard. Each preamplifier channel in the ASIC has a built-in
12 switch to individually cycle the calibration injection. The bias voltage reaches the LArTPC wires
13 via a two-fold redundant path on the motherboard that allows the detector to operate normally even
14 if one bias voltage channel fails. Use of Rogers 4000 series as the base material of the cold moth-
15 erboard avoids the potential risk of contamination of the liquid argon. The Rogers material has
16 a similar temperature expansion coefficient as the surface mounted components which enhances
17 the reliability of the electronics assembly when operated at cryogenic temperatures. The different
18 positions of the wire attachments along the top and sides of the LArTPC requires 2 types of cold
19 motherboard. The top version of the motherboard has 192 readout channels that includes 96 Y
20 channels, 48 U channels, and 48 V channels. The side version of the motherboard has 96 readout
21 channels that are either U or V channels. A picture of the top version of a cold motherboard with
22 12 mounted ASIC chips is shown in figure 50.



Figure 50: Top version of cold motherboard with 12 ASIC chips including 6 chips are mounted on top layer and 6 chips on bottom layer

23 The MicroBooNE LArTPC required a total of 36 top version motherboards and 14 side version
24 motherboards to instrument the full detector. A test stand was built for testing of the front end
25 electronics. This test stand included a full readout chain from the cold motherboard, cold cable,
26 signal feed-through, warm interface electronics, warm cable and Receiver ADC board to a DAQ
27 board based on a Xilinx ML605 FPGA evaluation board which sends acquired data to a PC over
28 a Gigabit Ethernet. The production test of each motherboard also involved both a warm and cold

1 test. Both tests used the same test stand, except the motherboard was placed in a Faraday box for
2 the warm test and submerged in a liquid nitrogen dewar for the cold test. Noise, gain, peaking
3 time, and linearity parameters were measured in both warm and cold to screen the motherboard.
4 Motherboards had to pass both tests before being installed on the detector.

5 **6.1.3 Cold Cables**

6 Cold cables transmit the detector signals from the cold motherboard to an intermediate amplifier
7 on top of the signal feed-through and distribute power to the CMOS ASICs. The cold cable is a
8 custom-built 32-pair twisted pair flat ribbon cable with Teflon FEP insulation and 100Ω ($\pm 10\%$)
9 impedance, using AWG 26 stranded wire with silver-plated copper. Custom designed shells with
10 jack screws used in the cable assembly ensured proper alignment of the insertion on the signal
11 feed-through pin carriers. The twisted pair cable was ordered from the manufacturer and sent
12 to a company to be woven into flat ribbon cables. Cold cables of two different formats were
13 assembled by an assembly house: signal cables and service cables. Signal cables are used to
14 transmit amplified detector signals while the service cable is used to transmit calibration pulses
15 and slow control/monitoring signals. Signal cables were produced in three different lengths: 80
16 inch, 100 inch and 180 inch to accommodate the different lengths between the cold motherboards
17 and the signal feedthroughs, while the service cables were produced in two different lengths: 100
18 inch and 180 inch. All of the cold cable assemblies were tested with a cable tester in the assembly
19 house before they were shipped out. In addition, $\sim 10\%$ of the cold cables were tested in the test
20 stand at BNL to confirm the quality of the cable assembly.

21 **6.1.4 Electronic Calibration**

22 The MicroBooNE cold electronics include a precision charge calibration system. Through the cold
23 cable and calibration network on the motherboard, a calibration signal enters the cryostat via a
24 feed-through and reaches the preamplifiers. A built-in switch in the ASIC makes it possible to
25 power cycle the calibration injection for every channel individually. The electronics calibration is
26 based on charge injection through known capacitances (180 fF) in the ASIC. This system enables
27 gain (charge sensitivity) calibration, verification of sense wire integrity and noise measurements.
28 The built-in electronics calibration capability is an important tool in testing and characterizing the
29 overall performance of the detector readout system. It was extensively used in the cold electronics
30 production testing and the electronics checkout during installation, commissioning, and data taking.

31 **6.1.5 Performance Tests**

32 The development of the analog front end ASICs was initiated using 180 nm CMOS technology
33 and 300 K models, though the performance parameters are extracted at 77 K. CMOS was found
34 to function at cryogenic temperatures with increased gain and lower noise. The noise, gain, and
35 pulse shaping were found to be as expected in evaluation tests of the ASICs. Extensive testing of
36 the ASICs mounted on the motherboards was performed; these tests were done in liquid nitrogen
37 rather than at room temperature, since noise levels and characteristics of the ASIC performance in
38 liquid nitrogen are similar to the performance in liquid argon. Thus, cold tests were performed on
39 all production cold motherboards fully populated with 12 chips. A total of $\sim 2,200$ chip-immersions
40 were accumulated in liquid nitrogen without any failures due to thermal contraction or expansion.

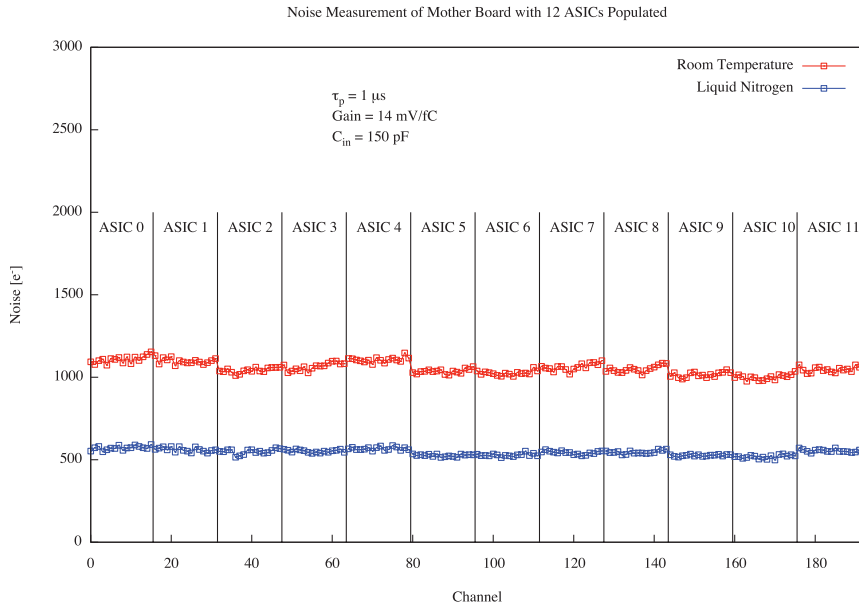


Figure 51: Plot of noise vs. temperature of 12 ASICS, total 192 channels. Noise is $\sim 1,200e^-$ at 293K, and $\sim 550e^-$ at 77 K with 150 pF C_d

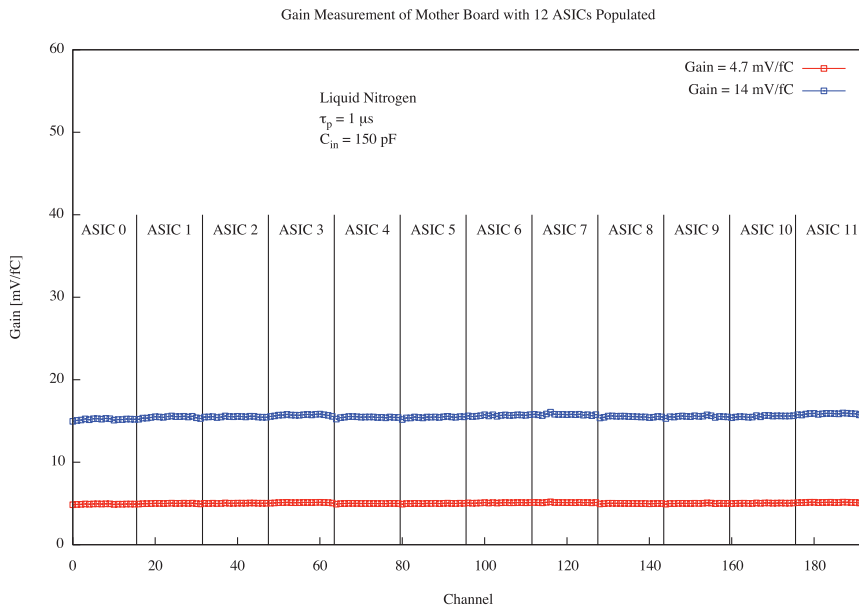


Figure 52: Plot of gain uniformity of 12 ASICS, total 192 channels, at 77 K with two different gain settings

1 The test results show the noise of the front end readout electronics system decreasing uni-
2 formly for all 768 channels from $\sim 1,200e^-$ at 293 K to less than $600e^-$ at 77 K with 150 pF

1 detector (sense wire) capacitance. A plot of noise versus temperature of 12 ASICs for a total of
 2 192 channels is shown in figure 51. The response of the front end electronics exhibits excellent uni-
 3 formity at cryogenic temperatures. As shown in figure 52, the gain variation of a cold motherboard
 4 with 12 ASICs is only $\sim 7\%$ peak-to-peak across 192 channels. The spread of the gain variation is
 5 only $\sim 1\%$ of the gain setting.

6 6.2 Warm Electronic Amplification

7 Signals from the cold electronics are carried over the cold cables to dedicated feedthroughs mounted
 8 on the cryostat. The cold cables are connected to pin-carriers located on 14-inch CF signal feedthrough
 9 flanges that are mounted on nozzles N1A-N1K of the cryostat (see figure 5). The signal feedthrough
 10 design must accommodate 100% hermeticity and high signal density. A design based on the AT-
 11 LAS pin carrier style was developed for this purpose. Two 8-row pin carriers and two 7-row pin
 12 carriers are welded onto the 14-inch CF flange, as shown in figure 53, and create a vacuum-tight
 13 seal. Nine of the 11 signal feedthroughs receive signals from the three LArTPC anode planes (384
 14 Y-plane, 192 U-plane, 192 V-plane), while the remaining two on the extreme ends of the cryostat
 15 only receive signals from one of the angled induction planes (672 U-plane on one feedthrough, 672
 16 V-plane on the other).

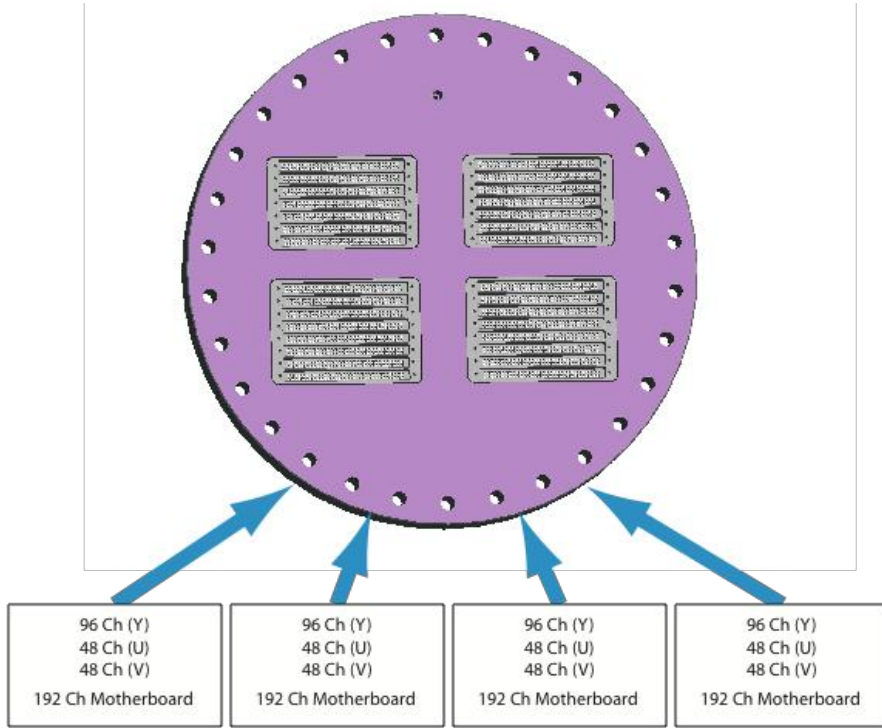


Figure 53: Signal feedthrough flange consisting of a 14-inch CF flange with two 8-row and two 7-row pin carriers welded in place.

17 A Faraday cage is mounted on the external, warm, side of the signal feedthroughs to provide
 18 shielding for the intermediate amplifiers located inside. The bias voltage feedthrough, which sup-

plies anode plane bias voltages into the cryostat, is built onto a small 2.75-inch CF flange welded onto the signal feedthrough flange. A filter board mounted on the bias voltage flange filters noise and ensures a good ground connection. Figure 54 shows details of the signal feedthrough assembly with electronics boards, bias voltage feedthrough, and Faraday cage.

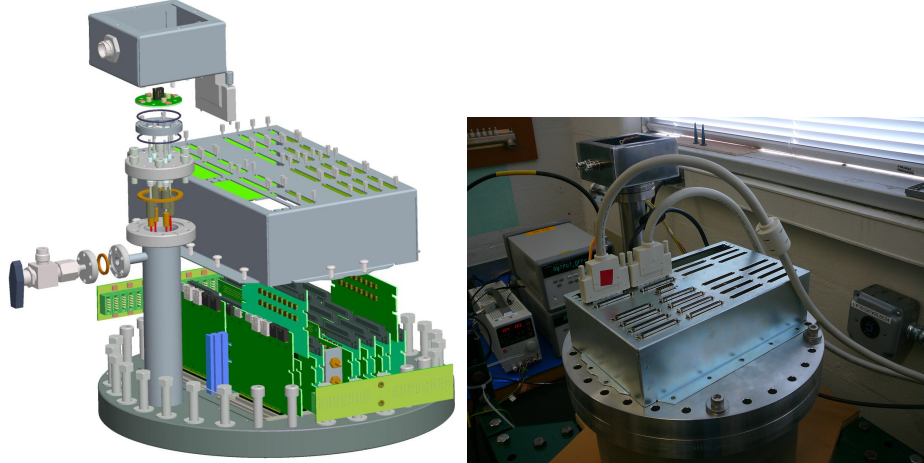


Figure 54: Left: Diagram of the signal feedthrough assembly, which includes intermediate amplifiers, Faraday cage, bias-voltage feedthrough and filtering circuit. Right: Photograph of one of the feedthrough assembly, partially constructed and being tested.

The intermediate amplifiers provide ~ 12 dB gain to the LArTPC signals to make them suitable for transmission over a 20 m long cable to the readout electronics (see section 6.3). Each intermediate amplifier has 32 channels installed on the signal feedthrough flange and housed inside the Faraday cage to provide noise isolation. Figure 55 shows a picture of a prototype intermediate amplifier plugged on the signal feedthrough pin carrier. The intermediate amplifier uses a 68-pin SCSI-3 connector to drive the 32 channels of signal differentially for better noise immunity. The layout and connector position have been carefully designed to ensure the card can be plugged on the pin carrier in either direction. This efficiently utilizes the limited available space on the top of the feedthrough, which also makes the design of the Faraday cage easier.

In addition to the intermediate amplifiers, there are two service boards mounted on the top of each signal feedthrough. The service board provides regulated low voltage, control and monitoring signals to the analog front end ASICs. It also provides pulse injection to the preamplifiers for precision calibration. The control, monitoring, and calibration signals are provided to the front end electronics with two-fold redundancy. Should one set of signals become defective the detector can still operate normally with the redundant set. Each service board plugs onto a 64-pin carrier row. Figure 55 shows a picture of a prototype service board.

6.3 Readout Electronics

The MicroBooNE readout electronics system consists of two subsystems: the LArTPC and PMT readout electronics. The LArTPC readout electronics are responsible for the readout, digitization, and processing of the induction and collection wire signals after amplification. The PMT readout



Figure 55: Left: Photograph of one of the intermediate amplifier boards plugged into a pin carrier during testing. Right: Photograph of a prototype service board.

1 electronics are responsible for the amplification, shaping, digitization, and handling of PMT signals, as can be used to provide a trigger signal for the readout and data acquisition systems. While
2 the LArTPC and PMT readout systems share the same back-end design that organizes and packages
3 the data for delivery to the DAQ system, they employ different analog front-end and digitization
4 designs, which are described in this and the following subsection.

6 The LArTPC readout electronics are responsible for processing the signals from the 8,256
7 wires in MicroBooNE after pre-amplification and shaping in the cold electronics (section 6.1).
8 The pre-amplified and shaped analog signals from the cold electronics are transmitted to the warm
9 electronics outside the cryostat, as described in section 6.2, and then passed to custom-designed
10 LArTPC readout modules distributed evenly over nine readout crates. The readout modules digitize
11 the analog signals and then process and prepare them for shipping to designated DAQ machines
12 (one per readout crate) (section 6.6).

13 The LArTPC readout crates communicate with the DAQ machines via three duplex 3.125
14 Gbits/sec optical links that connect to a crate controller module and data transmitter (XMIT) mod-
15 ule on the crate end, and to three PCI Express boards on the DAQ machine end. The controller
16 is responsible for configuration, trigger and run control command distribution as well as the slow
17 monitoring of each readout crate. The controller occupies one of the optical links while the XMIT
18 is responsible for sending two separate streams of readout data to the DAQ machines via the two
19 other optical links. The first XMIT stream contains losslessly compressed LArTPC data associ-
20 ated with event triggers received by the LArTPC readout crates, such as the BNB trigger, and
21 is referred to as the “NU” data stream. The second stream is a continuous LArTPC data stream
22 which is compressed with some data loss. The continuous data stream is used for beam-unrelated
23 physics analyses, such as the study of potential supernova neutrino events, and is referred to as
24 the “SN” data stream. The compression schemes used in the NU and SN streams are described in
25 section 6.3.3.

26 All readout crates are synchronized to a common 16 MHz clock. The clock sync is provided
27 by a clock fanout board which shares the same ground as all readout crates, and is sent via coaxial
28 cable to a distribution board which is mounted on each crate backplane. The readout frame size
29 is set to 1.6 ms, which is equivalent to the time it takes for charge produced on the far end of the

1 LArTPC to drift to the wire planes at the design cathode voltage of -128 kV.

2 **6.3.1 Data Digitization**

3 The amplified and shaped analog LArTPC signals are differentially received and digitized in the
4 first section of the readout modules. Each ADC module holds 8 AD9222 octal-channel 12-bit
5 ADCs. Each ADC module handles signals from 64 wires. The wire signals are grouped in two
6 sets of 32 consecutive wire channels: either 32 induction wires plus 32 collection wires or two sets
7 of 32 induction wires. The induction channel sequence alternates wires between the two induction
8 planes. The ADC module digitizes the signals continuously at 16MHz. Each channel has a config-
9 urable baseline, which is either set low (450 ADC counts) for collection channels or at the middle
10 of the dynamic range (2055 ADC counts) for induction channels, thus ensuring that both the collec-
11 tion plane unipolar differential signals and the induction plane bipolar differential signals can make
12 use of the full ADC analog input range. The requirement to observe a MIP produced at the far end
13 of the LArTPC in the induction plane determines the lower end of the dynamic range, while the
14 requirement to observe a highly-ionizing stopping proton at the close end of the LArTPC without
15 saturation sets the upper end. The digitized outputs from the ADC board are passed directly to a
16 Front End Module (FEM) in the second section of the LArTPC readout module. The FEM houses
17 an FPGA for data processing, data reduction, and preparation for readout by the DAQ system as
18 described in the following section.

19 **6.3.2 Data Handling**

20 The FEM board consists of a 14-layer printed circuit board which is mechanically integrated with
21 the ADC board as illustrated in figure 56. The choice of a smaller board allows for short trace
22 lengths which is beneficial for high speed signals. The full assembly comes together as a standard
23 VME 9U card in height, with a 280 mm depth. Differential outputs from the ADCs connect to the
24 FPGA through HM-Zd connectors that have individual ground shielding on each differential pair.

25 The digitized data stream moves from the ADCs to a Stratix III Altera FPGA, which reduces
26 the sampling rate of the ADC from 16 MHz to 2 MHz. The 2 MHz sampling rate is optimized by
27 taking into consideration the expected pulse shape provided by the convolution of the cold electron-
28 ics, the expected LArTPC field responses, and the $O(1\mu s)$ diffusion effects which govern charge
29 drift within the liquid argon. The FPGA stores the data from all 64 wires per board sequentially in
30 time in a $1M \times 36$ bit 128 MHz SRAM, grouping two ADC words together in each 36 bit memory
31 word. This requires a data storage rate of $(64/2) \times 2$ MHz = 64 MHz. The SRAM chip size and
32 memory access speed allow for continuous readout of the LArTPC data. Since data reduction and
33 compaction algorithms rely on the sequential time information of a given wire, the data readout out
34 from this SRAM takes place in wire order in alternate clock cycles, again at the rate of 64 MHz.
35 This read in/out sequence is illustrated in figure 57.

36 Separate DRAM multi-event buffers on the FEM store the NU and SN data streams. The data
37 divert into the NU readout stream when a trigger is issued and received (as shown in figure 58)
38 which signals, for example, an accelerator neutrino-induced event. When an event trigger is re-
39 ceived, 4.8 ms worth of data, relevant to that event, are packeted per channel and sent to the DAQ
40 through the NU data stream. The 4.8 ms readout size is governed by the maximum drift time and
41 spans three or four frames. In order to reduce the amount of data being transmitted, the FPGA

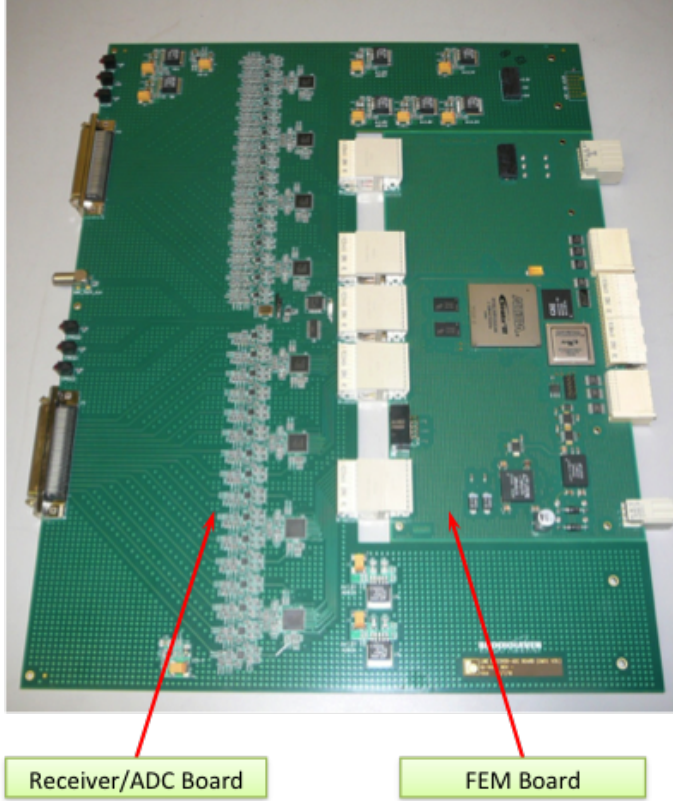


Figure 56: LArTPC ADC+FEM board.

1 trims the three or four frames to span the exact 4.8 ms required, 1.6 ms before the trigger plus 3.2
 2 ms after the trigger. In parallel, the data is continually sent out through the SN data stream, frame
 3 by frame. The compression and data reduction algorithms applied to each of the two streams are
 4 described in the following section.

5 After processing by the FPGA, the data passes to the crate backplane dataway on connectors
 6 shown in figure 56. A token-passing scheme is utilized to transfer data from each FEM board to the
 7 data transmitter module (XMIT) in a controlled way, whereby each FEM, in the order of closest to
 8 furthest from the XMIT module, receives a token, transmits its data to the XMIT, and passes the
 9 token on to the next FEM in the sequence. For the NU stream, each FEM sends all data associated
 10 with a particular trigger number; while for the SN stream, each FEM sends all data associated with
 11 a particular frame number. This data transfer is relayed via the otherwise passive crate backplane,
 12 and is limited to 512 MB/s. In the XMIT module, the data is buffered temporarily and sent to the
 13 DAQ machine through the two streams, SN and NU, which proceed effectively in parallel.

14 **6.3.3 Compression Schemes**

15 In the case of the NU data stream, a lossless Huffman coding scheme implemented in the FEM
 16 FPGA compresses the data by approximately a factor of five. Further reduction in the overall
 17 rate is achieved by exploiting a PMT trigger in coincidence with the BNB trigger, as described in
 18 section 6.5. Huffman coding provides for lossless data compression by taking advantage of the

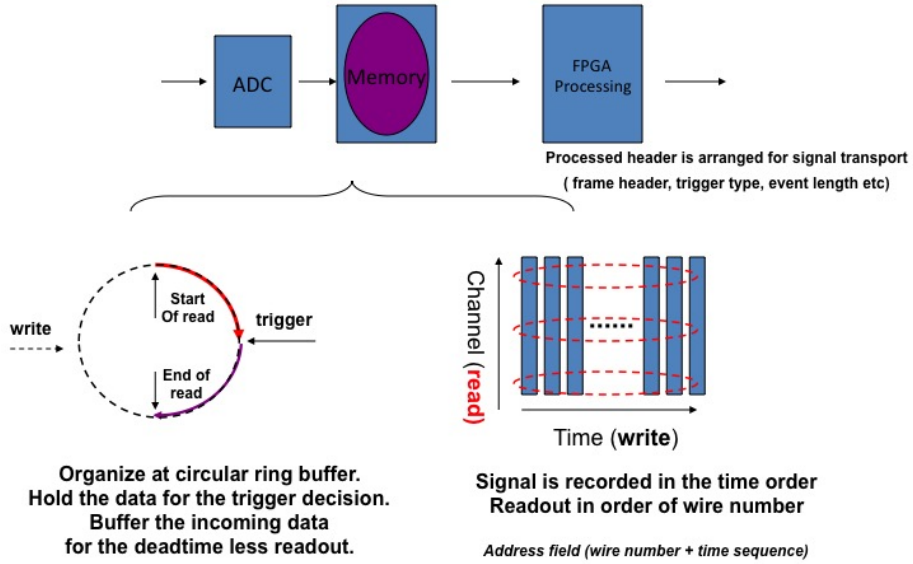


Figure 57: LArTPC readout sequence in the TPC FEM.

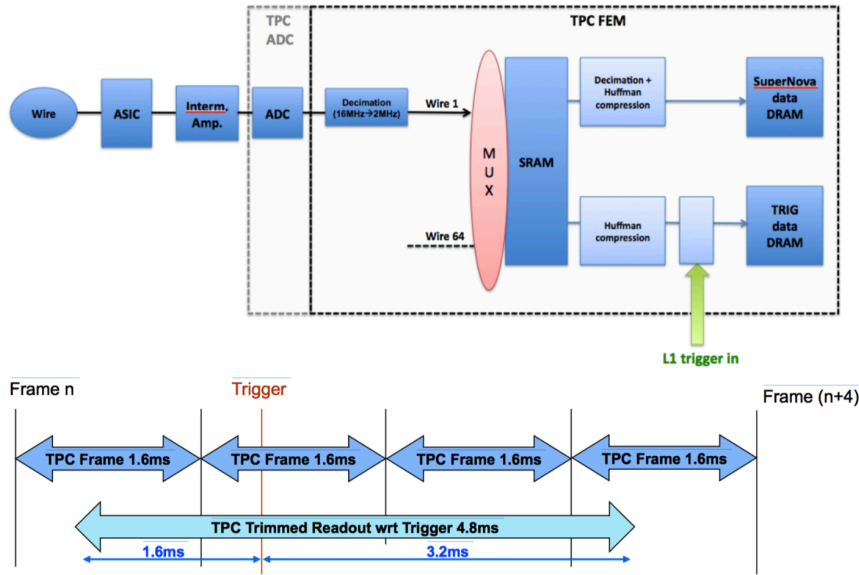


Figure 58: LArTPC trigger readout.

1 slow variation of the waveform TPC data in any given channel. In particular, this compression
 2 scheme relies on the fact that successive data samples on any given wire vary relatively slowly in
 3 time. As such, when noise levels are low, any two adjacent data samples either coincide or differ
 4 by 1 ADC count. The most frequent values for the difference in ADCs between successive data
 5 samples are assigned pre-specified bit patterns with the lowest number of bits possible. Those bit

1 patterns are encoded in the 16-bit data words that would otherwise be used for a single 12-bit ADC
 2 sample value. As such, data reduction of up to a factor of 14 is theoretically possible¹. In practice,
 3 the data reduction is sensitive to noise levels and LArTPC activity, and is also dependent on the
 4 gain setting. The compression factor achieved by MicroBooNE is shown in figure 59.

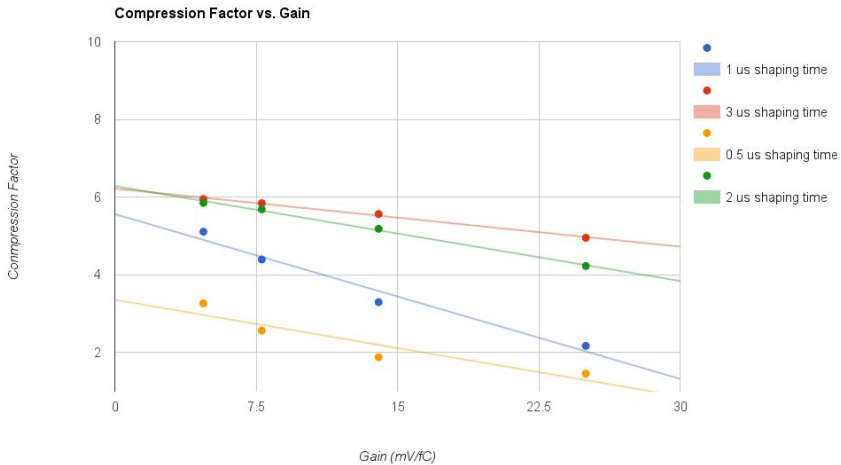


Figure 59: Compression factors achieved on ADC data with Huffman compression.

5 Because of the low trigger rate², lossless Huffman coding compression proves sufficient for the
 6 NU data stream. However, for the continuous SN stream, further compression becomes necessary,
 7 resulting in unavoidable data loss. A method called “dynamic decimation” (DD) handles this case.
 8 The DD scheme relies on recognizing regions of interest (ROI) in the data stream that contain
 9 waveforms corresponding to drift ionization charges. Portions of the data stream not containing
 10 ROI contribute to pedestal determination, and ROI are identified as deviations from the continually-
 11 updated pedestal, buffered, and read out to disk. At the time of this writing, the MicroBooNE SN
 12 stream compression scheme is being finalized and the SN readout stream will be commissioned in
 13 September 2016.

14 6.4 PMT Readout Electronics

15 The PMT readout electronics are responsible for processing signals from the 32 PMTs described
 16 in section 5 and identifying light signatures coincident with the BNB and NuMI beam spills. The
 17 coincidences generate PMT triggers that can be later mixed with other triggers in the Trigger Board
 18 (TB). Signals from the 4 light paddle guides installed in the LArTPC are also recorded by the PMT
 19 readout electronics, but these signals do not participate in the PMT trigger generation.

20 The stages of signal processing are illustrated in figure 60. First, each PMT signal (with the
 21 exception of the light paddle guide signals) is split into two different gains, as described in sec-
 22 tion 5.2.5, with the HG channel carrying 18% of the PMT signal and the LG channel carrying

¹The uppermost two bits are always reserved for header information, in each 16-bit word.

²The BNB trigger dictates an upper bound on the trigger rate of 15 Hz.

1 1.8% of the PMT signal. Each gain is split once again into HG1 and HG2, and LG1 and LG2, in
 2 order to allow different processing of beam-related and beam-unrelated PMT signals. All $32 \times 2 \times 2$
 3 plus 4 signals are pre-amplified and shaped in 16-channel pre-amp/shaper boards (section 6.4.1).
 4 Four PMT readout modules receive the analog shaped signals differentially and digitize them (sec-
 5 tion 6.4.2) at 64 MHz. The PMT readout modules then process the signals in order to prepare them
 6 for shipping to a designated DAQ machine and to form a possible PMT trigger (section 6.4.3).

7 Each one of the 4 PMT ADC+FEM readout boards used in the PMT readout system handles
 8 one of the following:

- 9 • Readout of and PMT trigger generation using the HG1 PMT signals associated with neutrino
 beam events. The paddle signals are also readout by this board.
- 11 • Readout of and PMT trigger generation using the HG2 PMT signals that are out of beam
 time (i.e. cosmic rays and other cosmogenic backgrounds)
- 13 • Readout of the LG1 PMT signals associated with neutrino beam events
- 14 • Readout of the LG2 PMT signals that are out of beam time

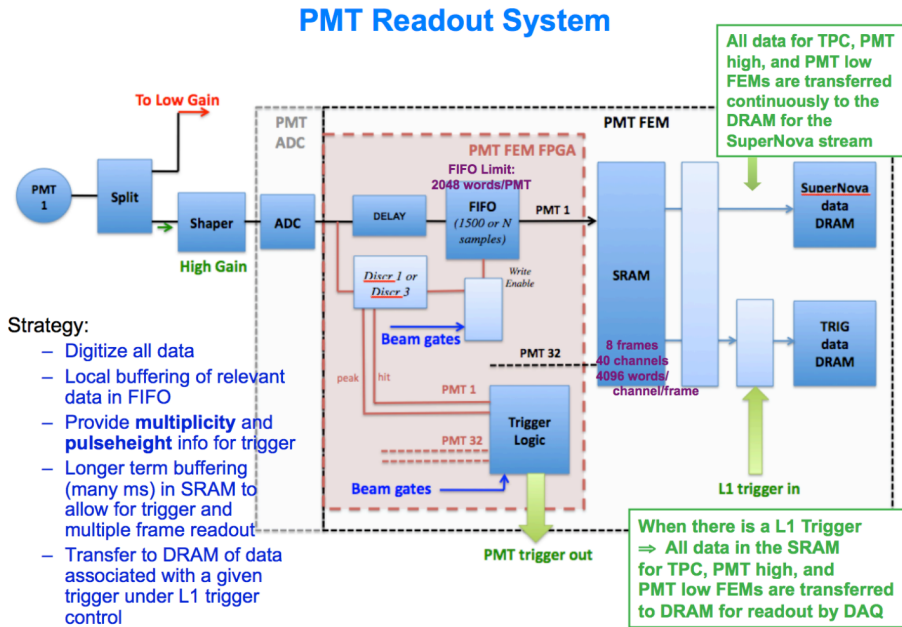


Figure 60: Signal processing in PMT FEM.

15 After signal processing, the data is sent to a designated DAQ machine via a transmitter (XMIT)
 16 module in the same way as is done for LArTPC data. Two data streams are provided: a NU data
 17 stream associated with event triggers and a SN data stream which a continuous version of the NU
 18 stream readout.

6.4.1 Signal Amplification and Shaping

The preamp/shaper boards read raw PMT signals from the PMT HV/signal splitters and shape them into unipolar signals with a 60 ns rise time. The shaped signals are sent to the LArTPC readout boards differentially via short front-panel cables, in order to minimize noise, where they are digitized at 64 MHz. The 60 ns peaking time allows digitization of two or three samples on the rising edge. This in turn enables an accurate determination of the event start time (t_0) needed to determine the x coordinates of ionization signals along the drift direction. An accurate time measurement also helps reject other tracks, such as cosmic rays, that cross the detector during the drift time.

6.4.2 PMT Data Digitization

The ADC (Texas Instruments, ADS5272) module part of the PMT readout board (figure 61) is responsible for digitization of up to 48 differentially-driven input signals. The differential signals are digitized at 64 MHz. The 64 MHz clock used by the PMT readout is generated starting from the 16 MHz clock that is common to all readout crates (LArTPC and PMT).



TEMPORARY
PLACEHOLDER

Figure 61: The PMT readout board digitizes 48 input signals. **NOTE: Missing Image!**.

In addition to HG and LG waveforms from the PMTs, each readout board also receives, digitizes, and processes beam gate signal markers which arrive $4\mu s$ before the BNB $1.6\mu s$ and NuMI $10\mu s$ beam gates. These gates are used to (a) specially mark regions of interest where PMT data are read out continuously with no compression and (b) look for coincident PMT light signatures for trigger generation.

6.4.3 Data Handling and PMT Trigger Generation

PMT information is recorded in the NU data stream for four 1.6 ms frames associated with an event

1 trigger: the frame containing the (asynchronous) trigger, the frame preceding the trigger frame,
2 and two frames following the trigger frame. To avoid the inordinate amount of data that would
3 be generated at a 64 MHz sampling rate, the FEM applies a zero-suppression immediately after
4 digitization, retaining only samples above a given threshold as well as enough information before
5 and after this useful data to establish a local baseline value; this collection of information is referred
6 to as a PMT readout ROI. An exception is formed for beam-related or other likewise-triggered data
7 where, for example, the $4\mu\text{s}$ -early BNB and NuMI beam gates mentioned in section 6.4.2 instruct
8 readout of 1500 consecutive samples ($23.4\mu\text{s}$) surrounding and including the beam gates regardless
9 of signal activity.

10 Two different discriminators are used: one that is active inside the beam gate(s), and one
11 that is also active outside the beam-gate-surrounding $23.4\mu\text{s}$. The latter discriminator governs the
12 readout activity due to cosmic rays and other non-beam related activity. The first discriminator
13 enables PMT channels with pulse heights above a configurable threshold (e.g. corresponding to 1
14 photoelectron) to participate in trigger multiplicity and pulse height sum conditions, as described
15 in the following section. The thresholds for those two discriminators are set to different levels and
16 configured with different dead times for the HG and LG signals.

17 **6.5 Level-1 Trigger Generation**

18 The TB, which physically resides in the PMT readout crate, issues a “Level-1” trigger in order to
19 flag frames that must be treated differently. In the case of the LArTPC readout, the TB flags the 4
20 frames that must be trimmed and readout through the NU data stream and, in the case of the PMT
21 readout, it flags the 4 frames that must be readout in full through the NU data stream.

22 The inputs to the TB include a BNB trigger input (maximum rate of 15 Hz), a NuMI trigger
23 input (1.25 Hz), a Fake Beam trigger input (configurable), a PMT trigger input, and two calibra-
24 tion trigger inputs, provided by the laser calibration system and the cosmic ray muon telescope,
25 respectively. The TB also has the ability to receive, via the crate controller, DAQ-issued calibration
26 triggers, which are used explicitly for cold electronics and PMT calibration. The various input
27 triggers can be independently pre-scaled, masked, and mixed together (OR or AND) to generate an
28 event trigger.

29 The FPGA firmware in the PMT FEM can generate two different types of PMT triggers based
30 on the PMT signals: a cosmic PMT trigger and a beam gate PMT trigger. Beam gate PMT triggers
31 are configured in the same way for the BNB, NuMI, and Fake Beam. The nominal criteria for these
32 triggers are (1) PMT multiplicity ≥ 1 and (2) summed PMT pulse-height ≥ 2 photoelectrons (p.e.)
33 summed over all 32 HG1 PMT channels. Both criteria must be met during any 100 ns time interval
34 coincident with the beam spill duration ($1.6\mu\text{s}$ in the case of the BNB and Fake Beam gates and
35 $10\mu\text{s}$ in the case of the NuMI gate), and only channels enabled by the beam gate discriminator can
36 participate in the active pulse-height and multiplicity sums. The criteria for a cosmic PMT trigger
37 are (1) PMT multiplicity ≥ 1 and (2) summed PMT pulse-height ≥ 40 p.e. summed over any one of
38 28 preset groups of 5 HG2 PMT channels that are grouped based on their spatial correlation. Again,
39 only channels enabled by the cosmic discriminators can participate in the trigger generation.

40 In addition, a software-based algorithm has been written to mimic the capabilities of the beam
41 gate PMT trigger performed in the FPGA and provide more flexibility in trigger criteria settings.
42 Details of this higher-level software trigger are described in section 6.7.

Figure 62 diagrams the PMT readout and trigger logic. Activation or masking of each of the trigger inputs and outputs is DAQ-controlled. The trigger condition and explicit PMT trigger type, if applicable, is available for every event in the NU data stream at both the event-building stage and offline; this information is read out via a dedicated optical data stream, directly from the TB. The trigger number and trigger time are also propagated and available in the NU data streams arriving independently at the assembler DAQ machine from each LArTPC and PMT crate, and can therefore be used to correctly associate data from the same event.

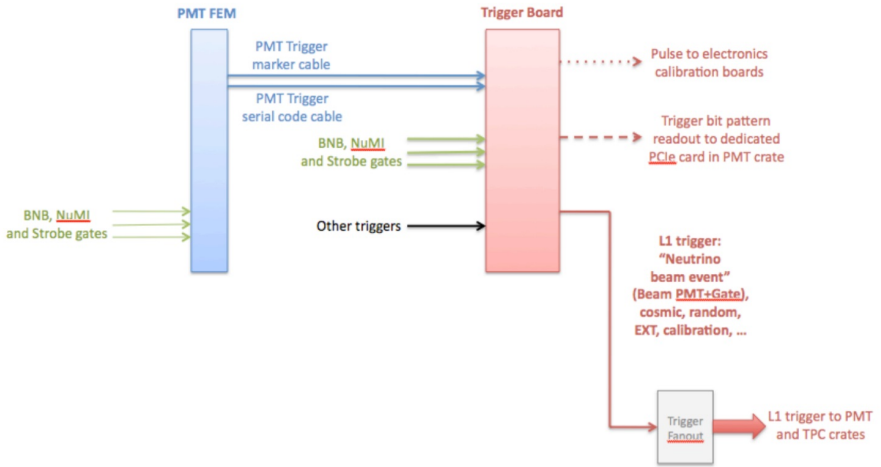


Figure 62: PMT readout and trigger logic.

The readout control sequence is illustrated in figure 63. When a trigger is generated by the TB it is passed to a fan-out module on a single cable and from there it is distributed to all crate controllers (LArTPC and PMT). Through the crate backplane, the trigger gets propagated to each FEM. An FEM that receives a trigger temporarily inhibits the SN stream with its associated decimation and initiates the loss-less readout scheme to direct the data to the appropriate readout path. SN readout resumes once the XMIT is done sending all NU data associated with an event to the DAQ.

6.6 DAQ Design

The MicroBooNE DAQ system acquires data from the readout electronics, writes data to local disk before transferring it to long-term storage, configures and controls the readout electronics during data-taking periods, and monitors the data flow and detector conditions. These tasks are performed on a network of commodity servers running both custom and open-source software.

The data from each crate of the backend electronics is sent to a dedicated server (called the sub-event buffer, or SEB) via an optical fiber, arriving in a card on the SEB's PCIe bus. A real-time application places these data in an internal buffer, collects all segments belonging to an event, and creates a sub-event fragment that may be routed to a specified destination. For the NU stream, in which the data arrives with every trigger, these fragments are sent to a single event-building machine (EVB) over an internal network. Full events are checked for consistency and written to

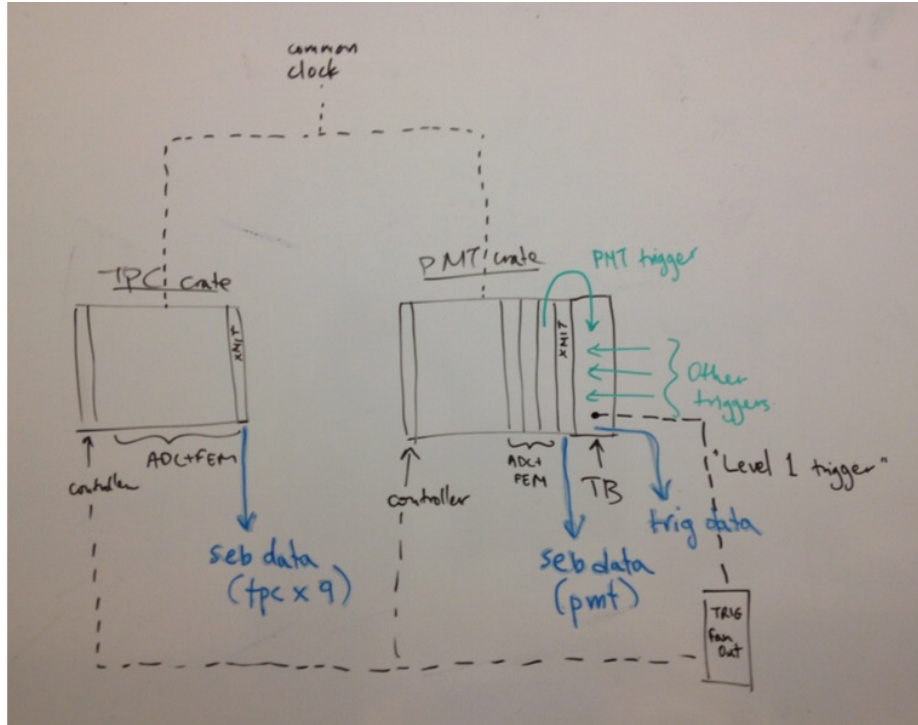


Figure 63: Readout control sequence. The MicroBooNE Level-1 trigger is a hardware trigger which consists of the OR between a BNB, NuMI, and EXT (strobe) trigger. Once received, the Level-1 trigger is propagated to all readout crates and instructs PMT and TPC data readout into ten dedicated sub-event buffer DAQ machines. The data across different DAQ machines is correlated at event building stage by the trigger number and corresponding trigger frame and sample numbers recorded in each data stream, per event. All readout crates are synchronized and correlated to the same, 16 MHz clock. **NOTE: Placeholder figure!**

1 local disk on the EVB before being sent offline for further processing. A high-level software trigger,
 2 described in section 6.7, is applied to the data to determine whether events should be written locally
 3 or ignored. For the SN stream the data remains on the SEB where it is written to disk and only sent
 4 for offline analysis on explicit requests.

5 Data writing to either triggered or SN streams is limited by the RAID6 disk write speeds which
 6 are roughly 300 MB/sec. This is much less than the network bandwidth bottleneck, which is 10
 7 Gbps. The 300 MB/sec disk write speed therefore sets the maximum aggregate rate at which all
 8 SEB fragments can ship data to the EVB without loss of data. With Huffman compression, which
 9 gives a data reduction of approximately a factor of five (figure 59) and the PMT trigger, which
 10 reduces the data rates by another factor of > 70 , this is more than sufficient for MicroBooNE's
 11 maximum 15 Hz beam spill rate. MicroBooNE expects a total triggered write rate of around 12
 12 MB/sec. The SN stream circular buffers, which will be aggressively (non-losslessly) compressed
 13 beyond what the triggered stream experiences, will fill each server's 14 TB in on the order of one
 14 day, which is ample time to respond to a Super Nova Early Warning System (SNEWS) alert [102].

15 After data is written to disk, it is then copied to another server on the internal DAQ network,

1 where the raw data is further compressed, shipped, and queued to be stored on in tape and disk
 2 cache using the Fermilab central data management system known as SAM. Offline applications
 3 then begin processing the raw data, converting the binary data format into a LArSoft [103] ROOT-
 4 based format which can be used as input for reconstruction algorithms. LArSoft is a common
 5 framework of software tools utilized by many LArTPC experiments at Fermilab and elsewhere. A
 6 separate process collects beam data and, during binary to LArSoft conversion, inserts that data into
 7 the built events. A duplicate copy of the data is also stored offsite at Pacific Northwest National
 8 Laboratory (PNNL). This collection of approximately 15 “projects” and the database which holds
 9 and monitors the state of the data flow is known as the Python/Postgres for MicroBooNE Scripting
 10 system (PUBS), and is patterned after a similar database state machine that the Double Chooz ex-
 11 periment used for data management. As PUBS pushes the data through this process, the progress of
 12 each project is monitored and viewable via GUI. PUBS can also monitor the state of the SN stream
 13 data, held locally on the SEBs. A separate offline PUBS instance controls the processing of the
 14 data, including applying newly calculated calibration constants as part of data quality management.
 15 Figure 64 schematically depicts the flow of data throughout the MicroBooNE DAQ system.

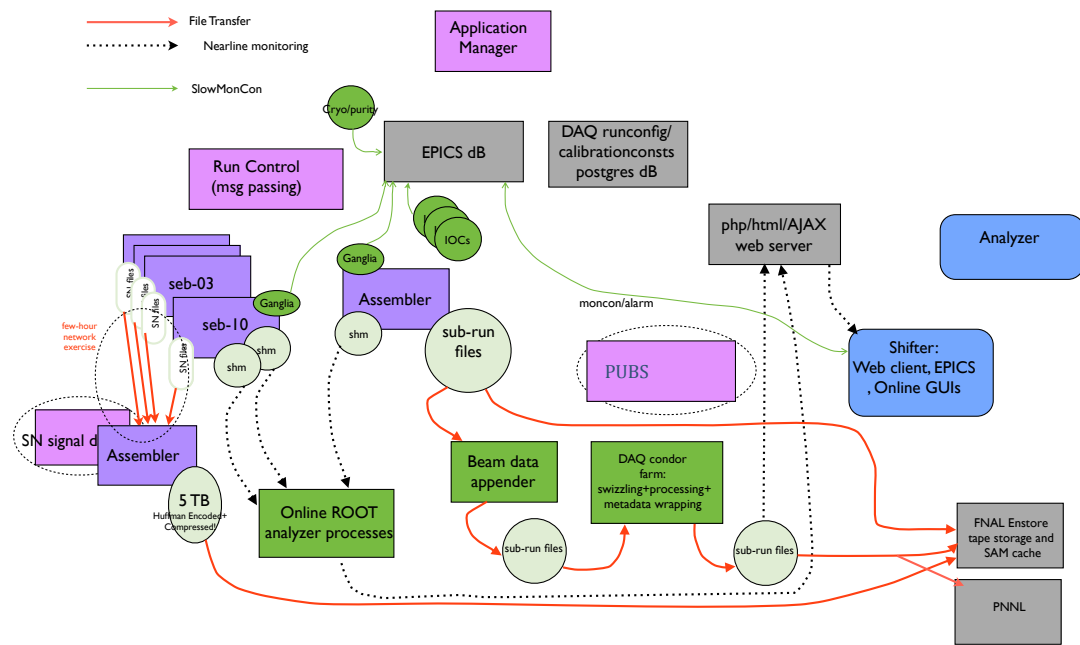


Figure 64: Data flow for MicroBooNE DAQ from raw to processed.

16 Additional software components handle the management of the main DAQ processes moving
 17 the data. A run control application issues configuration and state-progressing commands to the
 18 SEBs and EVB. Configuration states are stored in a dedicated run configuration database, which
 19 allows for the setting and preserving of configuration information for the DAQ, readout, and addi-

tional components. This database not only allows for creating the large (~ 200 parameters) intricate DAQ run configuration files, but also enforces certain conditions which must hold for consistency. For example, the configuration that initiates the ASICS charge-injection calibration also dials and captures the settings on the external pulser that drives the calibration signal and assures that ASICS gains and peaking time parameters are enforced and recorded.

Another important aspect of the system is monitoring the health of the DAQ. Monitoring of DAQ components is accomplished through Ganglia which monitors basic system states (such as CPU, memory, and network usage) as well as allows use of custom metrics to monitor the data flow and status of the readout electronics [104]. These metrics are sampled and collected by the EPICS slow monitoring and control processes, which archives desired quantities and provides alarms when pre-defined thresholds are exceeded [105]. Some examples of Ganglia metrics that are monitored and alarmed in EPICS are the rates of growth of the SEB data buffers, the fragment rates leaving each SEB, and fragment arrival rates at the EVB. Figure 65 shows examples of Ganglia metrics.

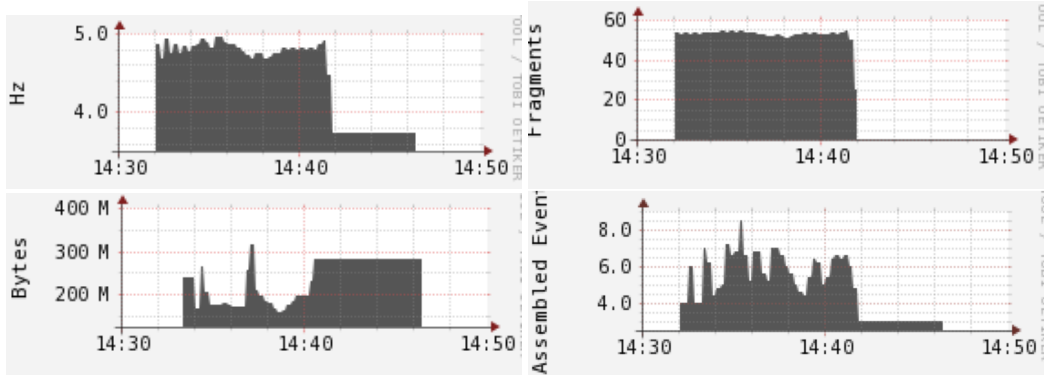


Figure 65: Ganglia metrics showing data flow on the EVB machine during a 5 Hz test run. Shown are the external trigger rate (top-left), the received fragment rate (top-right), the disk data write rate (bottom-left), and the number of assembled queued-up events waiting to be written (bottom-right). (11 fragments constitute a complete event in the MicroBooNE DAQ.)

Additional online monitoring exists to check data quality in more detail, through both programmed checks and visual checks including a real-time event display. The online monitoring takes snapshots into shared memory segments on the SEBs and the EVB, and thus provides the desired low latency checks of newly-arriving data. It continually walks through these ≈ 150 MB snap-shotted events and outputs histograms of occupancies and rates which are saved in ROOT files [106]. The histograms are then displayed in a web-based monitoring system that is easily accessible by the shift crew. Channels are aggregated in a variety of formats, including the order in which they appear in crates or across the wires and PMTs themselves. In this way, potential problems across connectors or crates, for example, may be more readily identified. Noisy, quiet, and unresponsive channels are easily marked and displayed to the shift crew. Figure 66 shows an example of available online monitoring information.

6.7 High-level software trigger

After events are collected on the DAQ event-builder server, a suite of trigger algorithms are applied

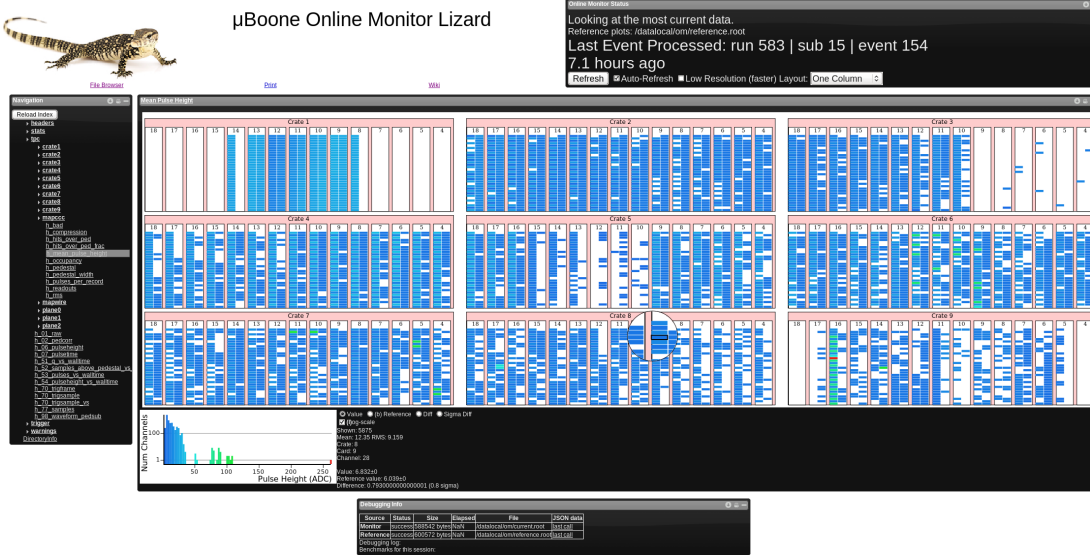


Figure 66: The online monitoring GUI (Lizard). The pedestal-subtracted ADC values for all 8256 wires in one minimum bias event are shown. Each box is a channel. Not all crates are fully populated with electronics.

to the data. Currently, these algorithms mimic the PMT readout electronics’ FPGA-based beam gate trigger algorithms, described in section 6.5. A search over the PMT digitized waveforms from the beam-spill period is performed, and if there is a significant amount of light in coincidence with the expected arrival time of the neutrinos, the event is marked and saved. This selection is performed on data that passes the level-1 trigger, which typically includes data from the BNB and NuMI beams, and randomly selected off-beam data from an “external” trigger. A fraction of the data from each of these level-1 trigger input streams is also retained via a random prescale, which provides a selection of data that has not been biased by the trigger. The high-level trigger algorithms take approximately 10 ms to return a result, a latency that is well-below the event-taking rate and so does not impact data-taking performance. The average pass rate for data-events in the PMT beam gate trigger algorithm is roughly 5%.

7. Infrastructure and Monitoring Systems

MicroBooNE is housed at LArTF, which is located on-axis to the BNB. Complete knowledge of the electrical and cryogenic systems housed within LArTF is necessary to maintain acceptable operating conditions for the experiment. Continuous monitoring of the beam being delivered to LArTF is also necessary for subsequent physics analyses. This section describes the details of infrastructure within LArTF, as well as monitoring of the experiment and beam conditions.

7.1 Electronics Infrastructure at LArTF

This section describes the electronics infrastructure of the experiment, which is essential for proper operation of the electronics that control the functioning of and extract data from the LArTPC,

1 PMTs, and other detector subsystems. Figure 67 shows a diagram of this system at LArTF, depicting
2 racks located on a platform directly above the cryostat that house electronics for: LArTPC control
3 and readout, light collection system, drift high voltage, purity monitor, calibration laser, trigger,
4 and cryogenic control systems. Additional server racks containing the data acquisition, beam timing,
5 and external network electronics are located in a separate computer room above and adjacent to
6 the above-cryostat platform. The distribution of power, data, and network connections to and from
7 all of these racks are also presented in figure 67, and is described in more detail in the following
8 sections, as are electronics safety systems and interlocks.

9 **7.1.1 AC Power Distribution and Grounding for Low-Noise LArTF Data-taking**

10 As with any large detector operating with a high dynamic range, prevention of electromagnetic
11 interference and its attendant effects on MicroBooNE data is an essential aspect of detector design.
12 MicroBooNE’s strategy for producing a low-noise environment for the LArTPC and associated
13 readout electronics can be largely summarized in a few key points. AC power distribution-related
14 items will be described here, while cabling, connections, and shielding will be described in a
15 following section.

- 16 • ‘Clean power,’ or AC power electrically isolated from AC power for the rest of LArTF
17 ('building power'), is supplied to all sensitive electronics via an isolation transformer.
- 18 • Highly sensitive electronics are housed inside the Faraday cage provided by the detector
19 cryostat or inside Faraday cages directly grounded to the cryostat.
- 20 • The detector cryostat is grounded to a ‘detector ground,’ which is physically and electrically
21 isolated from the ground provided to all other LArTF power circuits, or ‘building ground.’
- 22 • No direct electrical connections are present between detector ground and building ground.
23 This is accomplished through the use of insulating platform and cryostat saddle materials,
24 insulating cable trays and cables, and by inserting insulating ‘breaks’ (i.e. fiber data links
25 or insulating cryo pipe sections) when connections between sensitive and potentially noisy
26 detector components are necessary.
- 27 • Indirect pickup on clean signals through capacitive coupling to adjacent noise sources is
28 minimized through use of detector-grounded shielding and electrically-insulating cable trays.
- 29 • Ground loops on detector ground are avoided wherever possible by connecting all electronics
30 racks directly to the cryostat and by minimizing direct electrical connections between racks.
- 31 • Direct or capacitive couplings between building and detector ground are constantly monitored
32 during installation and operation with a custom-designed impedance monitor.

33 A line drawing describing the production of clean power and clean ground are shown in figure
34 68. Two 200-Amp clean power circuits produced at isolation transformers are used to power all
35 sensitive racks, which are indicated in figure 67. All racks containing LArTPC readout electronics
36 are placed on one circuit, while all other sensitive equipment is placed on the alternate circuit. On
37 the platform, all racks utilize clean power with the exception of the calibration laser and in-line

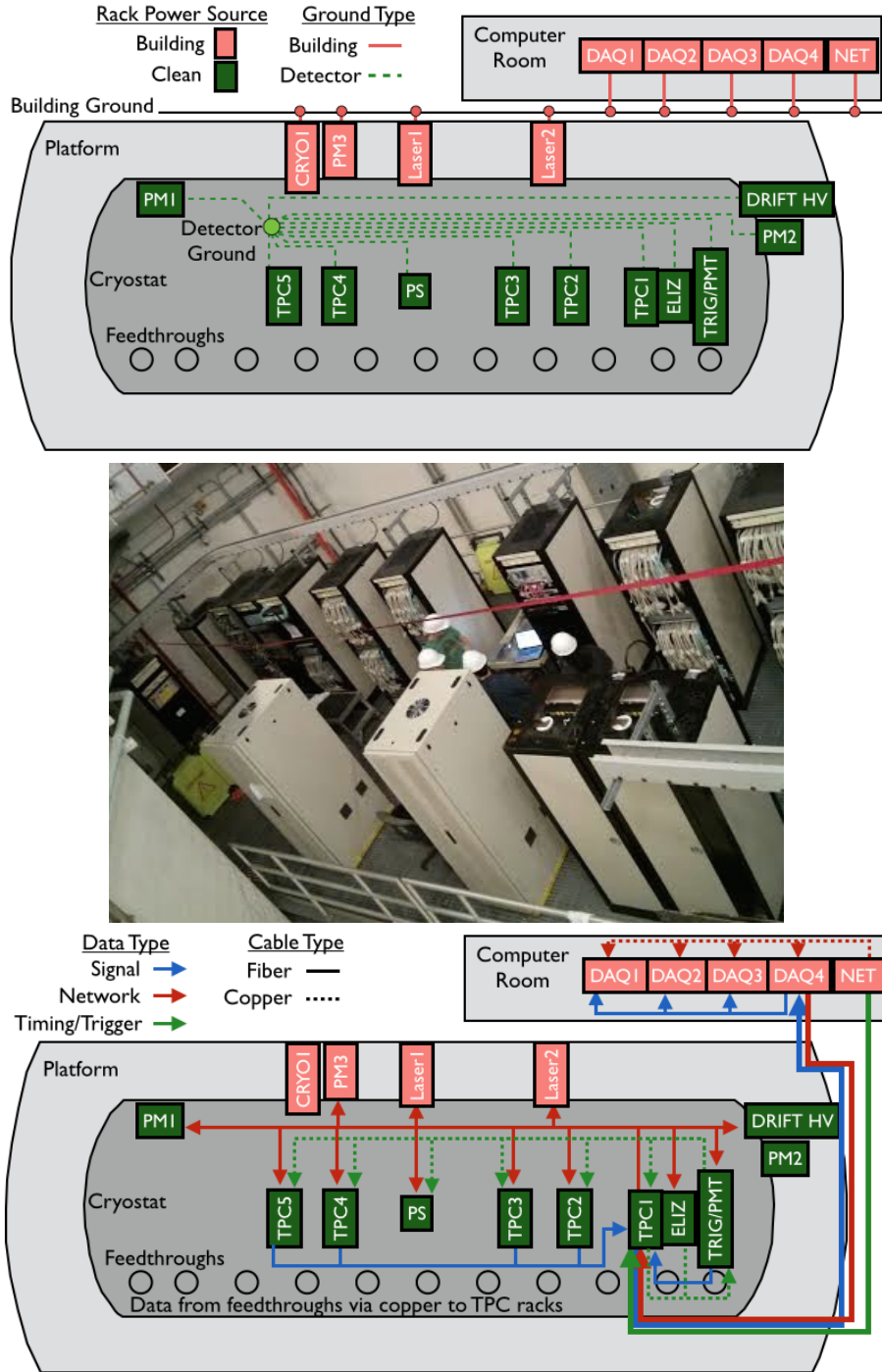


Figure 67: Top: Diagram illustrating location of deployed electronics racks and separation of detector and building grounds and clean and building power for differing racks. Middle: Photograph of installed electronics racks on the LArTF platform. Bottom: A diagram illustrating the general scheme of signal, network, and timing signal cabling in the LArTF computer room and platform.

- 1 purity monitor racks, which either contain noise-producing elements or support building-grounded
 2 components. All racks in the LArTF computer room utilize building power.

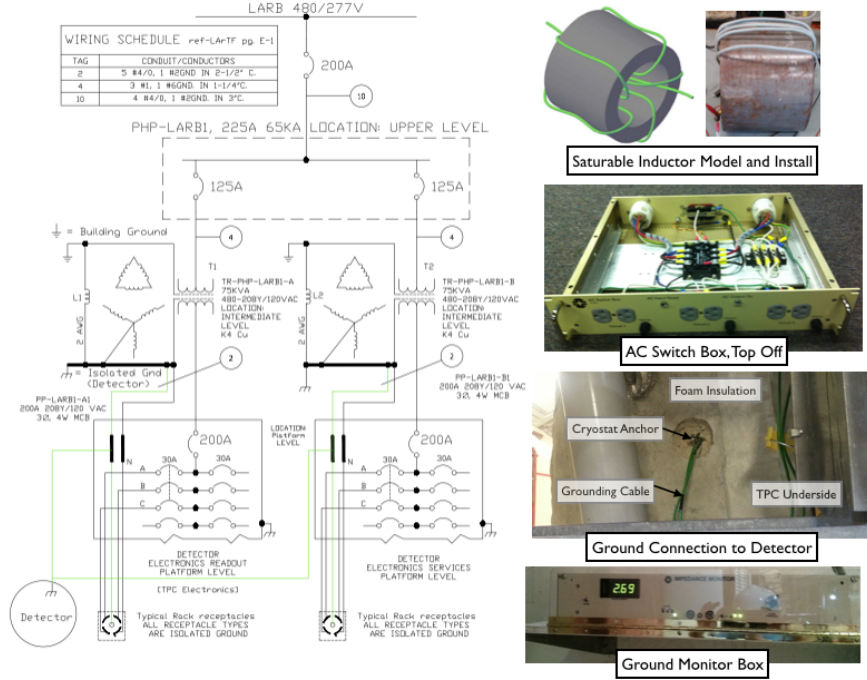


Figure 68: Line drawing of clean power generation and distribution and connections to detector ground, along with pictures of the installed saturable inductor (top), AC switch box (top middle), detector ground strap and connection (bottom middle), and impedance monitor (bottom).

3 208-3phase power is distributed to each individual electronics rack. For racks with signifi-
 4 cant power requirements or a large number of components, this power is delivered to a Fermilab-
 5 designed ‘AC switch box,’ which distributes power to an Eaton Power Distribution Unit (PDU)
 6 only upon receiving an interlock signal from a smoke detection system in each rack, which will be
 7 described in more detail below. Rack components then receive power from one of the three phases
 8 on this PDU. For racks with fewer requirements, power is supplied to components directly from an
 9 interlocked simplified AC switch box or SurgeX SX-1120-RT PDU. Racks with sensitive electron-
 10 ics are grounded to the cryostat via copper sheeting running throughout insulated cable trays above
 11 the cryostat. Sensitive components within each rack are connected to a tin-plated copper grounding
 12 bar electrically connected to the rack bottom and running the height of the rack. Mechanical at-
 13 tachments to the rack provide grounding for less sensitive rack components. As mentioned before,
 14 any unintentional direct connection between building and detector ground can be quickly identified
 15 by the impedance monitor located on the LArTF platform.

16 7.1.2 DC Power Distribution to the MicroBooNE Detector

- 17 DC power is provided to the LArTPC and readout electronics by power supplies in clean-powered,
 18 detector-grounded racks for a variety of purposes:

- Holding the LArTPC cathode plane at voltage to produce the desired ionization electron drift speed
- Holding the two ungrounded anode planes at the proper constant voltage to ensure the planes are transparent to drifting electrons
- Operating the light collection system PMTs
- Powering the cold electronics located inside the LArTPC
- Powering the warm electronics located in the LArTPC readout electronics racks
- Powering auxiliary systems, such as LArTPC temperature sensors and purity monitors

Table 7 summarizes the required voltages or currents for each of these purposes as well as the power supply make and model utilized in each case. Power supplies are located in the relevant subsystem's electronics rack, with power and grounding connections as dictated by that rack.

Table 7: Overview of MicroBooNE DC power distribution. Delivered voltages or currents are listed, along with power supply makes and models and whether each supply utilizes clean or building power.

Sub-System	Supplied Value	Supply Made/Model	Clean Power?
Drift High Voltage	120 kV	Glassman LX150N12	Y
Anode Plane Voltage	1 kV / 8 mA	Wiener MPOD ISEG_EHS 82 10X_805F	Y
PMT High Voltage	2 kV / 3 mA	BIRA T4	Y
Cold Electronics Power	8 V / 10 A	MPOD MPV 800l	Y
Warm LArTPC/PMT Electronics	+/-5V MDH 2-8V/25A +12V MEH 8-15V/92A +3.3V MEH 2-7V/115A	Wiener PL508	Y
Auxiliary Systems Power	Various	Various	Laser: N Inline PM: N Cryostat PM: Y

DC supply power consumption is minimal in most cases, with the exception of the warm LArTPC electronics PL-508 supplies, which can draw in the vicinity of XXX W during normal operation. Care was taken to distribute the AC power load by limiting the number of high-draw PC supplies per electronics rack.

7.1.3 Network, Timing, and Data Distribution for Low-Noise LArTF Data-taking

Network, timing, and data connections must be made between the detector, building-ground, and detector-ground racks to properly read out MicroBooNE data. However, as described above, these connections must be made while maintaining strict detector-building electrical isolation. Deployed interconnections meeting both of these requirements are displayed in figure 67.

1 Timing and LArTF-external network signals are brought into LArTF via electronics in the
2 computer room, where all racks are building grounded and powered. These signals are distributed
3 and processed in the computer room via copper cable, while network and processed timing sig-
4 nals to be sent to the platform are converted onto fiber cables and aggregated into a central fiber
5 termination box. A fiber trunk line then delivers these signals to the platform, where another fiber
6 termination box on a detector-ground rack is used to fan out these signals. Network connections are
7 fanned out via fiber to a network switch in each platform rack, while timing signals are re-converted
8 to copper and further processed for use by the trigger system on a different detector-grounded rack.
9 All rack-to-rack cables are run in insulating cable trays beneath the platform.

10 PMT and LArTPC data are transferred from each detector feedthrough to readout crates in
11 detector-ground racks via insulated copper cable whose shield is tied to detector ground. Digitized
12 crate output is then sent to the aforementioned platform fiber termination box, where these signals
13 are sent via fiber trunk line to the computer room. In the computer room, these fibers are then
14 fanned out to the appropriate DAQ computer. Readout crate and cold electronics control commands
15 are transmitted in the opposite direction utilizing a similar scheme, with crate controls delivered
16 directly via fiber, and cold electronics commands delivered via ranger fiber to a copper fanout in a
17 detector-ground rack.

18 Clock and trigger signals must also be sent from a central trigger rack to all detector-ground
19 LArTPC/PMT readout racks. These signals are transmitted via copper connections, and represent
20 the only source of ground loops on detector ground. To further reduce the possible impact of
21 induced noise in these and all copper cables mentioned above, all insulating cable trays beneath
22 the platform are lined with copper sheeting grounded to the detector. As an additional precaution,
23 all LArTPC signal copper cables are run in separate cable trays from power and auxiliary cabling
24 beneath the platform as well as inside every rack.

25 All cables between all detector components have been uniquely labelled with serial number,
26 source, and destination to allow for ease of replacement and reconnection. Ample fiber and copper
27 spares for every major cable type are also installed along with the production cables to allow for
28 quick replacement of any failed cable.

29 **7.1.4 Interlocks and Safety Systems**

30 All electronics racks contain smoke-sensing and temperature-monitoring systems, which, when
31 interlocked with AC and DC power transmission in each rack, constitute a rack protection system
32 (RPS) designed to meet Fermilab safety requirements and reduce the risk of fire and related damage
33 in LArTF and to individual rack components.

34 The RPS principally consists of a smoke sensor connected to a Fermilab-designed rack pro-
35 tection box. This box produces and outputs a 12 V interlock signal when the rack protection box
36 is on and receiving a ‘no-smoke’ signal from the smoke sensor. This 12 V signal can be sent to the
37 AC distribution box located in each rack, as described above, to allow AC transmission to all rack
38 components only if the RPS is on and not detecting smoke. A similar 12 V ‘RPS Status’ signal
39 is also produced by the RPS box for input into the MicroBooNE slow control box, which will be
40 described in following sections. Alternate contacts are available on the rear of the RPS box for
41 coupling the status of additional subsystems, such as the DAQ and calibration laser uninterruptible
42 power supply (UPS), to smoke sensor or rack power status.

1 Temperature sensors deployed in two or three locations in each electronics rack sample air
2 temperature within each rack. Temperatures at each sensor are read out and recorded in the slow-
3 control database by the slow-control monitoring box. In addition, the box also produces a 5 V
4 interlock signal if all sampled temperatures are within pre-programmed thresholds. In electronics
5 racks distributing PMT- or LArTPC-related DC power these temperature interlock signals are input
6 into each relevant power supply, allowing DC power distribution only when this interlock signal is
7 present, for safety purposes.

8 Additional hardware interlocks ensure the non-simultaneous operation of particular subsys-
9 tems. In particular, the PMT system is disabled when cryogenic system liquid level sensors detect
10 a level below that of the highest PMT bases, or when the UV laser system is active. The former
11 requirement is enforced with a dry-contact hardware interlock, while the latter is enforced with a
12 software interlock in the MicroBooNE online software.

13 **7.1.5 Performance Measurements**

14 The proper operation of each production electronics rack’s AC and DC distribution and RPS sys-
15 tems has been tested prior to installation at LArTF. Furthermore, test stands exercising function-
16 ality of DAQ, PMT and LArTPC electronics, trigger, and drift HV systems have successfully in-
17 corporated and tested various aspects of these same AC and DC distribution and RPS systems.
18 Impedances between detector and building grounds were recorded throughout the installation of
19 the rack infrastructure at LArTF using the impedance monitor located on the LArTF platform.

20 **7.2 Slow monitoring and control system**

21 MicroBooNE uses the Experimental Physics and Industrial Control System (EPICS) [105] for con-
22 trolling and monitoring most devices and conditions important to the experiment. These include
23 power supply controls, temperatures, fan speeds, rack protection interlock status, and various en-
24 vironmental conditions. The DAQ, cryogenics systems, and beam data collection systems operate
25 independently of the EPICS slow monitoring, but export data which are imported into EPICS for
26 archiving and status displays. Applications from the Control System Studio software collection
27 [107] are used for providing displays, alarm notifications, and data archiving.

28 An EPICS system consists of any number of server programs implementing the EPICS Chan-
29 nel Access (CA) protocol [108] to provide client programs access to any number of process vari-
30 ables, where each process variable represents a quantity being controlled (an output) or measured
31 (an input). The EPICS base distribution provides a standard type of channel access server called an
32 Input/Output Controller (IOC), which can be extended to support specific hardware as desired.

33 Most power supplies are controllable over the network through the NetSNMP protocol [109].
34 Several EPICS driver modules are available for SNMP, and MicroBooNE utilizes one written at
35 NSCL [110]. An IOC with this SNMP module runs on a central computer and contacts the power
36 supplies over a private network for monitoring and control. The photomultiplier power supplies
37 are reused from the D0 experiment and have custom IOCs running in their own controllers. The
38 main high voltage power supply has only a simple RS-232 serial interface; control and monitoring
39 for it is provided by a nearby computer running an IOC with the EPICS asynDriver [111] and
40 StreamDevice [112] modules.

1 MicroBooNE has a number of racks in various positions above the detector and in an adjacent
2 server room. Each is equipped with a rack-protection system and multiple digital temperature sen-
3 sors, and most contain one or two fan packs, each containing 6 fans. To monitor and control these
4 devices, each rack has an 1U rack-mount enclosure containing an ARM-based single-board com-
5 puter (SBC) running Linux. An off-the-shelf GESBC-9G20 from Glomation Inc. [113] is utilized
6 for the SBC. A custom interface board [114] connects the SBC to front panel LEDs, temperature
7 probes, fan packs, and rack-protection-status input. The temperature sensors are DS1621 chips,
8 controlled and read out over an I2C bus by the SBC’s I2C controller. The DS1621 also has a ther-
9 mostat output with programmable trip and reset temperatures, which are connected via the interface
10 board to outputs that can be used to interlock devices in the racks, such as power supplies. The fans
11 provide pulse-per-rotation outputs, which are monitored by a 12-channel tachometer implemented
12 via a PIC16F887 microcontroller, and also read out by the I2C bus. An EPICS IOC runs in each
13 SBC, with custom device drivers for reading all status information and controlling the heartbeat
14 LED and temperature sensor trip and reset points.

15 Data are imported into EPICS channels from a number of external sources. The primary rea-
16 son for duplicating these data in EPICS is to integrate displays and warnings into one system for
17 the experiment operators, and to provide integrated archiving for sampled data in the archived
18 database. An IOC running on a central computer provides “soft” process-variables channels for
19 these data. The data acquisition system provides many metrics describing its operation via the
20 Ganglia system[104, 115], which makes the data available in an XML format easily read by a
21 Python script, which in turn writes to EPICS using the PyEPICS module [116]. The hardware and
22 system status of the DAQ computers is monitored through the industry standard Intelligent Plat-
23 form Management Interface (IPMI); rather than writing a script to import data from IPMI directly
24 into EPICS, a IPMI-to-Ganglia interface provided by the FreeIPMI’s “ipmi-sensors” package [117]
25 is used, allowing data to be imported via the same mechanism used for the DAQ metrics. Separate
26 Python scripts periodically retrieve data about outside weather conditions from various sources,
27 cryogenics system data from a file retrieved non-intrusively from the IFIX cryogenics control sys-
28 tem, and beam data from Fermilab’s Intensity Frontier Beam Database (IFDB) [118].

29 **7.3 Beam Monitoring**

30 The primary source of neutrinos for the MicroBooNE experiment is the BNB. The primary beam-
31 line is lined with instrumentation including toroids which indicate beam intensity, “multiwires”
32 showing beam profile in the horizontal and vertical planes, and beam position monitors measuring
33 the mean beam position. Data from these monitors are stored on a spill-by-spill basis in the IFDB.
34 Many of MicroBooNE’s physics analyses require that beam data are recorded for each spill and
35 matched to detector events.

36 Primary beam monitoring in MicroBooNE is done using a “dashboard” interface to IFDB.
37 By using the IFBD instead of the accelerator control system, the experiment can also verify that
38 data are being acquired by the IFBD. The dashboard is accessible over the network using a web
39 browser. The final monitoring step includes a post-data-merge check, ensuring that beam data are
40 successfully matched with detector data for all beam spills. This is done once the detector DAQ
41 binary data file is closed.

1 The dashboard presents a graphic representation of the data, allowing for easy error identification,
 2 as shown in figure 69. The experiment monitors: two toroids which indicate beam intensity;
 3 three multiwires, each of which shows beam profile in each plane; and beam position monitors
 4 along the beamline which show the vertical and the horizontal position. Parameters pertaining to
 5 the target and horn, such as cooling air temperature and horn current, can also be monitored. The
 6 dashboard allows the experiment to easily add additional devices if experience demonstrates the
 7 need for their monitoring.

8 Data are monitored in near real-time. A reasonable history is also kept so that changes are
 9 easily identified. The accelerator control system provides detailed diagnostics tools to experts and
 10 can be used in case of any problems.

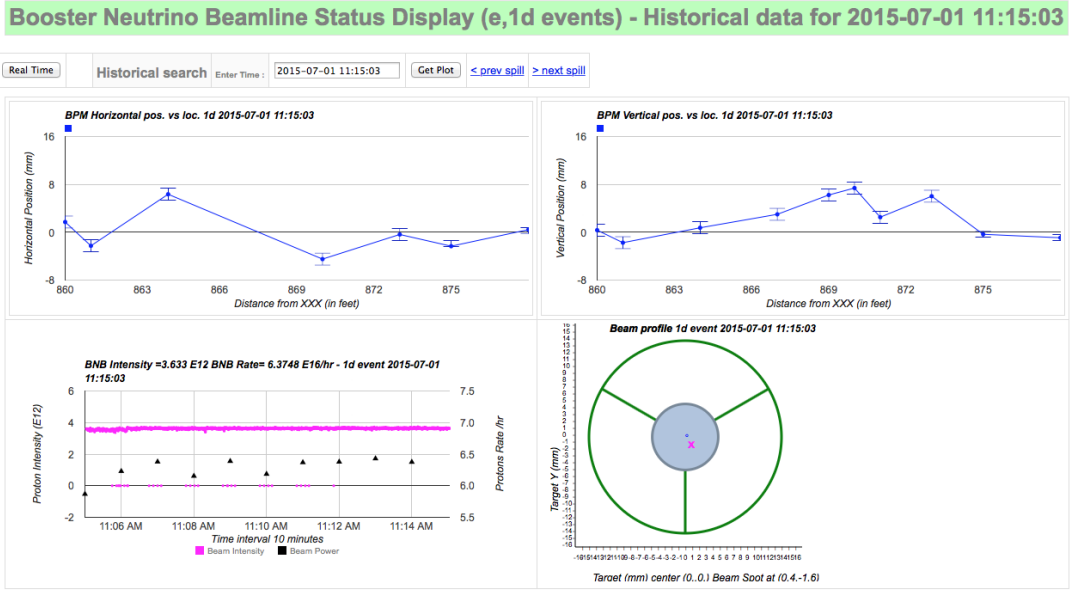


Figure 69: The BNB dashboard, showing graphical representation of beam instrumentation data, is used to monitor the beam. The top box shows the timestamp of the beam spill and indicates if data is stale by changing the color. The two top plots show the primary proton beam position along the BNB. The bottom left plot shows the recent beam spill intensity and rate. The bottom right plot shows the beam as projected onto the Beryllium target (the grey circle in the middle with radius of 0.5cm). The dashboard is accessible via web page providing both real time updates and the review of past data. The page can be easily extended to monitor additional beam devices.

11 8. UV Laser System

12 The knowledge of the electric field inside the drift volume of a LArTPC is a necessary aspect
 13 for performing subsequent event reconstruction. Distortions of particle tracks due to field non-
 14 uniformities affect the accuracy of the particle momentum reconstruction based on multiple scat-
 15 tering. Deviations from a uniform drift field may arise mainly due to accumulation of positive argon
 16 ions in the drift volume. These ions are produced by ionizing particles from neutrino interactions,

1 as well as by cosmic rays. While electrons produced by ionizing particles are quickly (within few
 2 milliseconds) swept towards the readout system, ions have significantly lower mobility. Their drift
 3 velocity in the MicroBooNE detector at nominal drift field is of the order of 0.8 cm/s. The rate of
 4 cosmic muons in the LArTPC volume is estimated to be 11,000 muons/s within the active volume
 5 (assuming a cosmic rate of 200 muons/m²/s through a horizontal plane at the earth's surface and
 6 63 muons/m²/s through a vertical plane), traversing a combined length of 1.9×10^4 m through the
 7 liquid argon. Assuming that cosmic muons are minimum-ionizing (2.1 MeV/cm) and produce 23.6
 8 eV per ion pair, positive ion charge is produced at a rate of 2.8×10^{-8} C/s in the MicroBooNE
 9 TPC. These ions are continuously neutralized at the cathode. The resulting charge distribution in
 10 equilibrium is shown in figure 70. Such accumulated space charge leads to noticeable distortion
 11 of the drift field and, consequently, to deviations of reconstructed track coordinates by up to 10
 12 cm (see figure 71). The ion drift velocity is comparable to local argon flow velocities, produced by
 13 global argon recirculation flow and thermal convection. Therefore the distribution of positive space
 14 charge inside the drift volume may be not only nonuniform (figure 72), but also non-stationary.

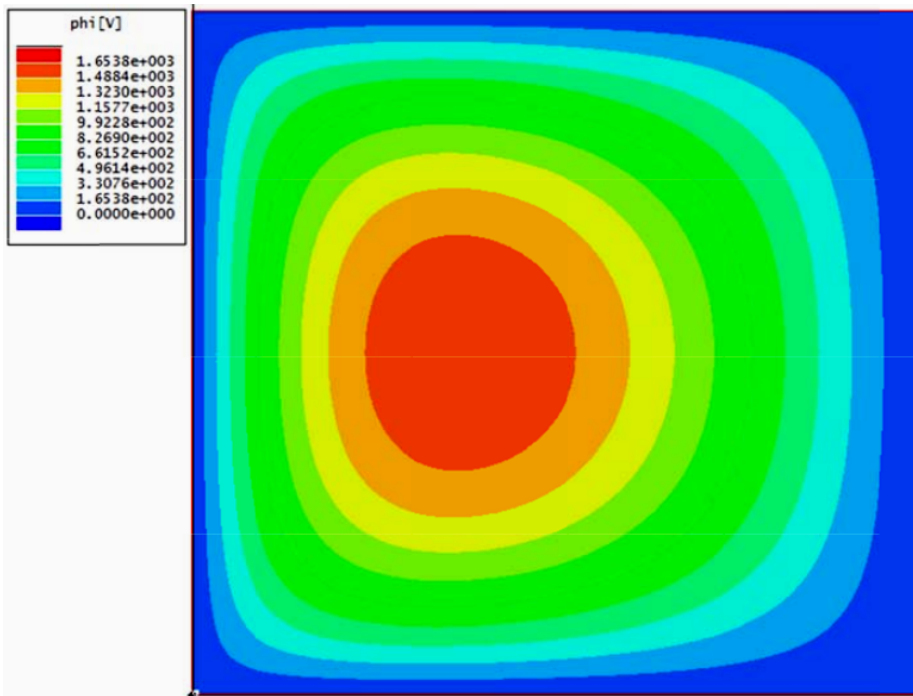


Figure 70: Distorting potential distribution due to positive space charge in equilibrium in the MicroBooNE detector.

15 A nonuniform drift field in the LArTPC leads to the apparent bending of truly straight tracks of
 16 high-momentum ionizing particles. In principle, a set of events from such particles allows for the
 17 reconstruction of the field in any small region of the LArTPC drift volume, using the systematic
 18 apparent curvature of tracks at different angles passing through that region. In practice, the rate
 19 of such events from cosmic muons is too low to acquire sufficient statistics in reasonable time.
 20 A method to generate straight ionization tracks at a defined location in liquid argon is described
 21 in [119]. A collimated photon beam from a pulsed UV laser with $\lambda=266$ nm can ionize liquid

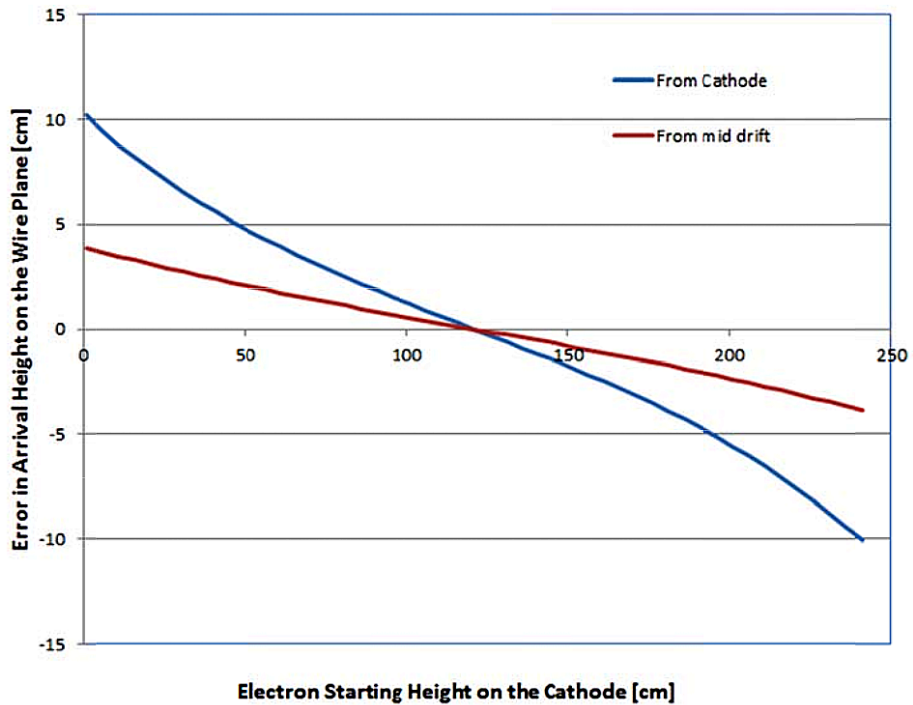


Figure 71: Deviation of a crossing track from its true coordinates due to positive ion space charge.

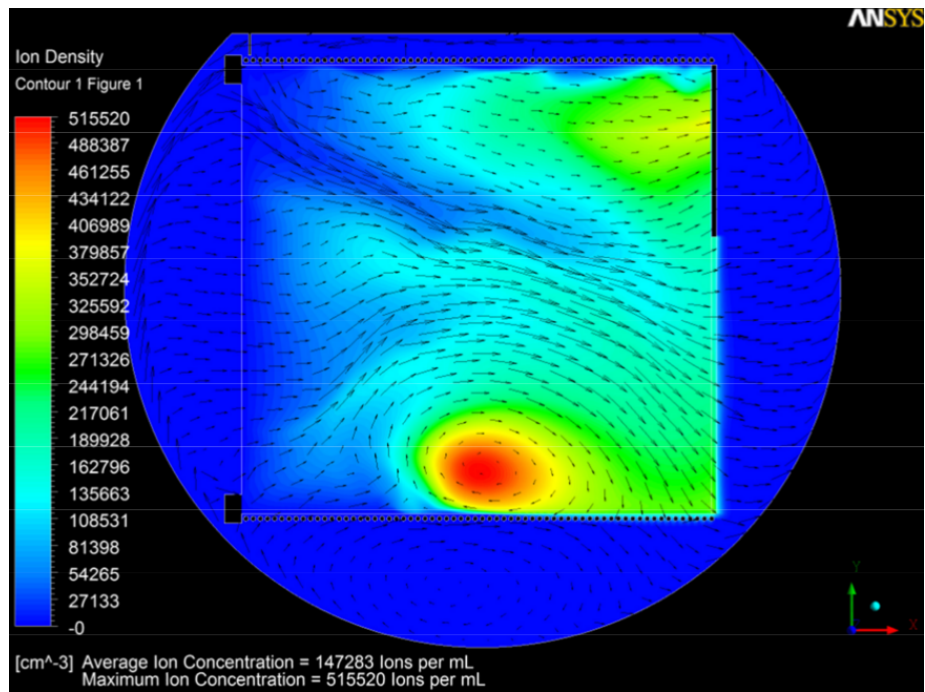


Figure 72: Distribution of the positive space charge in presence of argon circulation.

¹ argon via multi-photon absorption. The resulting ionization track is straight, characterized by low electron density, therefore featuring little charge recombination loss, unlike cosmic muon tracks.

1 Laser tracks are also free from δ -electrons, which complicate track reconstruction in the case of
2 muons. The method was successfully exploited in the Argontube long drift LArTPC [120 – 122]
3 to derive the non-uniformity of the electric field along its 5 m long drift volume (see [123]). The
4 MicroBooNE LArTPC requires a set of such tracks in order to cover the whole sensitive volume to
5 reconstruct field distortions. Tracks are generated one at a time by steering a pulsed laser beam with
6 the use of a custom-designed opto-mechanical feedthrough (see [124]). The pulse rate of the laser
7 generator is 10 Hz. This allows production of a minimum required set of 100 tracks within one
8 minute (taking into account steering time). Details of this solution are described in the following
9 sections.

10 **8.1 UV Laser Calibration**

11 In order to unambiguously reconstruct a drift field vector at any point within the detector fiducial
12 volume, a minimum of two ionization tracks are required to cross in the region of interest. The
13 total number of crossing points is determined by the required reconstruction granularity. In Micro-
14 BooNE the initial scenario is to acquire 100 tracks from each direction, producing a reconstructed
15 3-D map with voxels that are approximately $10 \times 10 \times 50 \text{ cm}^3$ in volume. This map provides a rough
16 picture of the space charge distribution. Depending on the results of this measurement, areas of
17 interest can be studied in more detail. Repetitive study of small volumes may reveal dynamics in
18 the space charge distribution due to turbulent circulation, and should further inform an optimized
19 scenario for a standard UV laser calibration procedure.

20 An algorithm of drift field calibration utilizes an input array of detector events with one straight
21 ionization track in each element of the array. The result of the calibration is a coordinate correction
22 map, to be applied to each track, which converts apparently curved track images back to the true
23 coordinate system where they are straight. The algorithm is iterative with an optimizable iteration
24 step and required accuracy. An example of simulated reconstruction in 2-D space is depicted in
25 figure 73, showing that the magnitude of the field distortions is reduced from 10 cm down to several
26 millimeters in 99% of the detector volume.

27 **8.2 Laser Source and Optics**

28 A Nd:YAG laser emitting light at a wavelength of 1024 nm is used as the primary light source [125].
29 Inside the laser head, nonlinear crystals are installed in the beam line for frequency doubling and
30 summing, resulting in a wavelength of 266 nm needed for ionization of liquid argon. For this
31 wavelength, the Nd:YAG laser is specified to produce an output energy of 60 mJ for each 4 to 6 ns
32 long pulse and a horizontal polarization. The maximal repetition rate is 10 Hz; the beam has a
33 divergence of 0.5 mrad.

34 An optical table, as seen in figure 74, was developed to introduce the necessary parts in a
35 stable and compact environment. With regard to the operation of the optical table on MicroBooNE,
36 the parts were chosen to be accessible remotely where necessary. The emitted laser beam contains
37 not only ultraviolet light but also all other harmonics generated in the crystal and the primary light
38 of 1024 nm. Dichroic Mirrors optimized to reflect only wavelengths in the UV region are used
39 to filter higher wavelengths out. To absorb the transmitted wavelength behind the mirrors, glass-
40 ceramic plates are installed. The beam leaving the laser head is reflected by the first 45° -mirror

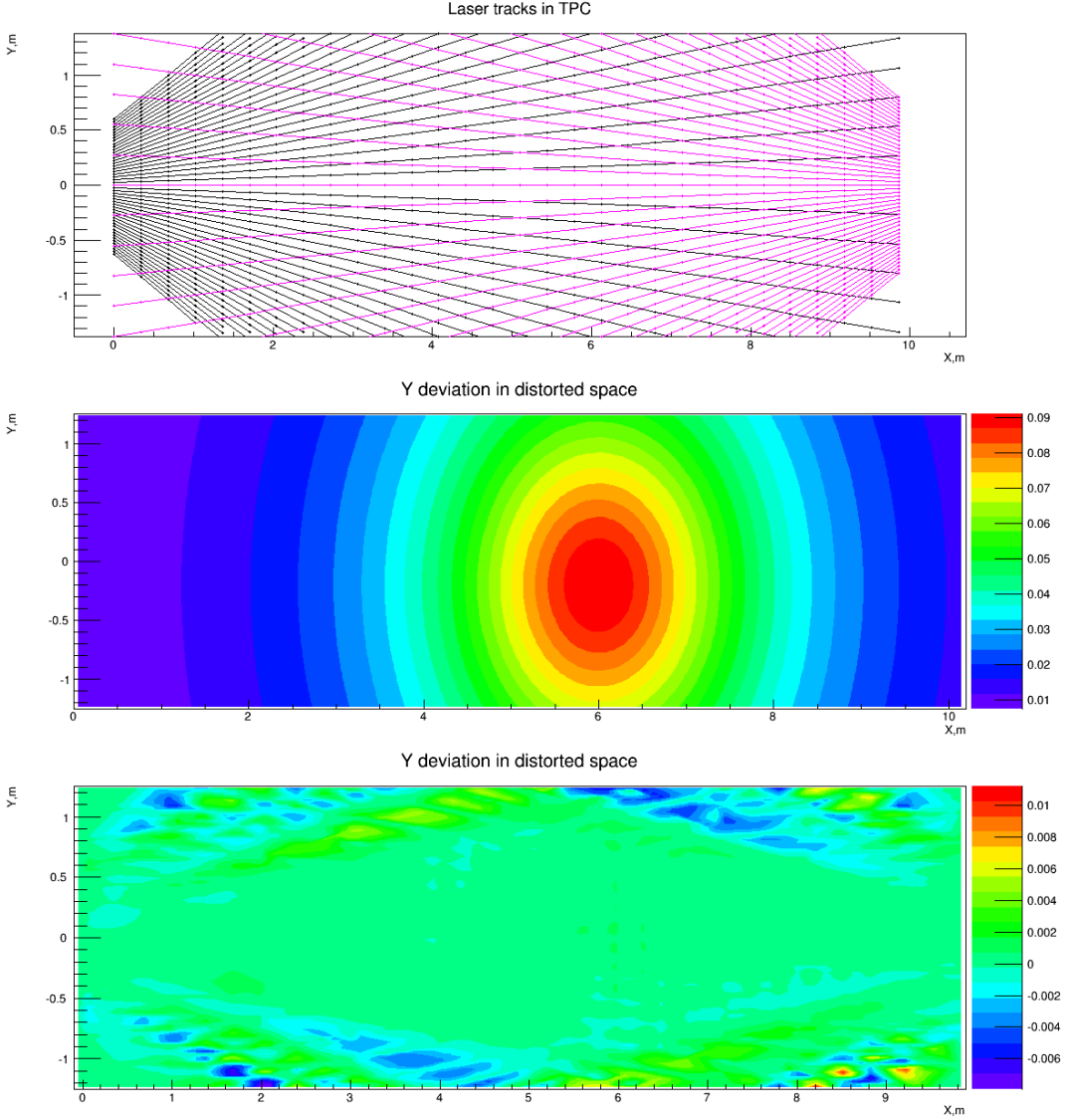


Figure 73: Top: Simulated true laser beam trajectories in the detector; Middle: map of Y coordinate of track deviation under influence of non-uniform electric field; Bottom: residual map of reconstructed track Y-coordinates versus true ones.

1 into an attenuator. For optical adjustment and verification of the non-visible UV-beam, a green
 2 alignment laser is placed behind this mirror and adjusted such that its path is coincident with the
 3 UV-laser beam. In the attenuator (Altechna Wattpilot) a turnable $\lambda/2$ -plate enables rotation of the
 4 orientation of the laser beam polarization. Behind the attenuator two parallel plates are installed
 5 such that the angle of the incident beam matches the Brewster angle of the reflector. Modulating
 6 the polarization of the beam adjusts the intensity of the reflected beam. After the attenuator an
 7 aperture is put in the optical path of the beam to control the beam diameter. The last part in the
 8 beam line is a remotely-controllable mirror mount (Zaber T-OMG), which directs the beam to the
 9 laser feedthrough on the cryostat. A photodiode (Thorlabs DET10A/M), which is sensitive in the

1 ultraviolet region, detects the scattered light when a laser pulse is fired. Its signal is then used as a
 2 trigger for data taking. Both the UV-laser head and the optical table are mounted on a 15 mm thick
 3 aluminum plate.

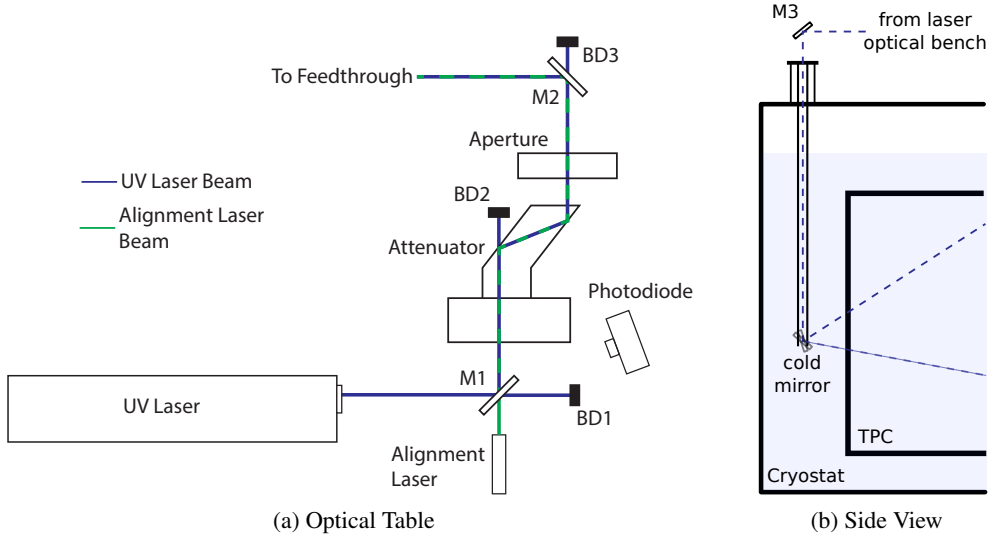


Figure 74: (a) A schematic drawing (not to scale) of the components used for laser beam configuration. An alignment laser (visible light) is introduced along the UV-laser path at the first dichroic mirror (M1), such that the paths overlap. In the attenuator the UV-laser beam intensity can be adjusted to the desired level, and the diameter of the beam is controlled by an aperture. A motorized mirror (M2) deflects the light into the direction of the feedthrough. Beam dumps (BD) are installed behind all mirrors to absorb the non-reflected laser light. (b) Side view of the cryostat indicating the mirror support structure with respect to the LArTPC.

4 8.3 Steering System

5 One of the main challenges of the laser calibration system is the introduction of a steerable laser
 6 beam into the detector. Earlier, an evacuated quartz-glass [126] was utilized to introduce a laser
 7 beam into liquid argon, however this beam had a fixed path through the detector. For the purpose of
 8 scanning the full detector a fully steerable mirror in liquid argon is necessary. In the MicroBooNE
 9 detector, this is achieved by mounting a mirror on a horizontally-rotatable support structure. A
 10 rack and pinion construction, where the mirror is mounted on the frontside of a half gear (pin-
 11 ion), provides the necessary freedom for the vertical movement (see figure 75 right). To steer
 12 the horizontal movement from outside the cryostat, a commercial differentially-pumped rotational
 13 feedthrough is deployed (see figure 75 left). The rack and pinion construction is attached to a linear
 14 feedthrough. Both feedthroughs are motorized to allow for remote control and automation of the
 15 mirror movement. The mirror support structure was fabricated out of polyamide-imide (Duratron
 16 T4301 PAI), which has a very low outgassing rate and low thermal expansion coefficient, and is
 17 certified for operation at 87 K. To minimize the probability of discharges due to the close loca-
 18 tion of the feedthrough to the field cage structure in MicroBooNE, no conductive parts were used
 19 in the support structure. The support structure has a total length of 2.5 m in MicroBooNE. Both

1 feedthroughs are equipped with high precision position encoders from Heidenhain. The accuracy
 2 of the encoders is chosen such that a position accuracy of 2 mm for the laser beam spot over 10 m
 3 distance is achieved. An external interface box controls the encoders and records a position reading
 4 upon receiving a trigger signal from the photodiode. The DAQ computer accesses the position in-
 5 formation over an ethernet connection. The same computer is also used for steering the two motors
 6 via a motor driver system (over a RS232 interface).

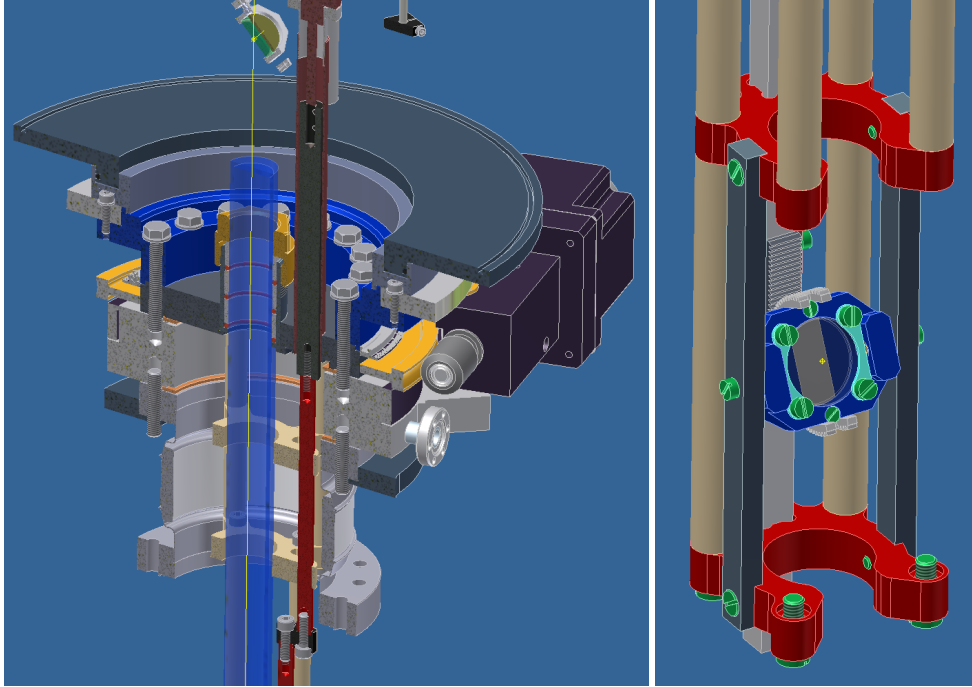


Figure 75: Left: CAD cutaway drawing of the feedthrough construction is shown. The yellow line indicates the laser path. Right, CAD drawing of the cold mirror including the support structure.

7 **8.4 Performance Tests and Initial Operation**

8 A full performance test of the laser calibration system identical to the one installed in the Micro-
 9 BooNE LArTPC was performed prior to the final installation. Apart from the general proof-of-
 10 principle of the laser calibration system, several operationally relevant parameters were identified.
 11 These include scanning speed, positioning accuracy, positioning limits, optimal laser beam inten-
 12 sity, beam diameter, and the minimal achievable field distortion which can be resolved. The test
 13 system consists of a LArTPC equipped with 64 readout channels and an active area of about 400
 14 cm^2 , with a drift distance of 40 cm (see [127] for further details).

15 Several tests of the motorized feedthrough were performed under warm conditions before cold
 16 tests were conducted. One crucial parameter for the quality of the electric field calibration is the
 17 resolution at which laser tracks can be aimed in the detector. For the rotational axis this angle
 18 is directly measured on a circular scale. For the vertical movement the linear displacement of
 19 the bellow is translated into a rotation inside the cryostat, as can be seen in the CAD drawing in
 20 figure 75. This construction introduces uncertainties to the measurement position and backlash.

1 The backlash can be compensated by always approaching positions from the same direction. For
2 the translation of the linear movement ΔL into a rotation $\Delta\phi$ the translation ratio s according to
3 $\Delta L = s \cdot \Delta\phi$ was measured with a laser alignment device³. The obtained ratio is $s = 0.3499 \pm$
4 0.0002 mm/° . The dominant uncertainty in the vertical position measurement is the accuracy
5 of the encoder $\sigma_{\text{linear}} = \pm 1 \mu\text{m}$, which translates into a vertical rotation measurement accuracy
6 $\sigma_{\text{vertical}} = 10.29''$.

7 Horizontal movement limitations arise from the construction of the feedthrough system, namely
8 the warm mirror support structure. This limit has its origins in the way of mounting the laser ta-
9 ble relative to the feedthrough on the MicroBooNE cryostat. Vertically the mirror can be rotated
10 more than 45° relative to the horizon in both directions. In an upward looking configuration, no
11 limitations arise which would affect the coverage of the detector with the beam. A limit arises
12 when the mirror faces the opposite downward direction, when properly aligned onto the centre of
13 the mirror the laser diameter and the size of the mirror limits the achievable coverage. However
14 slight misalignment will affect this limit, since the beam will not be in the optimal spot anymore.
15 In warm tests an maximal downward angle of the beam of 52.5° with respect to the horizon was
16 achieved. During the cold tests the horizontal movement speed was set to $2.6 \text{ }^\circ/\text{s}$ and the vertical
17 speed to $1 \text{ }^\circ/\text{s}$, horizontally an angle of 81° was covered and 22° vertically, respectively. Tests in
18 warm of the fully expanded setup showed vibrations if to high speed was chosen. The vibrations
19 are expected to be damped with a more stable fixation on the detector and the immersion of the
20 setup in liquid argon.

21 Modulation of the beam energy with respect to the vertical alignment of the cold mirror was
22 found to be crucial for obtaining sufficient ionization in the detector. Investigations showed that
23 the reflectivity of the selected dielectric mirrors, which were optimized for 45° in air, are very
24 sensitive to the angle of incidence in liquid argon. Therefore during a calibration run, the beam
25 energy has to be controlled. The emitted UV-laser beam has a diameter of 6 mm and will spatially
26 diverge during propagation. A beam with this diameter will produce an ionization signal larger
27 than the wire spacing, which will limit the capabilities of the full system. With the aperture a small
28 as possible diameter of the laser was selected to enter the detector. Measurements of the diameter
29 were performed with thermal paper (used for thermal printing) on which the selected beam spot
30 burns in. The minimal achieved diameter was 1 mm.

31 **9. Conclusion**

32 The MicroBooNE detector is the culmination of several years of development and construction. It
33 is the largest LArTPC ever constructed in the U.S., and represents a major technological advance
34 that future experiments will build upon.

35 **Acknowledgments**

36 We gratefully acknowledge...

³Bosch GPL3.

1 References

- 2 [1] **MiniBooNE** Collaboration, A. A. Aguilar-Arevalo et al., *Unexplained Excess of Electron-Like*
3 *Events From a 1-GeV Neutrino Beam*, *Phys. Rev. Lett.* **102** (2009) 101802, [[arXiv:0812.2243](#)].
- 4 [2] T. A. Mueller, D. Lhuillier, M. Fallot, A. Letourneau, S. Cormon, M. Fechner, L. Giot, T. Lasserre,
5 J. Martino, G. Mention, A. Porta, and F. Yermia, *Improved predictions of reactor antineutrino*
6 *spectra*, *Phys. Rev. C* **83** (May, 2011) 054615.
- 7 [3] P. Huber, *Determination of antineutrino spectra from nuclear reactors*, *Phys. Rev. C* **84** (Aug, 2011)
8 024617.
- 9 [4] **GALLEX** Collaboration, W. Hampel et al., *Final results of the Cr-51 neutrino source experiments in*
10 *GALLEX*, *Phys. Lett.* **B420** (1998) 114–126.
- 11 [5] **SAGE** Collaboration, J. N. Abdurashitov et al., *Measurement of the response of the*
12 *Russian-American gallium experiment to neutrinos from a Cr-51 source*, *Phys. Rev. C* **59** (1999)
13 2246–2263, [[hep-ph/9803418](#)].
- 14 [6] C. Adams et al., *LAr1-ND: Testing Neutrino Anomalies with Multiple LArTPC Detectors at*
15 *Fermilab*, [arXiv:1309.7987](#).
- 16 [7] T. Doke, *A historical view on the r&d for liquid rare gas detectors*, *Nuclear Instruments and*
17 *Methods in Physics Research Section A* **327** (1993), no. 1 113 – 118.
- 18 [8] W. Willis and V. Radeka, *Liquid-argon ionization chambers as total-absorption detectors*, *Nuclear*
19 *Instruments and Methods* **120** (1974), no. 2 221 – 236.
- 20 [9] C. Rubbia, *The liquid-argon time projection chamber: A new concept for neutrino detectors*, EP
21 Internal Report 77-8, CERN, May, 1977.
- 22 [10] P. Benetti et al., *A three-ton liquid argon time projection chamber*, *Nuclear Instruments and Methods*
23 *in Physics Research Section A: Accelerators, Spectrometers, Detectors and Associated Equipment*
24 **332** (1993), no. 3 395 – 412.
- 25 [11] P. Cennini et al., *Performance of a three-ton liquid argon time projection chamber*, *Nuclear*
26 *Instruments and Methods in Physics Research Section A: Accelerators, Spectrometers, Detectors*
27 *and Associated Equipment* **345** (1994), no. 2 230 – 243.
- 28 [12] F. Arneodo et al., *The ICARUS 50-l LAr TPC in the CERN ν beam*, [hep-ex/9812006](#).
- 29 [13] S. Amerio et al., *Design, construction and tests of the ICARUS T600 detector*, *Nuclear Instruments*
30 *and Methods in Physics Research Section A: Accelerators, Spectrometers, Detectors and Associated*
31 *Equipment* **527** (2004), no. 3 329 – 410.
- 32 [14] S. Amoruso et al., *Measurement of the muon decay spectrum with the icarus liquid argon tpc*, *The*
33 *European Physical Journal C - Particles and Fields* **33** (2004), no. 2 233–241.
- 34 [15] S. Amoruso et al., *Study of electron recombination in liquid argon with the {ICARUS} {TPC}*,
35 *Nuclear Instruments and Methods in Physics Research Section A: Accelerators, Spectrometers,*
36 *Detectors and Associated Equipment* **523** (2004), no. 3 275 – 286.
- 37 [16] M. Antonello et al., *Detection of cherenkov light emission in liquid argon*, *Nuclear Instruments and*
38 *Methods in Physics Research Section A: Accelerators, Spectrometers, Detectors and Associated*
39 *Equipment* **516** (2004), no. 2–3 348 – 363.

- 1 [17] S. Amoruso et al., *Analysis of the liquid argon purity in the ICARUS T600 TPC*, *Nuclear Instruments and Methods in Physics Research Section A: Accelerators, Spectrometers, Detectors and Associated Equipment* **516** (2004), no. 1 68 – 79.
- 2 [18] F. Arneodo et al., *Observation of long ionizing tracks with the ICARUS T600 first half-module*,
Nuclear Instruments and Methods in Physics Research Section A: Accelerators, Spectrometers, Detectors and Associated Equipment **508** (2003), no. 3 287 – 294.
- 3 [19] P. Aprili et al., *The ICARUS experiment: A second-generation proton decay experiment and neutrino observatory at the gran sasso laboratory. cloning of t600 modules to reach the design sensitive mass. (addendum)*, LNGS-EXP 13/89 add.2/01 CERN-SPSC-2002-027, CERN, 2002.
- 4 [20] D. B. Cline, J. G. Learned, K. McDonald, and F. Sergiampietri, *LANNDD—a massive liquid argon detector for proton decay, supernova and solar neutrino studies and a neutrino factory detector*, *Nuclear Instruments and Methods in Physics Research Section A: Accelerators, Spectrometers, Detectors and Associated Equipment* **503** (2003), no. 1–2 136 – 140. Proceedings of the 3rd International Workshop on Neutrino Factories based on Muon Storage Rings.
- 5 [21] A. Rubbia, *Experiments for CP violation: A Giant liquid argon scintillation, Cerenkov and charge imaging experiment?*, hep-ph/0402110.
- 6 [22] A. Rubbia, *Underground Neutrino Detectors for Particle and Astroparticle Science: The Giant Liquid Argon Charge Imaging ExpeRiment (GLACIER)*, *J.Phys.Conf.Ser.* **171** (2009) 012020, [arXiv:0908.1286].
- 7 [23] LAGUNA Collaboration. <http://laguna.ethz.ch/LAGUNA/Welcome.html>.
- 8 [24] A. Stahl et al., *Expression of Interest for a very long baseline neutrino oscillation experiment (LBNO)*, Tech. Rep. CERN-SPSC-2012-021. SPSC-EOI-007, CERN, Geneva, Jun, 2012.
- 9 [25] S. Agarwalla et al., *The mass-hierarchy and CP-violation discovery reach of the LBNO long-baseline neutrino experiment*, *JHEP* **1405** (2014) 094, [arXiv:1312.6520].
- 10 [26] C. Adams et al., *The Long-Baseline Neutrino Experiment: Exploring Fundamental Symmetries of the Universe*, arXiv:1307.7335.
- 11 [27] DUNE Collaboration, R. Acciarri et al., *Long-Baseline Neutrino Facility (LBNF) and Deep Underground Neutrino Experiment (DUNE)*, arXiv:1512.0614.
- 12 [28] C. Anderson et al., *The ArgoNeuT Detector in the NuMI Low-Energy beam line at Fermilab*, *JINST* **7** (2012) P10019, [arXiv:1205.6747].
- 13 [29] R. Acciarri et al., *A study of electron recombination using highly ionizing particles in the ArgoNeuT Liquid Argon TPC*, *JINST* **8** (2013) P08005, [arXiv:1306.1712].
- 14 [30] C. Anderson et al., *First Measurements of Inclusive Muon Neutrino Charged Current Differential Cross Sections on Argon*, *Phys.Rev.Lett.* **108** (2012) 161802, [arXiv:1111.0103].
- 15 [31] R. Acciarri et al., *Measurements of Inclusive Muon Neutrino and Antineutrino Charged Current Differential Cross Sections on Argon in the NuMI Antineutrino Beam*, *Phys.Rev.* **D89** (2014) 112003, [arXiv:1404.4809].
- 16 [32] R. Acciarri et al., *First Measurement of Neutrino and Antineutrino Coherent Charged Pion Production on Argon*, arXiv:1408.0598.
- 17 [33] R. Acciarri et al., *LArIAT: Liquid Argon In A Testbeam*, arXiv:1406.5560.
- 18 [34] A. Szeli, *The LArIAT light readout system*, *JINST* **8** (2013) C09011.

- 1 [35] M. Adamowski et al., *The Liquid Argon Purity Demonstrator*, *JINST* **9** (2014) P07005,
2 [[arXiv:1403.7236](#)].
- 3 [36] B. Rebel et al., *Results from the Fermilab materials test stand and status of the liquid argon purity*
4 *demonstrator*, *J.Phys.Conf.Ser.* **308** (2011) 012023.
- 5 [37] D. Montanari et al., *First scientific application of the membrane cryostat technology.*, .
- 6 [38] **HEPAP Subcommittee** Collaboration, S. Ritz et al., *Building for Discovery: Strategic Plan for U.S.*
7 *Particle Physics in the Global Context*, .
- 8 [39] A. Marchionni, *Status and New Ideas Regarding Liquid Argon Detectors*, *Ann.Rev.Nucl.Part.Sci.* **63**
9 (2013) 269–290, [[arXiv:1307.6918](#)].
- 10 [40] P. Adamson et al., *The NuMI Neutrino Beam*, *Nucl. Instrum. Meth.* **A806** (2016) 279–306,
11 [[arXiv:1507.0669](#)].
- 12 [41] **MiniBooNE** Collaboration, A. Aguilar-Arevalo et al., *The Neutrino Flux prediction at MiniBooNE*,
13 *Phys.Rev.* **D79** (2009) 072002, [[arXiv:0806.1449](#)].
- 14 [42] E. Aprile, K. Giboni, and C. Rubbia, *A study of ionization electrons drifting large distances in liquid*
15 *and solid argon*, *Nuclear Instruments and Methods in Physics Research Section A: Accelerators,*
16 *Spectrometers, Detectors and Associated Equipment* **241** (1985), no. 1 62 – 71.
- 17 [43] C. Tegeler, R. Span, and W. Wagner, *A new equation of state for argon covering the fluid region for*
18 *temperatures from the melting line to 700 k at pressures up to 1000 mpa*, *Journal of Physical and*
19 *Chemical Reference Data* **28** (1999), no. 3 779–850.
- 20 [44] R. L. Amey and R. H. Cole, *Dielectric constants of liquefied noble gases and methane*, *The Journal*
21 *of Chemical Physics* **40** (1964), no. 1 146–148.
- 22 [45] C. Amsler et al., *Review of particle physics*, *Physics Letters B* **667** (2008), no. 1–5 1 – 6.
23 <http://pdg.lbl.gov/2008/reviews/rpp2008-rev-passage-particles-matter.pdf>.
- 24 [46] E. Shibamura, A. Hitachi, T. Doke, T. Takahashi, S. Kubota, and M. Miyajima, *Drift velocities of*
25 *electrons, saturation characteristics of ionization and W-values for conversion electrons in liquid*
26 *argon, liquid argon-gas mixtures and liquid xenon*, *Nuclear Instruments and Methods* **131** (Dec.,
27 1975) 249–258.
- 28 [47] M. Miyajima, T. Takahashi, S. Konno, T. Hamada, S. Kubota, H. Shibamura, and T. Doke, *Average*
29 *energy expended per ion pair in liquid argon*, *Phys. Rev. A* **9** (Mar, 1974) 1438–1443.
- 30 [48] E. Shibamura, T. Takahashi, S. Kubota, and T. Doke, *Ratio of diffusion coefficient to mobility for*
31 *electrons in liquid argon*, *Phys. Rev. A* **20** (Dec, 1979) 2547–2554.
- 32 [49] S. Derenzo, *Electron diffusion and positive ion charge retention in liquid-filled high-resolution*
33 *multistrip ionization-mode chambers*, *Lawrence Berkeley Laboratory, Group A Physics Note No.* 786
34 (1974).
- 35 [50] V. Atrazhev and I. Timoshkin, *Transport of electrons in atomic liquids in high electric fields*, *IEEE*
36 *Transactions on Dielectrics and Electrical Insulation* **5** (June, 1998) 450 –457.
- 37 [51] *ASME boiler and pressure vessel code: an international code. I - Rules for construction of power*
38 *boiler*. American Society of Mechanical Engineers, New York, NY, 2010.
- 39 [52] B. Jones, C. Chiu, J. Conrad, C. Ignarra, T. Katori, et al., *A Measurement of the Absorption of Liquid*
40 *Argon Scintillation Light by Dissolved Nitrogen at the Part-Per-Million Level*, *JINST* **8** (2013)
41 P07011, [[arXiv:1306.4605](#)].

- 1 [53] Barber-Nichols Inc., 6325 West 55th Avenue, Arvada, CO 80002 USA.
- 2 [54] Sigma-Aldrich, P.O. Box 14508, St. Louis, MO 63178 USA.
- 3 [55] BASF Corp., 100 Park Avenue, Florham Park, NJ 07932 USA.
- 4 [56] Aspen Aerogels, Inc., 30 Forbes Road, Building B, Northborough, MA 01532 USA.
- 5 [57] G. Carugno et al., *Electron lifetime detector for liquid argon*, *Nuclear Instruments and Methods in*
6 *Physics Research Section A: Accelerators, Spectrometers, Detectors and Associated Equipment* **292**
7 (1990) 580.
- 8 [58] L. F. Bagby et al., *Breakdown voltage of metal-oxide resistors in liquid argon*, *JINST* **9** (2014),
9 no. 11 T11004, [[arXiv:1408.4013](#)].
- 10 [59] **MicroBooNE** Collaboration, R. Acciarri et al., *Liquid Argon Dielectric Breakdown Studies with the*
11 *MicroBooNE Purification System*, *JINST* **9** (2014), no. 11 P11001, [[arXiv:1408.0264](#)].
- 12 [60] J. Asaadi, J. M. Conrad, S. Gollapinni, B. J. P. Jones, H. Jostlein, J. M. St. John, T. Strauss,
13 S. Wolbers, and J. Zennamo, *Testing of High Voltage Surge Protection Devices for Use in Liquid*
14 *Argon TPC Detectors*, *JINST* **9** (2014) P09002, [[arXiv:1406.5216](#)].
- 15 [61] R. Acciarri et al., *Construction and Assembly of the Wire Planes for the MicroBooNE Time*
16 *Projection Chamber*, [arXiv:1609.0616](#).
- 17 [62] W. Buescher, *Spectrum Laboratory*, . <http://www.qsl.net/dl4yhf/spectra1.html>.
- 18 [63] “Citanox acid detergent.”
19 http://www.alconox.com/resources/StandardDocuments/MSDS/msds_citanox_english_ghs.pdf.
- 20 [64] “Simple Green detergent.” http://simplegreen.com/pdfs/MSDS_EN-US_AllPurposeCleaner.pdf.
- 21 [65] “Elma Clean 65.” [http://www.elma-](http://www.elma-ultrasonic.com/fileadmin/downloads/CleaningAgents/SafetyDataSheets/GB/S_EC%2065_GB.pdf)
22 [ultrasonic.com/fileadmin/downloads/CleaningAgents/SafetyDataSheets/GB/S_EC%2065_GB.pdf](http://www.elma-ultrasonic.com/fileadmin/downloads/CleaningAgents/SafetyDataSheets/GB/S_EC%2065_GB.pdf).
- 23 [66] L. Bugel, J. M. Conrad, C. Ignarra, B. J. P. Jones, T. Katori, T. Smidt, and H. K. Tanaka,
24 *Demonstration of a Lightguide Detector for Liquid Argon TPCs*, *Nucl. Instrum. Meth. A* **640** (2011)
25 69–75, [[arXiv:1101.3013](#)].
- 26 [67] **MicroBooNE** Collaboration, T. Katori, *MicroBooNE, A Liquid Argon Time Projection Chamber*
27 (*LArTPC*) *Neutrino Experiment*, *AIP Conf. Proc.* **1405** (2011) 250–255, [[arXiv:1107.5112](#)].
- 28 [68] C. Chiu, C. Ignarra, L. Bugel, H. Chen, J. Conrad, et al., *Environmental Effects on TPB*
29 *Wavelength-Shifting Coatings*, *JINST* **7** (2012) P07007, [[arXiv:1204.5762](#)].
- 30 [69] B. Baptista, L. Bugel, C. Chiu, J. Conrad, C. Ignarra, et al., *Benchmarking TPB-coated Light Guides*
31 *for Liquid Argon TPC Light Detection Systems*, [arXiv:1210.3793](#).
- 32 [70] T. Briese, L. Bugel, J. Conrad, M. Fournier, C. Ignarra, et al., *Testing of Cryogenic Photomultiplier*
33 *Tubes for the MicroBooNE Experiment*, *JINST* **8** (2013) T07005, [[arXiv:1304.0821](#)].
- 34 [71] B. Jones, T. Alexander, H. Back, G. Collin, J. Conrad, et al., *The Effects of Dissolved Methane upon*
35 *Liquid Argon Scintillation Light*, *JINST* **8** (2013) P12015, [[arXiv:1308.3658](#)].
- 36 [72] **MicroBooNE** Collaboration, T. Katori, *The MicroBooNE light collection system*, *JINST* **8** (2013)
37 C10011, [[arXiv:1307.5256](#)].
- 38 [73] B. Baller, N. Buchanan, F. Cavanna, H. Chen, E. Church, et al., *Liquid Argon Time Projection*
39 *Chamber Research and Development in the United States*, *JINST* **9** (2014) T05005,
40 [[arXiv:1307.8166](#)].

- 1 [74] Z. Moss, L. Bugel, G. Collin, J. Conrad, B. Jones, et al., *Improved TPB-coated Light Guides for*
2 *Liquid Argon TPC Light Detection Systems*, arXiv:1410.6256.
- 3 [75] MicroBooNE Collaboration, J. Conrad, B. Jones, Z. Moss, T. Strauss, and M. Toups, *The*
4 *Photomultiplier Tube Calibration System of the MicroBooNE Experiment*, *JINST* **10** (2015), no. 06
5 T06001, [arXiv:1502.0415].
- 6 [76] R. Acciarri, M. Adamowski, D. Artrip, B. Baller, C. Bromberg, et al., *Summary of the Second*
7 *Workshop on Liquid Argon Time Projection Chamber Research and Development in the United*
8 *States*, arXiv:1504.0560.
- 9 [77] Z. Moss, M. Toups, L. Bugel, G. Collin, and J. Conrad, *Anode-Coupled Readout for Light Collection*
10 *in Liquid Argon TPCs*, arXiv:1507.0199.
- 11 [78] B. J. P. Jones, *Sterile Neutrinos in Cold Climates*. PhD thesis, MIT, 2015.
- 12 [79] M. Suzuki and S. Kubota, *Mechanism of proportional scintillation in argon, krypton and xenon*,
13 *Nuclear Instruments and Methods* **164** (1979), no. 1 197 – 199.
- 14 [80] A. Hitachi, T. Takahashi, N. Funayama, K. Masuda, J. Kikuchi, and T. Doke, *Effect of ionization*
15 *density on the time dependence of luminescence from liquid argon and xenon*, *Phys. Rev. B* **27** (May,
16 1983) 5279–5285.
- 17 [81] WArP Collaboration, R. Acciarri et al., *Effects of Nitrogen contamination in liquid Argon*, *JINST* **5**
18 (2010) P06003, [arXiv:0804.1217].
- 19 [82] N. Ishida, M. Chen, T. Doke, K. Hasuike, A. Hitachi, M. Gaudreau, M. Kase, Y. Kawada, J. Kikuchi,
20 T. Komiyama, K. Kuwahara, K. Masuda, H. Okada, Y. H. Qu, M. Suzuki, and T. Takahashi,
21 *Attenuation length measurements of scintillation light in liquid rare gases and their mixtures using*
22 *an improved reflection suppresser*, *Nuclear Instruments and Methods in Physics Research A* **384**
23 (Feb., 1997) 380–386.
- 24 [83] Hamamatsu, “Large area photomultipier tubes.” Specification for R5912 and R5912-02
25 photomultiplier tubes:
26 http://www.hamamatsu.com/resources/pdf/etd/LARGE_AREA_PMT TPMH1286E05.pdf.
- 27 [84] E. H. Bellamy, G. Bellettini, F. Gervelli, M. Incagli, D. Lucchesi, C. Pagliarone, F. Zetti,
28 Yu. Budagov, I. Chirikov-Zorin, and S. Tokar, *Absolute calibration and monitoring of a*
29 *spectrometric channel using a photomultiplier*, *Nucl. Instrum. Meth. A* **339** (1994) 468–476.
- 30 [85] H. O. Meyer, *Dark Rate of a Photomultiplier at Cryogenic Temperatures*, arXiv:0805.0771.
- 31 [86] H. Meyer, *Spontaneous electron emission from a cold surface*, *EPL* (2010), no. 89 58001.
- 32 [87] Hamamatsu Photonics, *Photomultiplier Tubes, Basics and Applications, Third Edition, Chapter*
33 *13.9*, . https://www.hamamatsu.com/resources/pdf/etd/PMT_handbook_v3aE.pdf.
- 34 [88] W. Burton and B. Powell, *Fluorescence of tetraphenyl-butadiene in the vacuum ultraviolet.*, *Appl*
35 *Opt.* **12** (1973), no. 1 87–9.
- 36 [89] C. M. Ignarra, *Sterile Neutrino Searches in MiniBooNE and MicroBooNE*. PhD thesis, MIT,
37 Cambridge, 2014.
- 38 [90] V. Gehman, S. Seibert, K. Rielage, A. Hime, Y. Sun, et al., *Fluorescence Efficiency and Visible*
39 *Re-emission Spectrum of Tetraphenyl Butadiene Films at Extreme Ultraviolet Wavelengths*,
40 *Nucl.Instrum.Meth. A* **654** (2011) 116–121, [arXiv:1104.3259].

- 1 [91] R. Francini, R. Montereali, E. Nichelatti, M. Vincenti, N. Canci, et al., *VUV-Vis optical*
 2 *characterization of Tetraphenyl-butadiene films on glass and specular reflector substrates from room*
 3 *to liquid Argon temperature*, *JINST* **8** (2013) P09006.
- 4 [92] B. J. P. Jones, *A simulation of the optical attenuation of TPB coated light-guide detectors*, *JINST* **8**
 5 (2013) C10015, [[arXiv:1307.6906](#)].
- 6 [93] Sundance Supply, “Lexan Thermoclear Multiwall Polycarbonate Sheet.”
 7 <https://www.sundancesupply.com/Lexan.pdf>.
- 8 [94] “Stycast 2850.” <http://www.ellsworth.com/manufacturers/emerson-cuming>.
- 9 [95] J. B. Birks and K. N. Kuchela, *Energy transfer in fluorescent plastic solutions*, *Disc. Faraday. Soc* **27**
 10 (1959) 57–63.
- 11 [96] J. B. Birks and K. N. Kuchela, *Energy transfer in organic systems ii: Solute-solute transfer in liquid*
 12 *solutions*, *Proc. Phys. Soc* **77** (1961) 1083.
- 13 [97] S. Hanagodimath, B. Siddlingeshwar, J. Thipperudrappa, S. Kumar, and B. Hadimani,
 14 *Fluorescence-quenching studies and temperature dependence of fluorescence quantum yield, decay*
 15 *time and intersystem crossing activation energy of tpb*, *J. Lumin* **129** (2008), no. 4 335–339.
- 16 [98] L. Liu, “Time resolved fluorescence studies of dye-polymers as excited by laser and beta radiation.”
 17 PhD Thesis at Texas Tech University -
 18 <http://repositories.tdl.org/ttu-ir/bitstream/handle/2346/13744/31295012500558.pdf?sequence=1>.
- 19 [99] Hamamatsu, “Photomultipler tube r7723, r7724, r7725.”
 20 <http://www.hamamatsu.com/resources/pdf/etd/R7723 TPMH1315E01.pdf>.
- 21 [100] **ICARUS** Collaboration, A. Ankowski et al., *Energy reconstruction of electromagnetic showers from*
 22 *pi0 decays with the ICARUS T600 Liquid Argon TPC*, *Acta Phys. Polon.* **B41** (2010) 103–125,
 23 [[arXiv:0812.2373](#)].
- 24 [101] A. Ereditato Private Communication.
- 25 [102] K. Scholberg, *The SuperNova Early Warning System*, *Astron. Nachr.* **329** (2008) 337–339,
 26 [[arXiv:0803.0531](#)].
- 27 [103] “LArSoft.” <http://larsoft.org>.
- 28 [104] M. Massie et al., *Monitoring with Ganglia: Tracking Dynamic Host and Application Metrics at*
 29 *Scale*. O'Reilly Media, 2012.
- 30 [105] “Experimental physics and industrial control system.” <http://www.aps.anl.gov/epics/>.
- 31 [106] R. Brun and F. Rademakers, *Root — an object oriented data analysis framework*, *Nuclear*
 32 *Instruments and Methods in Physics Research Section A: Accelerators, Spectrometers, Detectors*
 33 *and Associated Equipment* **389** (1997), no. 1 81 – 86.
- 34 [107] “Control system studio.” <http://controlsystemstudio.org/>; developer's manual:
 35 <http://cs-studio.sourceforge.net/docbook/>.
- 36 [108] *Channel access protocol specification*, September, 2014. <http://www.aps.anl.gov/epics/docs/ca.php>.
- 37 [109] “Net-snmp.” <http://www.net-snmp.org>.
- 38 [110] J. Priller, *Epics snmp device support module: Release 1.0.0*, April, 2014.
 39 <https://groups.nscl.msu.edu/controls/>.

- 1 [111] M. Rivers, *asyndriver: Asynchronous driver support*, September, 2014.
 2 http://www.aps.anl.gov/epics/modules/soft/asyndriver/.
- 3 [112] D. Zimoch, *Epics streamdevice*, September, 2014.
 4 http://epics.web.psi.ch/software/streamdevice/doc/.
- 5 [113] Glomation, inc., *gesbc-9g20 user's manual, version 0.2*, June, 2009.
 6 http://www.gломатионинк.com/GESBC-9G20-user-manual.pdf.
- 7 [114] D. Huffman, *Peripheral interface: Fan and temperature probe*, September, 2014.
 8 http://www-ppd.fnal.gov/EEDOffice-W/Infrastructure_group/Huffman/WEB/uboone/pia.html.
- 9 [115] *Ganglia*, September, 2014. http://ganglia.info/.
- 10 [116] M. Newville, *Pyepics: Epics channel access for python*, September, 2014.
 11 http://cars9.uchicago.edu/software/python/pyepics3/.
- 12 [117] *Gnu freeipmi*, September, 2014. http://www.gnu.org/software/freeipmi/.
- 13 [118] I. Mandrichenko, A. Norman, A. Petrov, and V. Podstavkov, *Implementation of beam conditions database for intensity frontier experiments*, June, 2012.
 14 http://cd-docdb.fnal.gov/cgi-bin>ShowDocument?docid=4781.
- 15 [119] I. Badhrees et al., *Measurement of the two-photon absorption cross-section of liquid argon with a time projection chamber*, *New J.Phys.* **12** (2010) 113024, [[arXiv:1011.6001](#)].
- 16 [120] I. Badhrees et al., *Argontube: An R&D Liquid Argon Time Projection Chamber*, *JINST* **7** (2012) C02011.
- 17 [121] A. Ereditato et al., *Design and operation of ARGONTUBE: a 5 m long drift liquid argon TPC*, *JINST* **8** (2013) P07002, [[arXiv:1304.6961](#)].
- 18 [122] M. Zeller et al., *First measurements with ARGONTUBE, a 5m long drift Liquid Argon TPC*, *Nucl.Instrum.Meth.* **A718** (2013) 454–458.
- 19 [123] A. Ereditato et al., *Measurement of the drift field in the ARGONTUBE LAr TPC with 266 nm pulsed laser beams*, [arXiv:1408.6635](#).
- 20 [124] A. Ereditato et al., *A steerable UV laser system for the calibration of liquid argon time projection chambers*, [arXiv:1406.6400](#).
- 21 [125] “Continuum Lasers.” [http://www.continuumlasers.com](#).
- 22 [126] I. Badhrees, A. Ereditato, I. Kreslo, M. Messina, U. Moser, B. Rossi, M. S. Weber, M. Zeller, C. Altucci, S. Amoruso, R. Buzzese, and R. Velotta, *Measurement of the two-photon absorption cross-section of liquid argon with a time projection chamber*, *New Journal of Physics* **12** (2010), no. 11 113024.
- 23 [127] A. Ereditato, I. Kreslo, M. Lüthi, C. R. von Rohr, M. Schenk, T. Strauss, M. Weber, and M. Zeller, *A steerable uv laser system for the calibration of liquid argon time projection chambers*, *Journal of Instrumentation* **9** (2014), no. 11 T11007.